Master Thesis

Post-Liquefaction Soil-Structure Interaction of Pipelines Buried in Sand

Using Modern Simulation Techniques

TU Delft

Author: Lysimachos Tigkas

Student Number: 4521730

Date: 21 January 2019

DELFT UNIVERSITY OF TECHNOLOGY

FACULTY OF CIVIL ENGINEERING

SECTION OF GEO-ENGINEERING

Post Liquefaction Soil-Structure Interaction of Pipelines Buried in Sand

Using Modern Simulation Techniques

Master Thesis

Graduation Committee:

Dr. Ir. W. BROERE (TU Delft)

Prof. Dr. M. HICKS (TU Delft)

Dr. Ir. F. PISANO (TU Delft)

PREFACE

Before you lies the thesis “Post liquefaction soil-structure interaction of pipelines buried in sand: using modern simulation techniques”. The basis of this is the modelling of pipelines buried in sand during post-liquefaction, which has originally been triggered by earthquake excitations. This work has been written for the graduation requirements fulfilment of the Geo-Engineering track of the Civil engineering and Geosciences at Delft University of Technology. I was engaged in writing and researching this thesis from February 2017 till November 2018.

In this section, I would like to thank all members of my committee for their guidance and support. I would also like to express my thanks and appreciation to my supervisor, Dr. W. Broere, for his excellent guidance and cooperation during this project. Lastly, I feel that I owe thanks to the spectacular academic community of the University, which provided me with the knowledge required for undertaking this project.

At this point, I would like to thank my family. More specifically, I would like to thank my aunt, without whose endless support the completion of this project would not have been possible. My brothers and sister, who have always stood by my side every time I lost my faith. Last, but certainly not least, I would like to express my deepest and most sincere thanks to my mother, the memory of which has kept me trying.

This is for mum.

Lysmachos Tigkas,

Delft, January 2019

ABSTRACT

The starting point of this thesis lies in the area on Groningen, Netherlands. More specifically, induced earthquake activity is observed in this area due to gas extraction activities, which reduce underground gas pressure. In combination with the location's geomorphology, liquefaction can occur due to earthquake excitations. Furthermore, the area of Groningen is a location with urban activity and infrastructure, such as pipelines, present. The post-liquefaction effect of these pipelines is their uplift, which can lead to failure, along with all its negative consequences. Furthermore, the creation of two different models, capable of describing the soil-structure interaction of pipelines and post-liquefied soil was the main objective of this thesis.

The means by which these models were created was the implementation of the spring and dashpot method. More specifically, Kelvin-Voigt models were used for the ground's behaviour to be modelled. These models required two main parameters to be specified in each case, the spring coefficient (k) and the dashpot coefficient (c). In order for the spring coefficient to be determined, the creation and usage of post-liquefaction p-y curves was deemed necessary while the problem specific dashpot coefficients used, had previously been determined by means of physical modelling. The ground profile consisted of fully saturated loose sand and the pipes investigated had diameters of 110, 160 and 200mm.

The first model was a single degree of freedom one, with that being the vertical. As for the second one, it was a multi degree of freedom one. More specifically, it consisted on two degrees of freedom, the vertical and horizontal ones. The results of these models were validated by comparison to previous studies and further investigation of affecting parameters was carried out. More specifically, the way and the degree up to which several parameters of both ground and structure characteristics affect their interaction were investigated. More specifically, the first parameters considered were the pipelines' diameter as well as their weight, resulting from their geometry and transported material. Next, the effect of the pipelines' burial depth was considered and then, the effect of the soil's initial stiffness. Finally, the effect of the dashpot coefficient was investigated for the multi degree of freedom models. A comparison between single and multi-degree of freedom solution results was also carried out.

The results of this study were validated by comparison to previous research findings. Most results and conclusions were in complete agreement with the so far existing bibliography. However, what was found to be inaccurate was the previously determined dashpot coefficient for 110mm diameter pipelines and hence, these were left out of scope of study.

Table of Contents

Table of Figures

Table of Tables

1 Introduction

1.1 Scope of Study

1.1.1 Background Information

In 1952, traces of gas were found in Lower Permian Sands from a well drilled in the area of Harkstede, Netherlands. After two previous failed attempts, the Dutch Petroleum Company (NAM) made its first successful drilling on July 22, 1959, followed by two more during the same year some kilometres apart from each other. The depth of the water-gas interface was found to be the same in all three cases and it was confirmed that the largest gas field in Europe, and tenth largest in the world, had been discovered with a total capacity of 2800 billion m³.

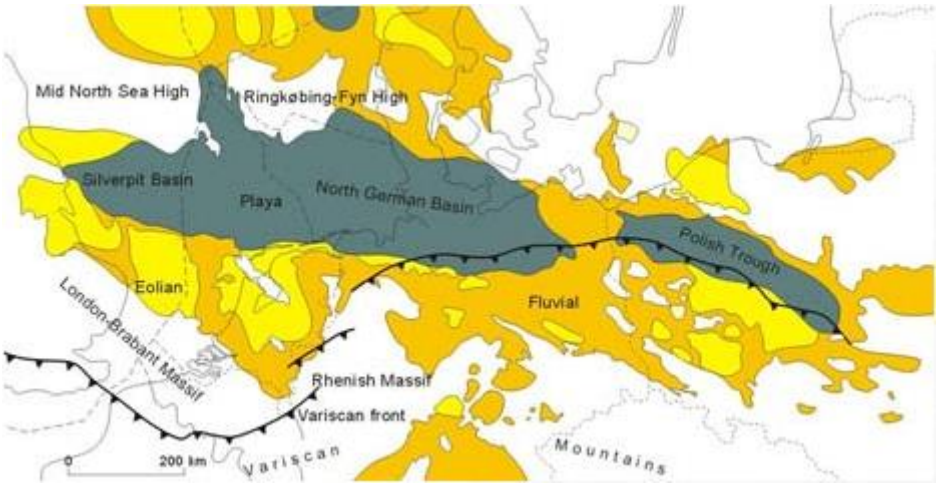

Figure 1.1: Geological morphology of the area (NAM)

Gas extraction started back in 1963 with a yearly production of 50 – 80 billion m³ and a significant created revenue. However, the extraction started to gradually reduce the gas pressure within the rock reservoir and create instabilities along fractured areas. The result was rock movement along fracture zones, which lead to generation of earthquakes. It is worth mentioning at this point how these earthquakes have been product of natural resources' exploitation by humans and hence, they are referred to as induced earthquakes.

Table 1.1: Rough comparison between tectonic and induced earthquakes

Feature	Tectonic Earthquake	Groningen Induced Earthquake
Epicentre (km)	>20	2
Duration (s)	10 – 60	±2
Frequency	-	Relatively High
Moment Magnitude Scale	3.0 – 9.0	2.0 – 4.0
Peak Accelerations	Multiple	1 - 2

On the other hand, tectonic earthquakes are a natural phenomenon of dynamic excitation resulting by, as the name suggests, movement of the earth's tectonic plates. Tectonic and induced earthquakes are fundamentally different as demonstrated in table 1.1.

Furthermore, occurrence of these earthquakes has already caused damage on structures located in nearby urban environments. Some examples of these structures are foundations and pipelines where the latter are a multipurpose means of material transportation in order for fresh and waste water, as well as oil and gas to be distributed.

When the vulnerability of buried pipelines against liquefaction is considered, it can be deduced how their failure can be the cause of soil and aquifer contamination with materials such as oil or chemicals which are being transported. In addition to this, such an event would produce great financial discomfort to the proprietor be held responsible for the restoration of the environment as well as their damaged network.

Hence, a great lot of proprietors and suppliers would be interested in understanding how significant damage can be caused to their networks by liquefaction and its post-occurrence as well as construction ways which minimize the expected damage.

1.2 Problem Definition

Dynamic excitations can be imposed to a given ground domain by earthquakes, either imposed or tectonic ones. Given the appropriate ground profile and conditions, these excitations can cause liquefaction and as a result, pipe failure. Liquefaction is a phenomenon during which pore pressure within the soil's skeleton faces such an increase that makes the ground completely lose its stability and behave similarly to the way that a viscous fluid would and is described in greater depth within this report.

The point at which soil has reached a complete loss of stability i.e. an effective stress equal to zero, is the beginning of the post-liquefaction state while the ending point is when effective stress starts building up once again.

The excess pore pressure present during these processes is proven to cause floatation, or uplift, of buried pipelines, which can get them reach significant deformations up to ground surface. Such deformations may vary from point to point and are called differential displacement. These deformations can cause failure of buried pipelines and create the need for a model which can realistically describe them to be created.

However, the main limitation is the lack of information for accurate modelling to be achieved.

1.3 Objective

As induced earthquakes are not very likely to trigger liquefaction and its post state effects, the objective of this report is the creation of a multi-functional model which, identifies whether liquefaction occurrence is or is not expected.

After that, expected deformations and pipe uplift during post-liquefaction can be calculated for a variety of cases through a fully automated algorithm and with main interest in the induced earthquakes of the Groningen area.

Furthermore, the factors which play a role to the degree up to which pipe uplift occurs are going to be investigated and preventing mechanisms are going to be identified.

Finally, it is worth mentioning that a very powerful and useful tool is going to be created which can help the production of pipeline force-displacement relationships for varying ground conditions.

2 Literature Review

2.1 What is Liquefaction

According to chapter 4 of "Eurocode 8: Design of structures for earthquake resistance Part 5: foundations, retaining structures and geotechnical aspects", liquefaction is defined as "a decrease in the shear strength and/or stiffness caused by the increase in pore water pressures in saturated cohesionless materials during earthquake ground motion, such as to give rise to significant permanent deformations or even to a condition of near-zero effective stress in the soil". It would be worth mentioning that static liquefaction is also possible and will be described in more detail later on.

In this chapter, the previously stated definition will be discussed in further depth in order to gain better understanding of main points as to how and when the phenomenon of liquefaction occurs as well as what impact it might have on the soil mass and its surrounding structures.

2.1.1 How Liquefaction Occurs

The first thing that has to be specified as to when liquefaction is most likely to occur is the geological and water-table conditions (Sahoo, Reddy, & Sukhija, 2007). Furthermore, most prone to liquefaction are cohesionless soils which can be characterised by their loosely packed state and their fine grains. An additional requirement is that the soil mass of interest is saturated and, most commonly, at shallow depths. From the requirements listed above, it is becoming evident that the most susceptible to liquefaction kind of material is loosely packed coarse silt to fine sand and saturated as stated before (Y. Huang & Yu, 2013). However, recent studies suggest some peculiar cases of liquefaction. These will be discussed in greater depth at a following paragraph of this chapter.

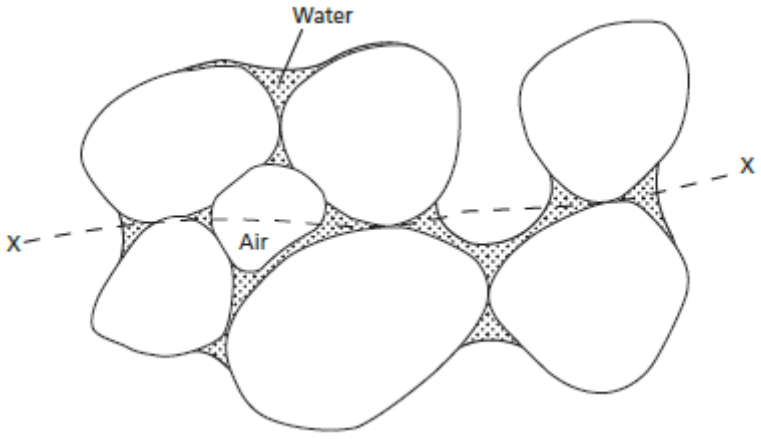

Figure 2.1: Partially saturated soil (Knappett & Craig, 2012)

When discussing liquefaction, a distinction can be made between static, or seepage-induced liquefaction, and dynamic/seismic one. The common factor in both cases is the influence that seepage has on effective stress. More specifically, if a soil domain is considered, there would be water seeping through its pores. This water movement would cause viscous friction resulting in the production of frictional drag acting upon the solid particles of the soil's grain skeleton. The resulting force would then be called seepage and combined with gravitational forces acting upon the soil mass is the resultant body force (Knappett & Craig, 2012). It is worth mentioning how this latter force governs the effective stress of the discussed domain where seepage takes place.

2.1.2 Seepage Induced (Static) Liquefaction

First, seepage induced liquefaction will be discussed. In order for the occurrence of this phenomenon to be clarified, the concept of critical hydraulic gradient (i_{cr}) would have to be introduced. Where:

$$i_{cr} = \frac{\gamma'}{\gamma_w} = \frac{G_s - 1}{1 + e} \tag{2.1}$$

And with:

- γ' being the effective unit weight
- γ_w being the unit weight of water
- G_s being the specific gravity
- e being the void ratio

According to (Knappett & Craig, 2012), the value for the critical hydraulic gradient is approximately 1.0 for most soils and when the hydraulic gradient of the material is equal to i_{cr}, the effective stress acting on any plane will also be zero due to upward seepage forces cancelling out the gravitational ones. This would cause the contact forces between sand particles to be equal to zero as well and the sand itself to have no strength. At this state, it can be said that the soil is liquefied and now acts as a viscous fluid instead. If the critical hydraulic gradient is exceeded, the soil would appear boiling and particles would be moved upwards due to flow of water. Finally, it is worth mentioning that in clay materials, the hydraulic gradient reaching the critical value derived from the above equation may not necessarily lead to it liquefying.

2.1.3 Seismic (Dynamic) Liquefaction

In the previous case, of static liquefaction, it was explained that the soil liquefied due to seepage. This was because the seepage force would create higher, excess, pore water pressure which would reduce the effective stress within the soil to zero. However, it is possible that the pore water pressure of soil can be increased due to cyclic loading, imposed to the material by dynamic loading due to seismic activity. When soil is not densely packed and undergoes cyclic shearing, it tends to contract. This would cause the void ratio (e) to be reduced. As a result, if this happens rapidly, the water within the soil might not have enough time to escape the pores in which it is located. This event, along with the contraction mentioned before would once again create excess pore water pressure due to the incompressibility of water (Knappett & Craig, 2012).

If a uniform soil layer with the water table at its upper surface is considered, the total stress will be given for any depth (z) by

$$\sigma_v = \gamma_{sat} * z \tag{2.2}$$

However, the pore water pressure is formed by two different components, which are the hydrostatic pressure (u_s) that was present initially before the soil was loaded and the excess part (u_e) which is imposed by the seismic motion's dynamic load. After defining these parameters, the critical excess pore water pressure at the point in time when liquefaction starts occurring u_{el} can be defined as follows:

$$u = \sigma_v \tag{2.3}$$

$$u_s + u_{el} = \gamma_{sat} * z$$

$$\gamma_w * z + u_{el} = \gamma_{sat} * z$$

$$u_{el} = \gamma' z \tag{2.4}$$

The equation presented above demonstrates that in order for liquefaction to take place, the excess pore water pressure has to be reach the same value as the one of the initial effective stress that was existing in the ground prior to cyclic loading.

Figure 2.2: Foundation failure due to liquefaction, Niigata 1964 (Knappett & Craig, 2012)

Several factors can enhance the potential of dynamic liquefaction. Some of these factors are characteristics of a seismic event, such as its magnitude and the location of the epicentre. More specifically, the higher the magnitude and the closer the epicentre is to the area of interest, the higher the potential of liquefaction is (Y. Huang & Yu, 2013). According to (Knappett & Craig, 2012), if a datum is considered at the soil's surface, the following is valid.

$$u = \gamma_w * (h + z) \tag{2.5}$$

$$h = \frac{\gamma_{sat} - \gamma_w}{\gamma_w} * z$$

$$\frac{h}{z} = \frac{\gamma'}{\gamma_w} \tag{2.6}$$

The previous expression demonstrates how there will be a positive hydraulic gradient between the surface and a point at depth z within the soil mass when liquefaction is triggered. In addition to this,

it can be observed that this expression is the same as the one of the critical hydraulic gradient mentioned previously for static liquefaction and in this case, combining what has been derived gives:

$$u_{el} = i_{cr} * \gamma_w * z = \frac{\gamma_w * (G_s - 1)}{1 + e} * z \tag{2.7}$$

It is also worth mentioning how soil near the top surface of a soil mass would present a lower density due to higher void ratio (e). Furthermore, during the event of an earthquake, the dynamic loading would, most of the time, travel from the earth's crust towards the soil surface. The combination of these two factors would mean that liquefaction starts from the surface of a soil mass and continues up to a certain depth. Also, it is clear that the effective stress within a soil domain increases linearly with depth and hence, from what has been mentioned so far, it can be safely stated that along with increasing depth, the amount of excess pore pressure needed to trigger liquefaction also increases. Finally, the last equation concerning u_{el} states how loose soils, which are characterised by higher values of pore pressure (e), would require lesser excess pore pressure than denser ones in order for liquefaction to be triggered (Knappett & Craig, 2012).

Finally, (Chian, Tokimatsu, Asce, Phani, & Madabhushi, 2014) state the parameter of liquefaction ratio (r_u) which is defined as the change of pore water pressure (Δu) divided by the initial vertical effective stress of the soil (σ'_v) ($r_u = \Delta u/\sigma'_v$). It can be said that full liquefaction then is reached when $r_u = 1$ and partial liquefaction is present when r_u is less than one.

2.1.4 Wave induced liquefaction

(Sumer, Fredsøe, Christensen, & Lind, 1999) investigated floatation of buried pipelines in marine environments as can be seen in figure 2.3. Furthermore, dynamic stresses can be caused in the soil from waves. This investigation concluded how if a certain wave height is reached, excess pore water pressures can be accumulated and build up to full liquefaction.

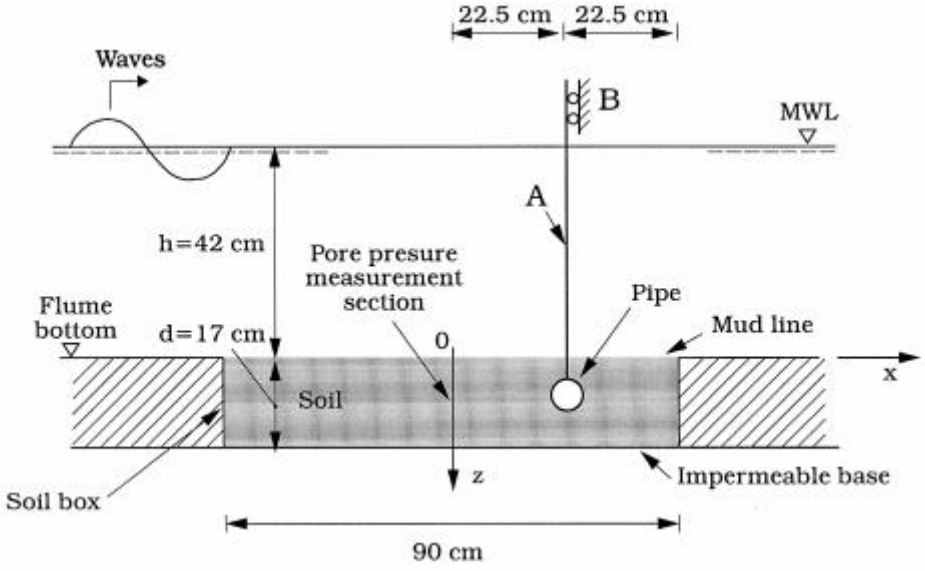

Figure 2.3: Wave induced liquefaction (Sumer et al., 1999)

2.2 Liquefaction Related Phenomena

In the previous paragraph, it was discussed how boiling can occur if the corresponding critical hydraulic gradient is exceeded. However, this is not the only phenomenon that could be expected from liquefaction. Events such as ground cracks and lateral spread should be also expected. In the paragraphs bellow, the typical phenomena which correspond to liquefaction will be analysed, in order to gain a better understanding of how the ground is altered in the post-liquefaction state.

2.2.1 Sand Boiling

It has previously been described what sand boiling is as well as why and how this phenomenon occurs. However, some further discussion can take place about the boiling formations. Furthermore, the particles that move upwards are, most commonly, originating from shallow depths of the soil and can form elements of different shape and size during earthquakes. Based on how the liquefied soils eject through the upper layers, sand boiling formations can be classified in two different categories (Y. Huang & Yu, 2013). These categories differ mainly on the shape of the element's formation as well as the way in which the material has reached ground surface. The first category includes flat cone sand volcanoes. The diameter of those structures may differ from few centimetres up to meters (Y. Huang & Yu, 2013). As for the second category, it includes soil particles which have reached ground surface through cracks, formed by the earthquake itself. These cracks usually expand for several meters in width and significantly less in depth and length.

Figure 2.4: Flat cone sand volcano [John Tinsley, U.S Geological Survey]

It is worth mentioning at this point how sand boiling acts as a relief mechanism for the ground that is undergoing liquefaction. As excess pore pressure is being generated, it might follow a path of least resistance and dissipate as shown in figure 2.6. More specifically, the inhomogeneity of soil properties can result to a different fluid extrusion rate and cause the fluid to migrate towards more pervious and/or lower pressure zones (Yang & Elgamal, 2001). Finally, the excess pore pressure relief offered by sand boiling acts as a mitigating measure for lateral spread that tends to occur due to liquefaction.

Figure 2.5: Ground cracks [http://nisee.berkeley.edu]

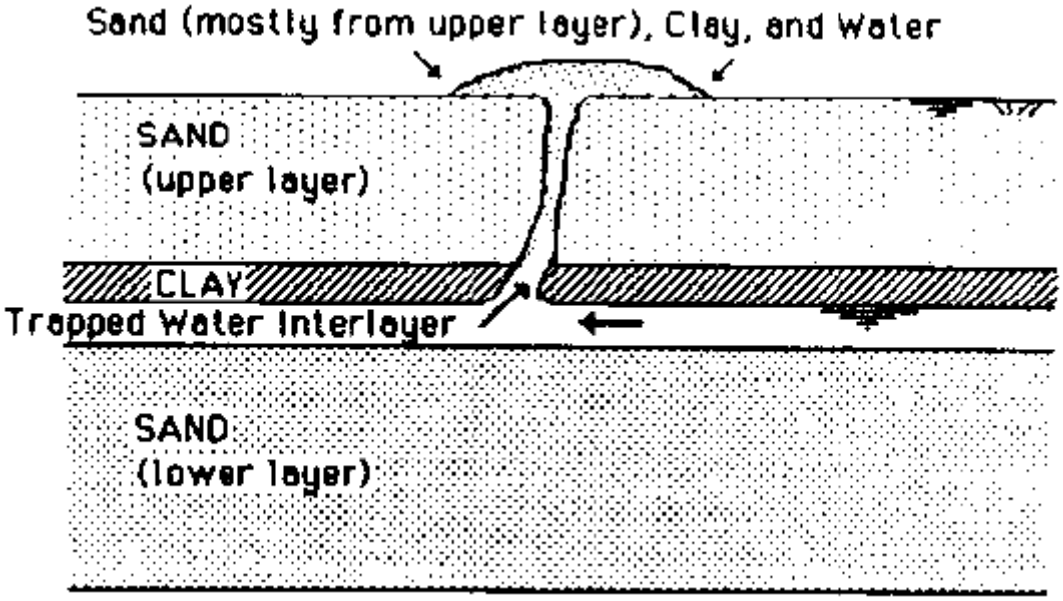

Figure 2.6: Excess pore pressure relief mechanism (Yang & Elgamal, 2001)

2.2.2 Lateral Spread

In the case where sand boiling does not take place, lateral spreading is a potential hazard for the soil mass. Lateral spread consists of surficial soil blocks displacing horizontally, down a slope or towards a free surface along a shear zone, which was formed within the liquefied zone (Bartlett & Youd, 1995). It is clear, from what has been stated so far, that this horizontal displacement is made possible due to the decrease of the liquefied material's shear strength to nearly zero. Lateral spread typically causes displacement that ranges from a few centimetres to several meters and can cause considerable damage to nearby structures. However, lateral deformation will in general create sand boiling for the interlayer water to escape (Yang & Elgamal, 2001).

2.3 Liquefied Soil

The subject of soil masses, which have undergone liquefaction has been studied and discussed in various published scientific papers so far. Furthermore, liquefied sand behaves as a non-Newtonian fluid in which the viscosity appears to be decreasing with increasing shear strain rate [Hwang et al., 2006]. It is worth mentioning how two approaches have been used in the liquefied soil's behaviour, these are a viscous fluid and a pseudo-plastic fluid ones. (Hwang, Kim, Chung, & Kim, 2006) gathered a significant amount of previous experimental research and compared the results, plotted in a relative density (D_r) – viscosity space, as seen in figure 2.7.

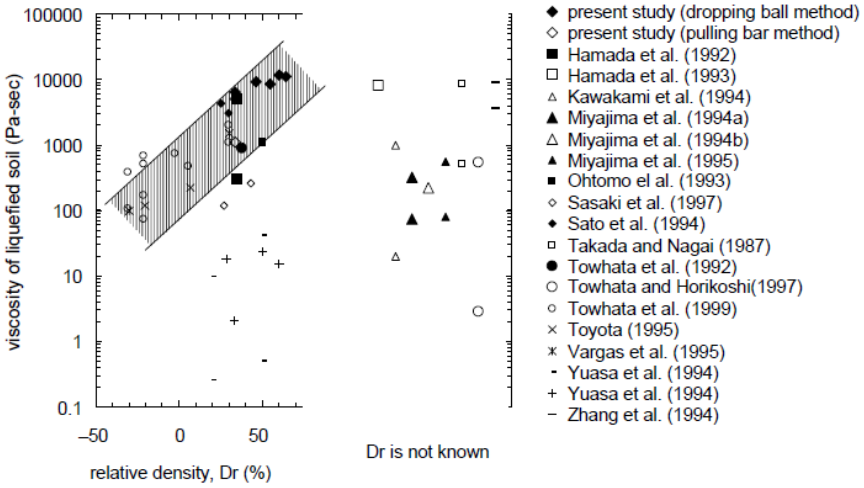

Figure 2.7: Viscosity value results suggested by other researchers (Hwang et al., 2006)

The types of tests which lead to the results presented in this figure were analytically:

Figure 2.8: Types of tests and method of liquefaction to gain viscosity (Hwang et al., 2006)

Symbol	Researcher	Type of test	Method of liquefaction
♦	Present study (sinking ball test)	1 g, subsidence of sphere	Impact
◇	Present study (pulling bar test)	1 g, pulling cylindrical bar	Boiling
■	Hamada and O'Roorke [2]	1 g, pulling sphere	–
□	Hamada et al. [13]	1 g, pulling pipe, pile, sphere	–
△	Kawakami et al. [9]	1 g, shaking table test	Shaking
▲	Miyajima et al. [15]	1 g, subsidence of sphere	Shaking
△	Miyajima et al. [16]	1 g, pulling sphere	Boiling
▲	Miyajima et al. [8]	1 g, subsidence of sphere	Shaking
■	Ohtomo el al. [17]	1 g, pulling sphere	Boiling
◇	Sasaki et al. [18]	1 g, subsidence of foundation	Shaking
♦	Sato et al. [19]	50 g, flow of slope	Shaking in centrifuge
□	Takada and Nagai [20]	1 g, subsidence of sphere	Shaking
●	Towhata et al. [4]	Analysis of the progress of lateral deformation of liquefied slopes	–
○	Towhata and Horikoshi [21]	Prototype subsidence of building foundation	1964 Niigata earthquake
○	Towhata et al. [22]	1 g, pulling pipe	Shaking
×	Toyota [23]	1 g, flow of slope	Impact
*	Vargas and Towhata [10]	1 g, pulling pipe	Shaking
-	Yuasa et al. [24]	1 g, pulling sphere	Shaking
+	Yuasa et al. [24]	1 g, viscometer	Boiling
–	Zhang et al. [25]	undrained triaxial test	–

What can be observed in the figure and table presented above is how the relationship between viscosity and relative density of a liquefied soil remain constant, no matter the researcher or the experimental procedure selected each time. This relationship is that viscosity tends to increase with relative density.

2.4 Liquefaction Potential

A fundamental question raised at the beginning of every simulation, regarding this paper, is whether the soil and loading conditions are adequate to produce liquefaction. Furthermore, in everyday application of this problem, the first thing that would be done is specification of the ground's liquefaction characteristic. This could be done by usage of the most commonly used ground investigation techniques, which are Standard Penetration Testing (SPT) and Cone Penetration Testing (CPT).

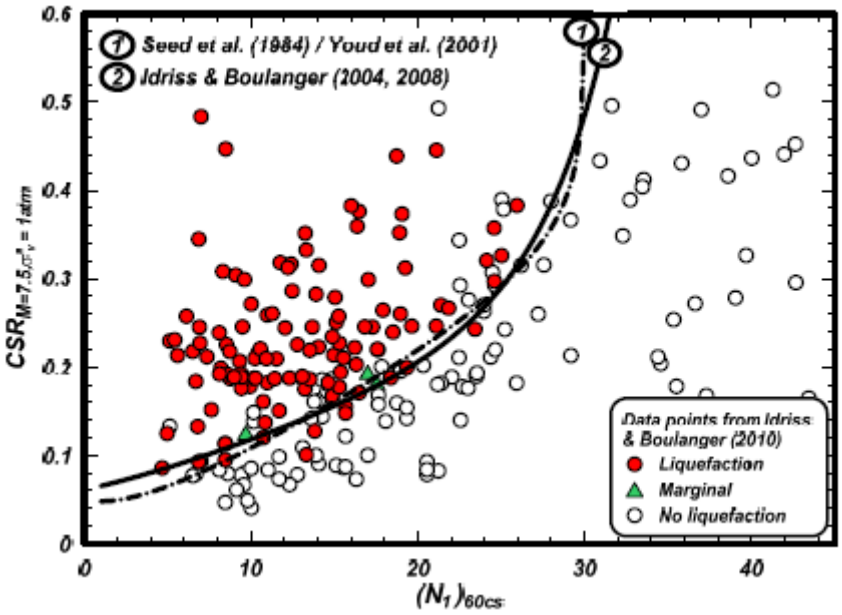

Figure 2.9: SPT based liquefaction potential curves from processed case histories (Boulanger & Idriss, 2014)

There have been countless efforts made by researchers so far in order for this problem to be solved. Furthermore, the development of SPT and CPT correlations began in Japan during the 1960^{s} and progressed up to the landmark work of Seed et al. in 1984, which was set as a standard for engineering practise during the next two decades (Boulanger & Idriss, 2014). The most notable updates made in the SPT and CPT procedures upon this matter were the ones by Idriss and Boulanger and the comparison between the aforementioned studies can be seen in figures 2.9 & 2.10.

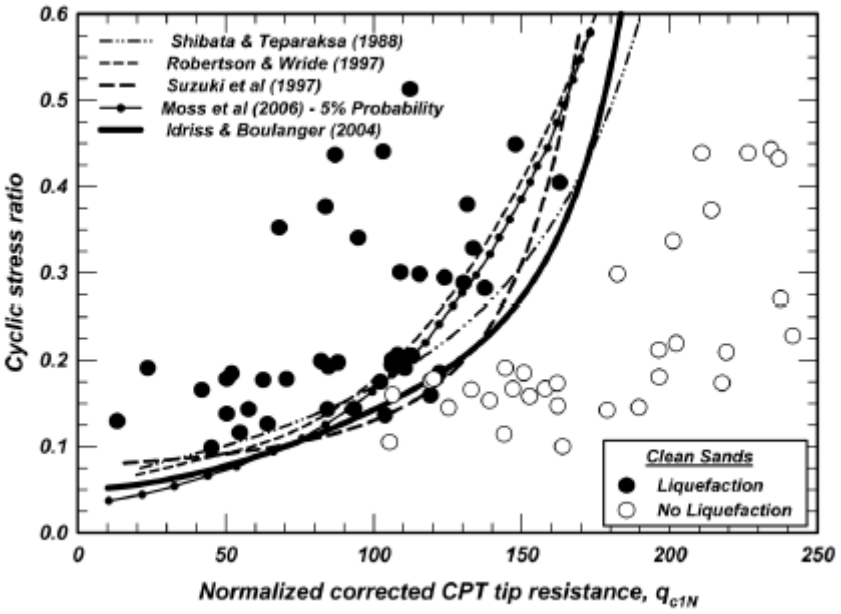

Figure 2.10: CPT based liquefaction potential based on clean sand case histories (Boulanger & Idriss, 2014)

It is worth mentioning at this point how the Cyclic Stress Ratio (CSR) is one of the main parameters when investigating liquefaction potential. The (Boulanger & Idriss, 2014) method, which is their most up to date one, has been used as a reference solution within the scope of this study.

Now, as far as the calculation process is concerned, the CSR ratio for a specific depth (z) has traditionally been expressed as 65% of the maximum cyclic shear stress ratio within a representative value. That is:

$$CSR_{M,\sigma'v} = 0.65 * \tau_{max} / \sigma'_v \quad (2.8)$$

Where τ_{max} is the maximum shear stress imposed by the earthquake and σ'_v is the vertical effective stress. It is worth mentioning, that as the CSR subscripts suggest, the result is calculated for a pre-specified value of earthquake magnitude (M) and vertical stress (σ'_v). The aforementioned percentage of 65% was suggested by Seed and Idriss in 1967 and has since then been used. Furthermore, the parameter τ_{max} can be specified from dynamic response analyses, which should include a satisfactory amount of site characterisation parameters as well as dynamic acceleration time series (Boulanger & Idriss, 2014). If the amount of these parameters is not satisfied, the following formula can be used for the determination of SCR:

$$CSR_{M,\sigma'v} = 0.65\ (\sigma_v/\sigma'_v)*(\alpha_{max}/g)*r_d \quad (2.9)$$

Where: σ_v is the total vertical stress at depth z, α_{max}/g is the maximum horizontal acceleration at ground surface and r_d is a shear stress reduction factor accounting for the ground's dynamic response (Boulanger & Idriss, 2014). As for the formulation of the remaining parameters:

$$r_d = \exp[\alpha(z) + \beta(z)*M]$$

$$\alpha(z) = -1.012 - 1.126 \sin(z/11.73+5.133)$$

$$\beta(z) = 0.106 + 0.118 \sin(z/11.28 + 5.142)$$

The next step in the analysis of liquefaction potential is the determination of the Cyclic Resistance Ratio (CRR). (Boulanger & Idriss, 2014) propose that the value of CRR for a magnitude (M) of 7.5 and a stress (σ'_v) is given from the relationship:

$$CRR_{M=7,5,\sigma'v=1} = CSR_{M,\sigma'v} /(MSF * K_\sigma) \quad (2.10)$$

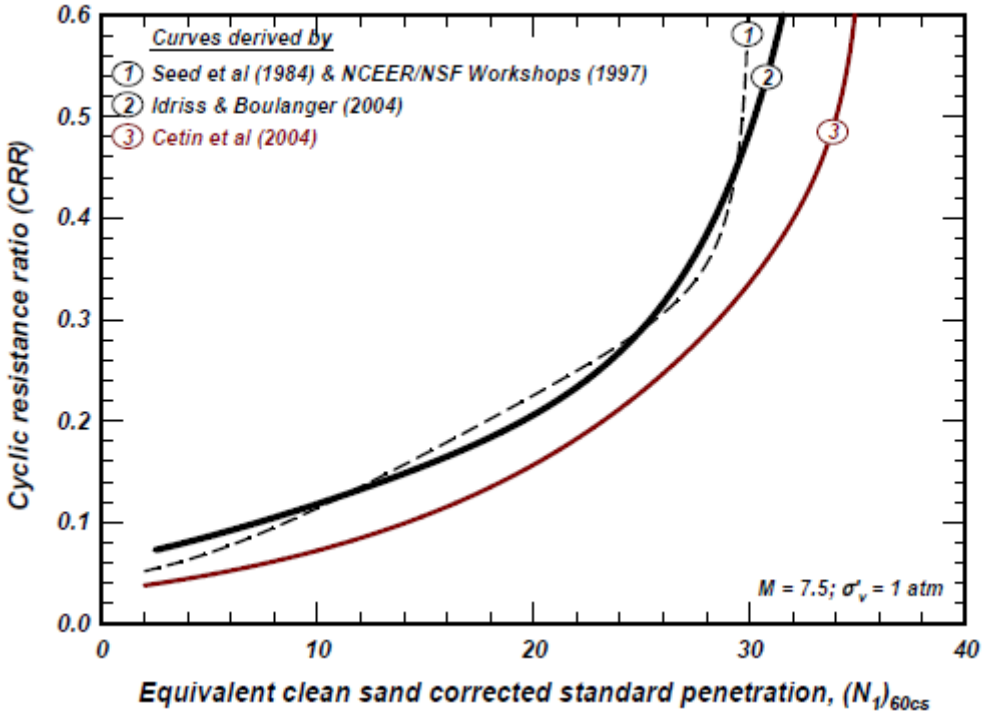

Figure 2.11: Example CRR correlations (Idriss & Boulanger, 2010)

It is explained in (Idriss & Boulanger, 2010) how the Magnitude Scaling Factor (MSF) represents a combination of dynamic ground motion and the behaviour of cohesionless soil for both CPT and SPT. This parameter is investigated in (Boulanger & Idriss, 2014) and found to be:

$$MSF = 6.9 * \exp(-M/4) - 0.058 \quad (2.11)$$

Where M is the desired earthquake magnitude MSF must be equal or less than 1.8. It is interesting to note at this point that (Idriss & Boulanger, 2010) also found the following relationship to be valid for SPT tensing:

$$MSF = 17.84 * (M)^{-1.43} = (M/7.5)^{-1.43} \quad (2.12)$$

Finally, K_σ was introduced in (Boulanger & Idriss, 2014) as a factor which describes effective overburden stress as:

$$K_\sigma = 1 - C_d * \ln(\sigma'_v/P_a) \quad (2.13)$$

With $C_d = 1 / (37.3 - 8.27(q_{c1Ncs})^{0.264})$ for CPT and $C_d = 1 / (18.9 - 2.55\ SQRT(N_1)_{60cs})$ for SPT.

Finally, the Factor of Safety (FS) for specified M and σ values can be described as $FS = CRR_{M,\sigma'v} / CSR_{M,\sigma'v}$.

2.5 Liquefied Soil as a Non-Newtonian Fluid

It was mentioned before, how the behaviour of liquefied soil can best be described as the flow of a non-Newtonian fluid and thus, it is found beneficial for the difference between Newtonian and non-Newtonian fluids to be described in order for better understanding of the material's behaviour to be obtained.

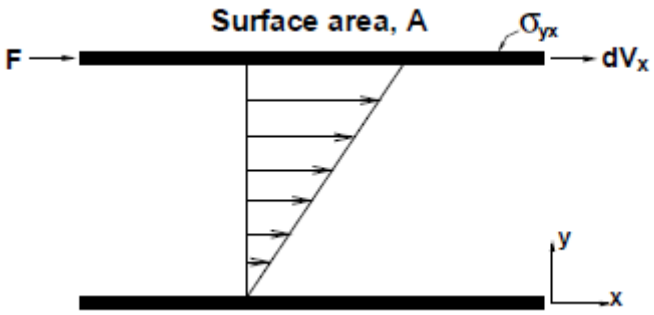

Figure 2.12: Schematic representation of unidirectional shear flow (Chhabra, 2010)

The first category to be discussed is Newtonian fluids. According to (Chhabra, 2010) in simple shear, which is described in figure 2.12, a linear response between applied shear stress and shear rate is the main characteristic of a Newtonian fluid. That is:

$$\sigma_{yx} = F/A = \eta\,(\gamma_{yx})' \qquad (2.14)$$

As for non-Newtonian fluids, according to (Chhabra, 2010), the simplest possible deviation from the Newtonian behaviour, is how the simple shear data (σ – $(\gamma)'$) does not pass from the axes origin (0, 0) and/or does not show a linear relationship between shear stress and shear rate. This relationship is very well described graphically in the following figure.

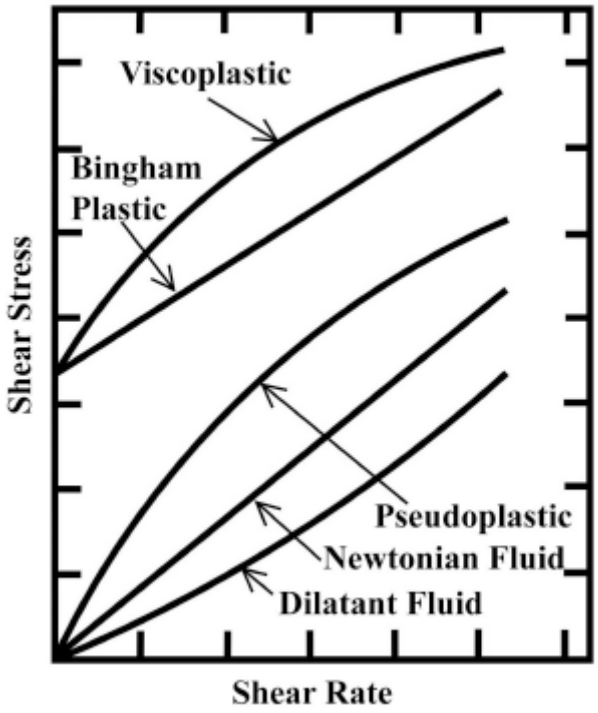

Figure 2.13: Qualitive flow curves for different types of non-Newtonian fluids (Chhabra, 2010)

2.6 Failure Mechanisms

2.6.1 Failure Mechanisms in Non-Liquefied Sand

As far as soil-structure interaction is concerned thus far, liquefaction can be the triggering cause of a given structure's failure mechanisms. In this study, the structures of interest are buried pipelines and their most common failure mechanisms will be discussed. However, failure mechanisms in liquefied sand are more complex and will be discussed later on in this paper.

In order to achieve better understanding of the uplift failure phenomenon itself, it was considered beneficial to analyse the general failure mechanisms before getting into further detail about how environmental parameters affect its development. However, this will be discussed in the course of this chapter.

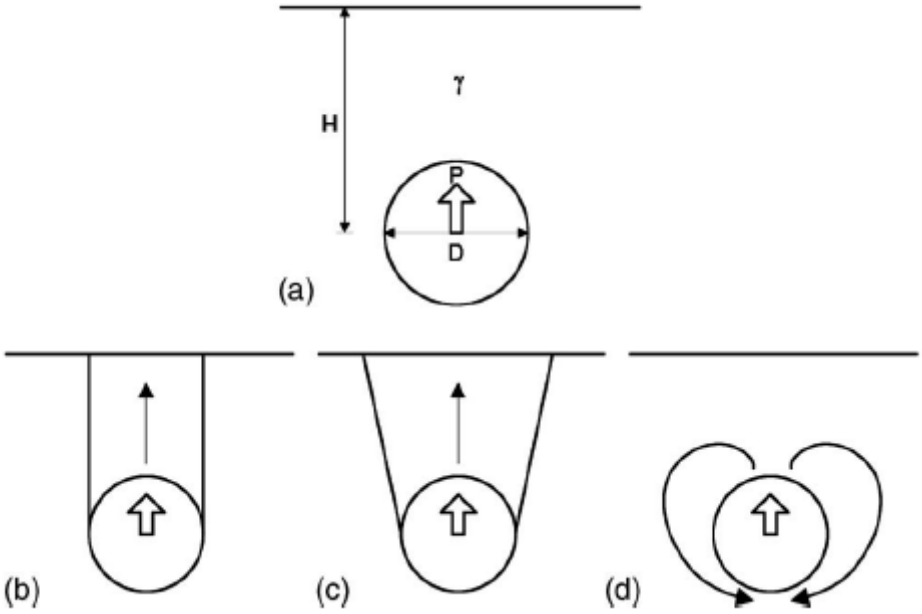

Figure 2.14: Uplift mechanisms of buried pipes in sand: (a) Problem geometry; (b) sliding block with vertical slip surfaces; (s) sliding block with inclined slip surfaces; (d) flow around (Cheuk, White, & Bolton, 2008)

According to (Cheuk et al., 2008), in figure 2.14, the geometry of a buried pipe is defined in part (a). Following in (b), it is stated how the uplift mechanism involves a sliding block, which is bounded by a pair of shear bands. In (c) it can be seen how the inclination of the shear bands is similar to the one of the soil's dilation angle, it is worth mentioning that (Berghe, Cathie, & Ballard, 2001) confirmed this mechanism through finite element analysis. Part (d) of the above figure presents a flow around mechanism which is typically encountered in very loose sand materials (Cheuk et al., 2008). However, it is possible that the flow around mechanism is observed in initially dense models beyond peak resistance (Cheuk et al., 2008).

(Cheuk et al., 2008) also discussed the influence of material properties on vertical displacement as well as the failure mechanism's propagation. In figure 2.15, three cases are being presented. Figure (a) is at peak resistance, while (b) and (c) are post-peak and more specifically, (b) at 0.12D vertical displacement and (c) at 0.5D. As can be seen in all cases, the influence of the soil density upon vertical displacement is becoming more and more evident approaching ground surface. It can also be observed how the inclination of the shear zone is dependent on the material density.

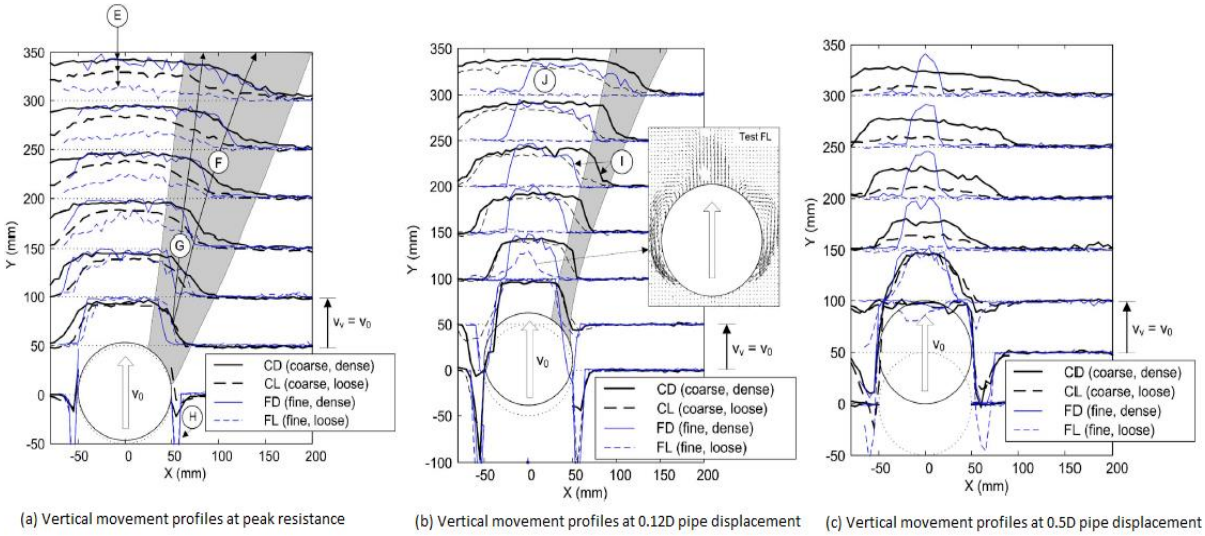

Figure 2.15: Vertical movement profiles (Cheuk et al., 2008)

The same study also concluded how, during pipe uplift, four key stages can be identified for the deformation mechanism. These are:

- Mobilization of peak resistance
- Onset of infilling beneath the pipe invert
- Post-peak shear band formation
- Flow around

It is worth mentioning that all of these stages are present in the above figure as well as how the effect of infilling is becoming clear at the soil-structure interface. Finally, the relationship between uplift resistance and vertical displacement was represented accordingly to the Figure 2.16, at right.

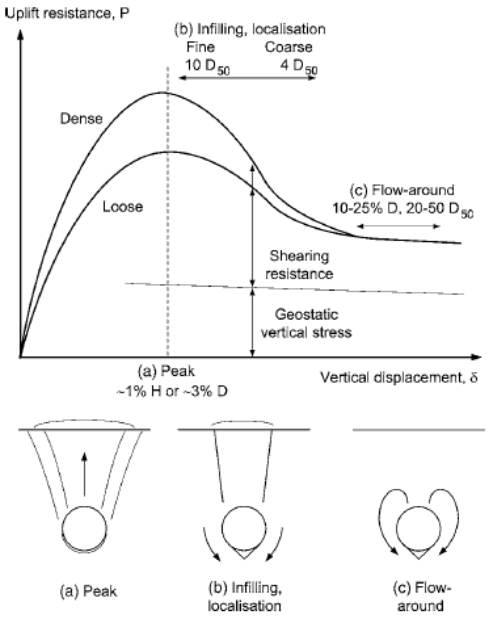

Figure 2.16: : Load-displacement response (Cheuk et al., 2008)

Finally, in the following two figures, test results can are presented and compared. Furthermore, at left there is a centrifuge test particle image velocimetry (PIV) result presented, which was done by Chian et al in 2014 and at 1.5D. At right, Cheuk et al's results can be seen from four different tests. It can be safely stated that the flow around mechanism is acting in all cases with slight geometrical alterations as all results can be well compared.

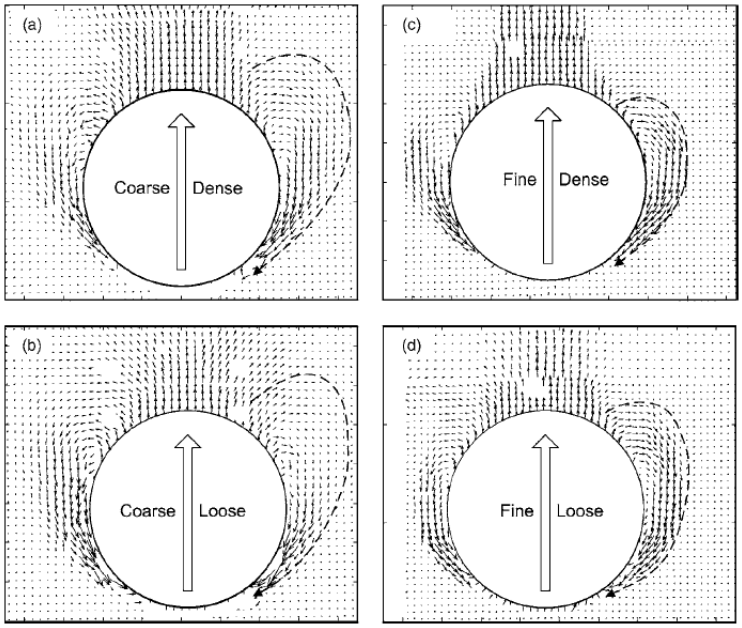

Figure 2.17: Pipe uplift test results (Cheuk et al., 2008)

In order for better visual understanding of the centrifuge tests held to be achieved, the apparatus which was used by Cheuk and colleagues is presented in figure 2.18.

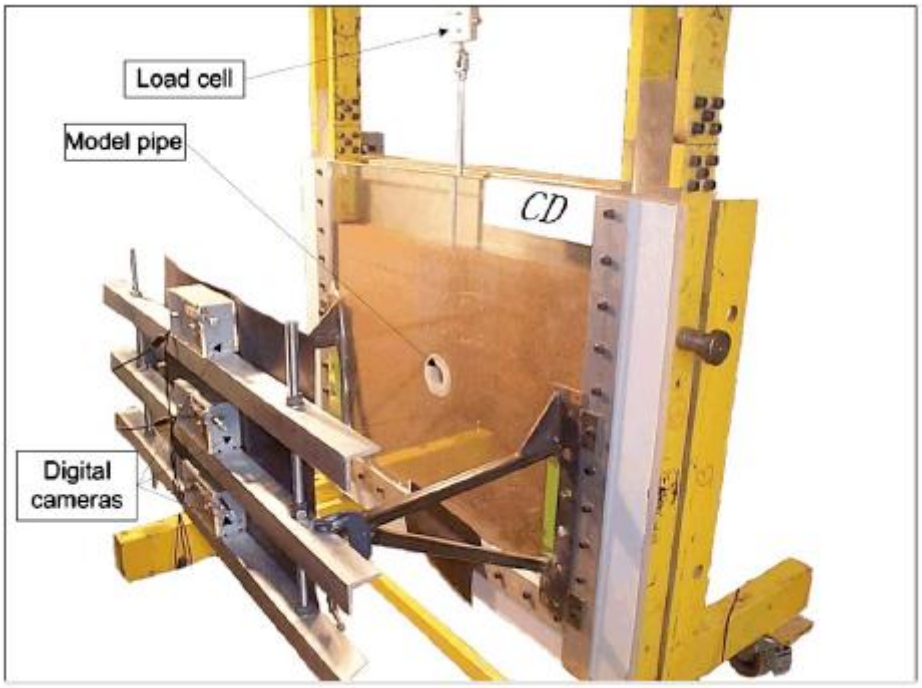

Figure 2.18: Centrifuge apparatus (Cheuk et al., 2008)

2.6.2 Failure Mechanisms in Liquefied Sand

The uplift behaviour of pipelines buried in liquefied sand is a process which results due to multiple forces and presents a high dependency on the one of excess pore pressure .Furthermore, during uplift the pipeline is forced to move vertically upwards as a result of excess pore pressure dissipating in this direction.

(B. Huang, Liu, Lin, & Ling, 2014) very well note how various factors have been thought to affect the extend up to which uplift will occur and after experimental research, it has been concluded that the ones which do so are burial depth, diameter, thickness and stiffness of the pipeline as well as type, liquefied area, stiffness and strength of the soil. It is also worth mentioning how the same study mentions that the most critical of the aforementioned factors are found to be the burial depth and diameter of the pipeline as well as the liquefied depth and stiffness of soil. As for the way in which the buoyancy force is most commonly calculated, that is:

$$F_{buoyancy} = \rho_{sat*} * g * V \quad (2.15)$$

Figure 2.19 presents the forces acting upon a buried pipeline during liquefaction induced by shaking in an experimental environment by (B. Huang et al., 2014). As can be seen, the failure mode adopted in this case is similar to the one of the sliding block, which is bounded by a pair of vertical share planes and was presented in figure 2.14 in the previous section of this report.

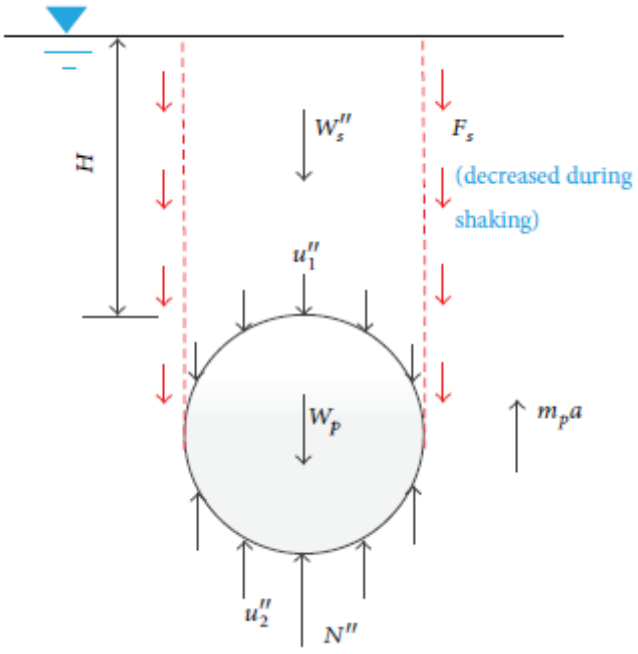

Figure 2.19: Schematic diagram of forces during pipe uplift (B. Huang et al., 2014)

The pipeline in the case presented here was not fixed, or provided a stabilizing force and hence, was able to move freely during experiments.

More specifically, the method of testing in this case was dynamic centrifuge with accelerations of 30g. Several accelerations were used as input for the dynamic excitation component of those tests and they are identified as figure 2.20 along with the observed outcomes of uplift occurring or not.

Test number	Seismic excitation			
	Seismic wave	Duration (s)	Amplitude (g)	Uplifting status
Test 1	Noise	30	0.02	
	Zhejiang seism wave		0.1	Remain still
	EL-Centro		0.1	Remain still
	Noise		0.02	
	Zhejiang seism wave		0.15	Sink slightly
	EL-Centro		0.15	Rise slightly
	Noise		0.02	
	EL-Centro		0.5	Rise
	Taft		0.4	Rise
	Noise		0.02	

Figure 2.20: Liquefaction occurrence outcome and input accelerations (B. Huang et al., 2014)

As for the ground conditions used, the liquefiable soil was a common practice Fujian Sand with a mean diameter D_{50} = 0.16mm, uneven coefficient C_u = 1, curvature coefficient C_c = 0.95 and finally, minimum and maximum void ratio coefficients of e_{min} = 0.62 and e_{max} = 0.95.

Samples were then created with a relative density D_r = 60% and tests were made. Figure 2.21 presents some of the results for different burial depths.

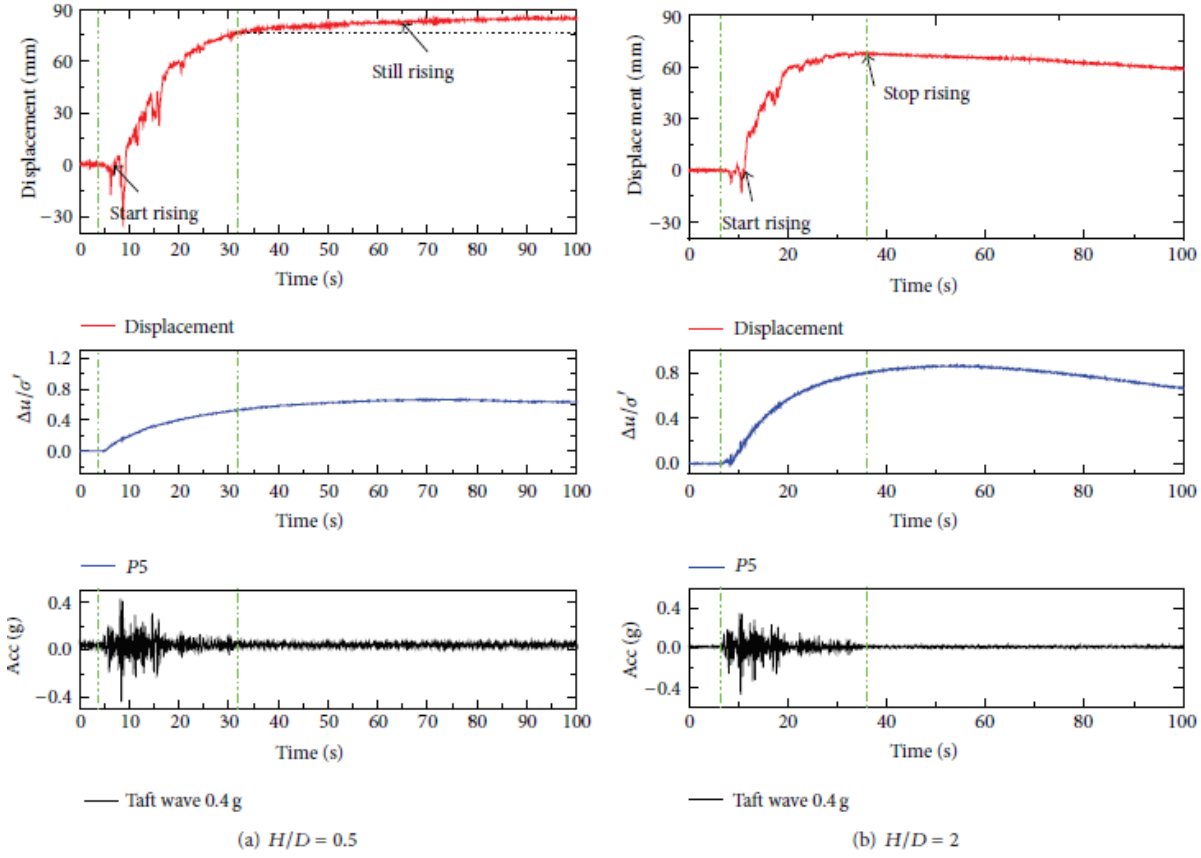

Figure 2.21: Uplifting displacement of pipeline at different burial depths (B. Huang et al., 2014)

As far as the force analysis is concerned, the pipe flotation studied is described by the equation:

$$m_p\alpha = F_s+\Delta W_s - \int_{-D/2}^{D/2}(\Delta u_2 - \Delta u_1)dD - \Delta N \quad (2.16)$$

Where W_s is the effective weight of the soil on top of the pipe, u_1 and u_2 are pore pressures occurring around it. The parameter N, which was shown in the schematic force diagram in figure 2.19 is the support provided by the pipe's underlying soil and has been eliminated as null during full liquefaction. F_s is a parameter which represents the frictional resistance provided to the pipe by the overlying soil. However, this parameter degrades during liquefaction and reaches 0 when the soil is fully liquefied. More specifically, this frictional resistance is specified in (B. Huang et al., 2014) as:

$$F_s = f_p\,[(D/H)*(H/D + 0.5)^2]*\sigma'_H DL \quad (2.17)$$

Where f_p is a parameter ranging between 0.4 and 0.6 for medium dense sand and σ'_H is the effective vertical stress of the pipe's overlying soil.

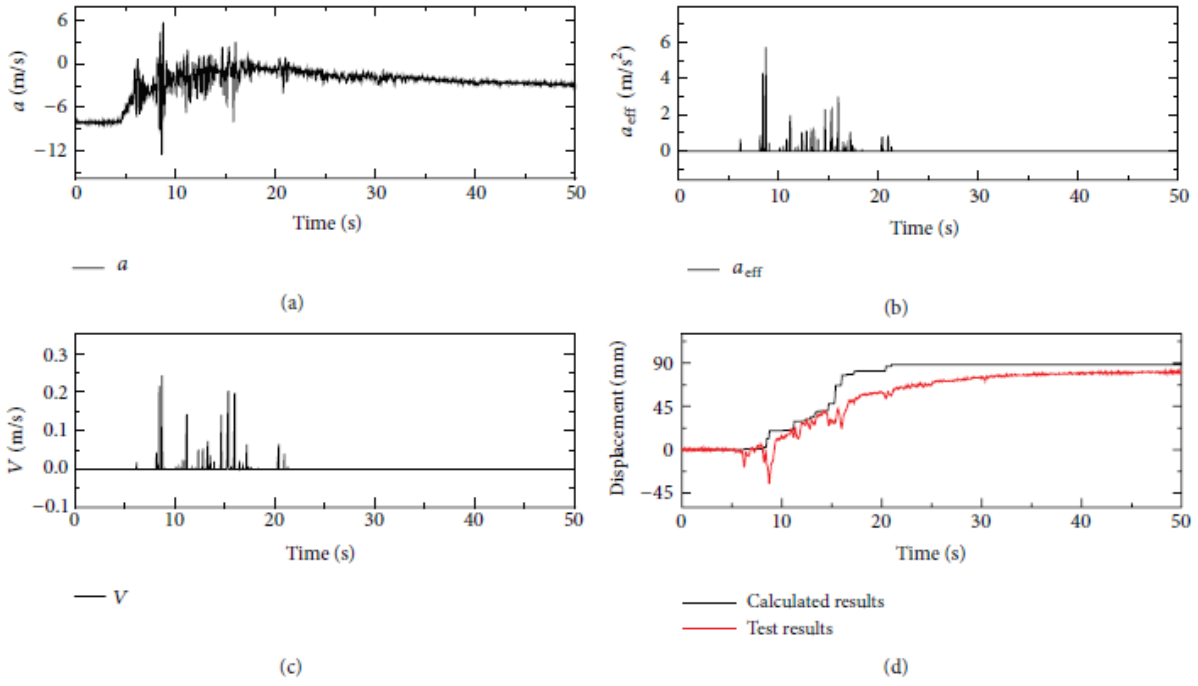

Figure 2.22: Calculated and measured acceleration, velocity and displacement of pipeline (B. Huang et al., 2014)

Finally, figure 2.22 presents the relationship between calculated and measured parameter results as well as a brief demonstration between parameter correlations.

2.6.3 Shallow and Deep Failure Approaches

In their study (Kouretzis, Krabbenhøft, Sheng, & Sloan, 2014) investigated the interaction effects of pipeline's vertical movement. Furthermore, instead of treating this problem as per common design practise and having the interaction force estimated by a shallow footing's bearing capacity theory, they assumed that the vertical behaviour mechanisms of a pipeline would be similar to circular pile's loading lateral ones. This approach was validated with the help of the finite element limit analysis method and some of the conclusions will be briefly presented in this section.

The most commonly used approach for the representation of a buried pipeline undergoing seismic loading is beam-nonlinear spring models, in which the pipeline is represented by beam elements while the reaction of the soil by non-linear springs and sliders in specified directions. However, (Kouretzis et al., 2014) very well notice an approach suggested by the established design guidelines of (ASCE-ALA, 2005) and the state of practice (O'Rourke & Liu, 2012) which treat the problem of vertical pipeline loading as a resemblance of that of a shallow strip footing. More specifically, these papers suggest that the common equations for shallow footings' bearing capacity are adequate to be used for the maximum force per unit length of the pipeline to be determined. That is:

$$Q_d = N_c c D + N_q \gamma' H D + N_\gamma \gamma (D/2)^2 \qquad (2.18)$$

Where D is the pipeline's diameter, H is the depth up to the pipeline's centreline, γ is the total unit weight of the soil, γ' the effective one, c is cohesion and N_c, N_q and N_γ are common bearing capacity factors.

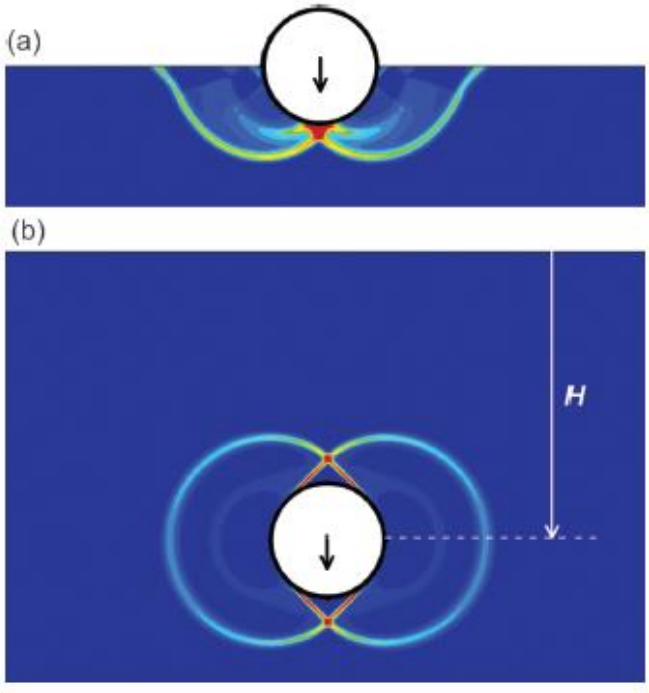

Figure 2.23: Shear strain contours defining the failure surface around a vertically loaded pipeline in uniform cohesive soil during undrained conditions. (a) is at H/D = 0 and (b) at H/D = 2.5 which is sufficient for deep failure (Kouretzis et al., 2014)

The theory is quite straightforward here and, as can be seen in figure 2.23, it is suggested that as the embedment depth (H) tends to zero, the pipeline is going to adopt the behaviour of a strip footing of width D.

However, when the embedment depth of the pipeline increases figure 2.23(b) a deep failure mode will be present where the maximum force to be developed on the pipeline will now be representative of the ultimate lateral bearing capacity of a horizontally loaded circular pile in uniform ground (Kouretzis et al., 2014). It is worth mentioning at this point how the latter is the case within the limits of this study as will be numerically presented later on.

2.7 Beam on Elastic Foundation Modelling

It was mentioned in the previous paragraph how the most common method of analysis for the problem of vibrations applied on a pipeline is the beam on non-linear spring modelling. In the following paragraphs, this type of models is to be explained in further detail.

Several such models have been developed during the past which enable the representation of the given problem with different approaches. Namely, some of these are the Pasternak, Florenko-Borodich, Rhines, Hetenyi, Kerr and finally, the Winkler models. It is worth mentioning how while the main approach remains the same in these models, small modifications have been applied to each one in order for inaccuracies to be minimized in given problems. The florenko-Borodich model for example, consists of Winkler elements, which are in continuous interaction by means of a thin elastic membrane under a constant tensile force T.

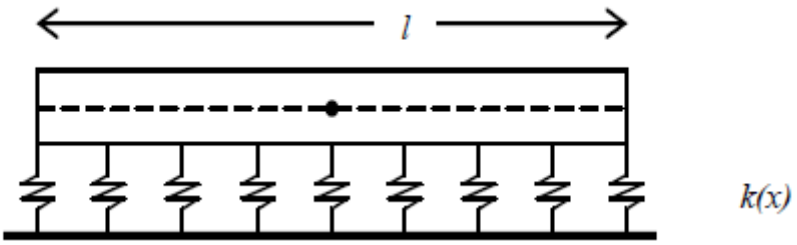

Figure 2.24:Beam on Winkler foundation (Kacar, Tan, & Kaya, 2011)

In remains one of the most fundamental and commonly used methods until today. The proposed model is capable of producing a linear algebraic relationship between a structure's normal displacement and contact pressure. As can be seen in Figure 2.24, the Winkler model considers a beam or a pipeline as an Euler-Bernoulli beam resting on an elastic medium, represented by a set of independent soil springs.

The main advantage of the Winkler model, which makes it used so commonly is its straightforward approach which enables representation of non-linear behaviour without the need of extended computational effort in comparison with the rest of the aforementioned models.

It is worth mentioning at this point how primary consolidation of soil can be very well represented by such a system as the Winkler one due to its static nature. However, in some cases, the need of representation of more complex mechanisms acting upon a structure leads to creation of altered models and the addition of more sophisticated element systems. For example, such a mechanism is soft soil's creep, a time-dependent mechanism which requires several additions and modifications to be introduced to the model in order for accurate representation to be achieved.

2.8 Rheological Models

Viscoelasticity, as the name suggests, is the process in which a material behaves both elastically and viscously. As it is very well described in (Braja M. Das, 2011), ground response can be expressed this way. This is due to the different nature between the soil skeleton and the pore water in the case of a fully saturated material. A main characteristic of this material is how the loading and unloading curves do not coincide and the product resulting is a hysteresis loop. After this action is complete, there may or may not be permanent deformation of the material.

In terms of force (f) and relative displacement (u), it is explained in (Chopra, 1995) how the force-displacement relationship can be linear at small deformations or non-linear at larger ones, and this can be seen in figure 2.25.

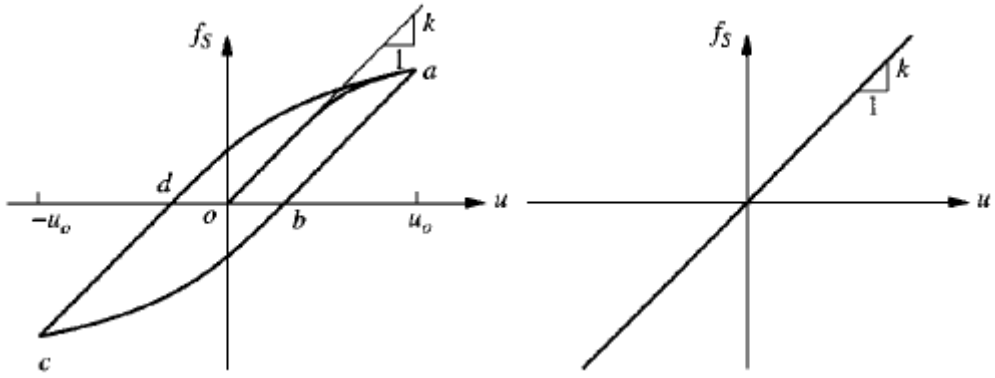

Figure 2.25: Force-Displacement relationship, linear to the right and non-linear to the left (Chopra, 1995)

It can be deducted from what has been mentioned so far how the behaviour of this material is time dependent and hence, the need for a constitutive equation which includes time as a variable in addition to stress and strain is created (Braja M. Das, 2011). Various models have been created for the representation of this behaviour which include spring elements in order to express elastic behaviour and viscous dampers, also known as dashpots, to express viscous. These models are called rheological or mechanical models.

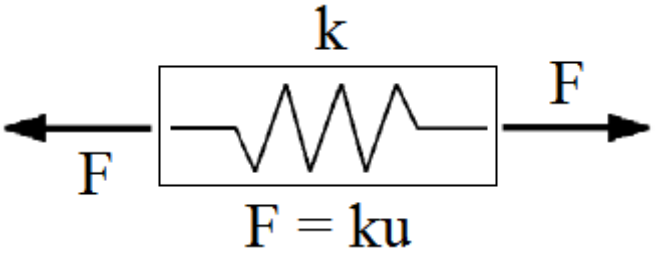

Figure 2.26: The elastic spring

It would be useful at this point for the main elements of these mechanical models to be stated. Furthermore, the first element is the elastic spring. The elastic spring reacts to applied force in accordance with the Hooke's law and is sometimes referred to as Hooke element (Chopra, 1995). This law states how a force (F) needed to displace the spring by some distance (u) is:

$$F = k*u \tag{2.19}$$

Where k is a property of the spring and is characteristic of its stiffness.

Now, it makes sense how the terms of force (f) and displacement (u) can be translated to stress (σ) and strain (ε) respectively when a rigid material is concerned. This is done by the relationships:

$$\sigma = F/A \quad (2.20)$$

$$\varepsilon = \Delta x/x \quad (2.21)$$

Which mean that stress is equal to applied force over the area (A) within which it is applied and strain is the change in dimension (Δx) over the original value (x) of it.

The next element to be discussed is the dashpot one. According to (Chopra, 1995) the process by which a free, or forced, vibration diminishes in amplitude is called damping. Furthermore, it can be understood how in real life applications various different mechanisms take part in this dissipation of energy, some of which may be acting simultaneously. Furthermore, using of dashpot is very common for the experimental representation of real events.

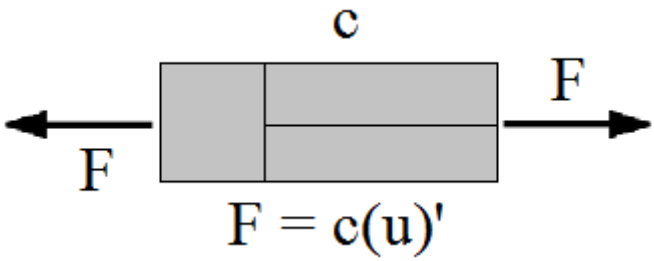

Figure 2.27: The viscous damper

As it is presented in figure 2.27, the relationship between applied force (f) and displacement (u) in this case is:

$$F = c*(u)' \quad (2.22)$$

Where in this equation, the constant c represents the viscous damping coefficient and (u)' the first derivative of displacement, which is velocity. The question which arises now is, how the viscous damper can satisfactorily represent all the complex energy dissipation mechanisms, which as stated before may be acting at the same time. The answer to this by (Chopra, 1995) is that a parameter (c) is selected so that the vibrational energy it dissipates is equivalent to the energy dissipated in all the present damping mechanisms combined. This idealised coefficient of the actual mechanisms is then called equivalent viscous damping.

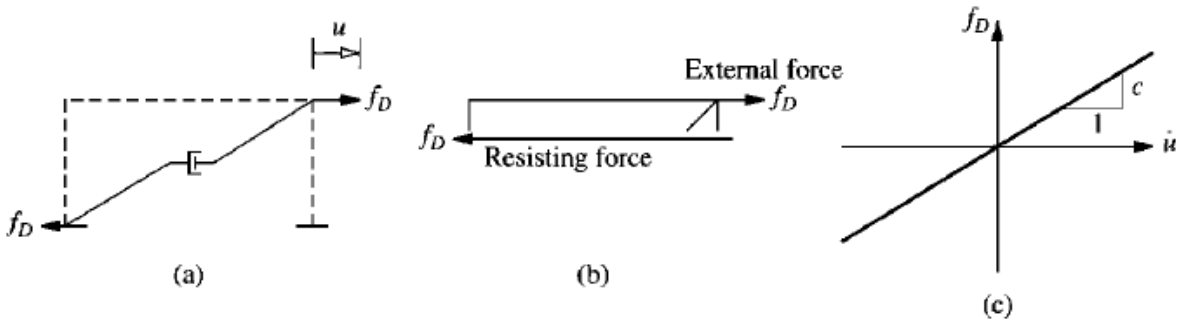

Figure 2.28: Damping response for a free vibration. a) Damper attached to a frame b) Acting forces c) F-u relationship (Chopra, 1995)

It is worth mentioning at this point how for some applications, such as dynamic excitations, it is nearly impossible to theoretically create a damping coefficient that is capable of representing reality. Instead, the most common way is that the coefficient is determined through experimental procedures.

Finally, the spring and dashpot elements can either be connected in series, i.e. one after the other as well as in parallel, i.e. one next to the other. A characteristic example of a system connected in series is the Maxwell model and the Kelvin-Voigt model one for parallel connection. These two are some of the most commonly used systems and will be explained in the section below.

2.8.1 The Maxwell Model

The Maxwell model is composed of a spring and a dashpot connected to each other in series. According to (Jóźwiak, Orczykowska, & Dziubiński, 2015), the total stress in this system is equal to the stress acting on both elements while the total strain is equal to the sum of the corresponding one for each element:

$$\sigma_t = \sigma_s = \sigma_d \quad (2.23)$$

$$\varepsilon_t = \varepsilon_s + \varepsilon_d \quad (2.24)$$

Where for both stress (σ) and strain (ε) from now on the notation (s) will stand for spring and (d) for dashpot.

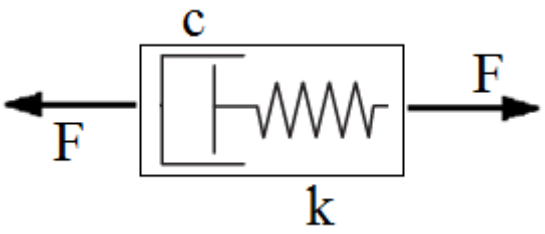

Figure 2.29: The Maxwell model

As (López-Guerra & Solares, 2014) states, the Maxwell model is known to successfully describe stress relaxation, which is the time-dependent drop in stress under a constant strain. However, this model is incapable of describing creep mechanisms, where creep is the process of time-dependent strain relaxation under a constant stress and this can be seen in the figure 2.30. The main disadvantage because of this is how during unloading, the sample experiences elastic recovery which is due to the spring element and proportional to the energy stored in it. However, there is no viscous recovery, as the dashpot has no mechanism to travel back to its original position (López-Guerra & Solares, 2014).

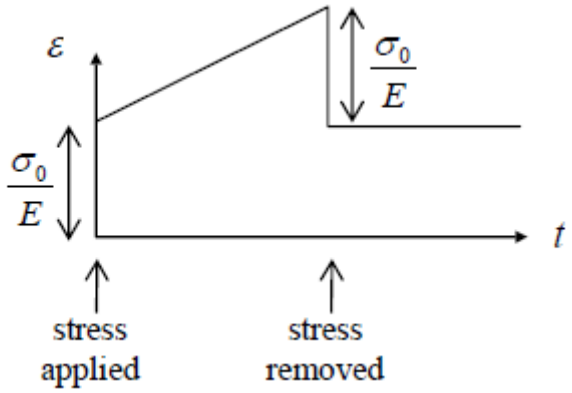

Figure 2.30:Creep recovery response of the Maxwell model (Kelly, 2015)

2.8.2 The Kelvin-Voigt Model

The next model to be discussed is the Kelvin-Voigt one. This model consists of two elements, a spring and a dashpot, connected to each other in parallel. In this case, the total stress of the system is equal to the sum of the two separate stresses acting upon the corresponding elements of the spring and dashpot. As for the strain, it is equal to the strain acting on both elements. This can be expressed as:

$$\varepsilon_t = \varepsilon_s = \varepsilon_d \tag{2.25}$$

$$\sigma_t = \sigma_s + \sigma_d \tag{2.26}$$

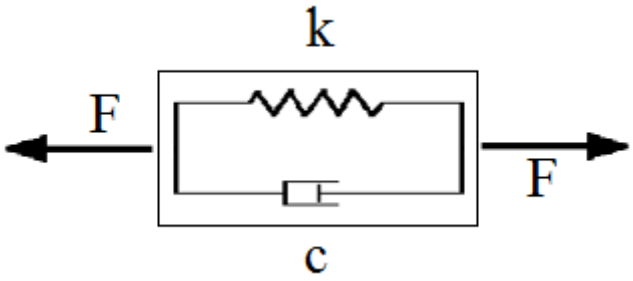

Figure 2.31: The Kelvin-Voigt model

(López-Guerra & Solares, 2014) conclude that this model is able to achieve the opposite of the Maxwell one in terms of performance for creep and stress relaxation. More specifically, it is found that this model is able to describe creep compliance but incapable of describing stress relaxation.

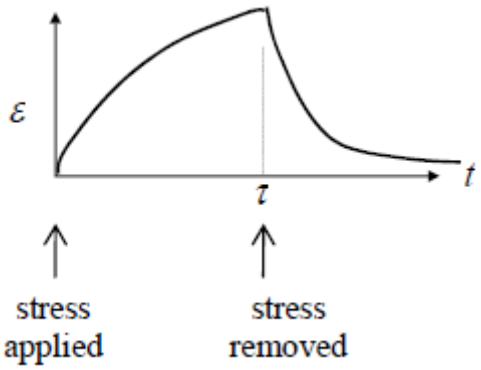

Figure 2.32:Creeo recovery response for the Kelvin-Voigt model (Kelly, 2015)

The two elements are connected in parallel and the system lucks a free spring, that is able to accommodate immediate force applied to it. This is because the only spring in the model experiences compression until the parallel dashpot starts to yield and hence, there is no immediate spring response (López-Guerra & Solares, 2014).

An example of a model with an added independent spring and dashpot is the burger model presented in figure 2.33 as developed at the University of Tehran.

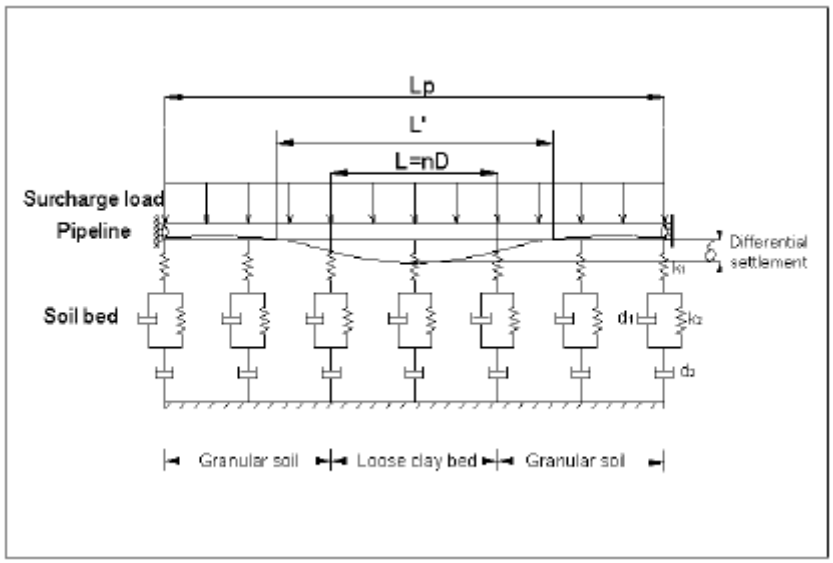

Figure 2.33: Buried pipeline analysed with the Burger model (Faeli & Fakher, 2010)

2.9 P-y Curves

P-y curves are the graphical representations of a buried structure's interaction with the soil, where (p) is the soil resistance and (y) is the relative displacement. In practice, the creation of p-y curves is often carried out by means of the Beam on Non-linear Winkler Foundation method (Dash, Rouholamin, Lombardi, & Bhattacharya, 2017). In this method, lateral interaction between the soil and the buried structure is investigated as a set of non-linear springs.

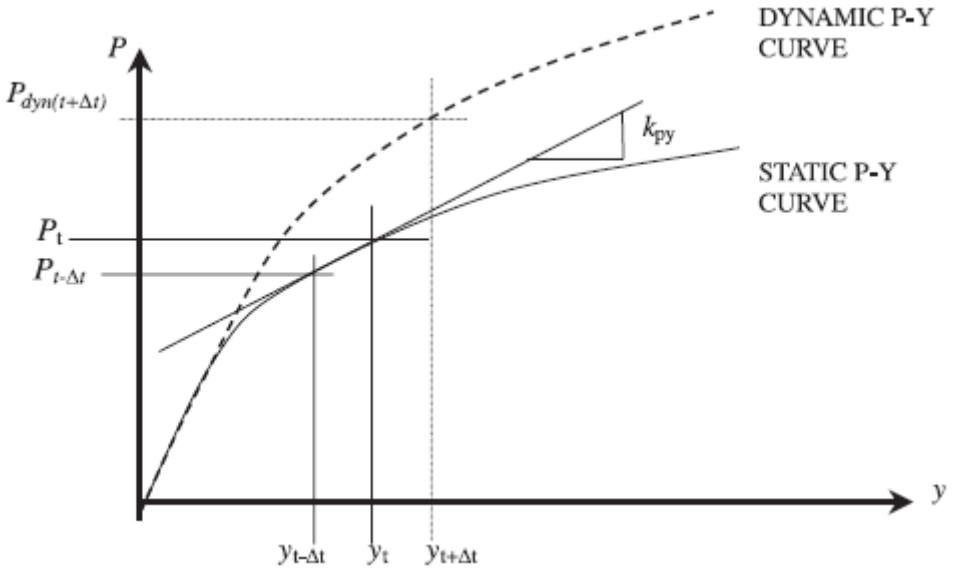

Figure 2.34: Response of Static and Dynamic p-y curves (Naggar & Bentley, 2000)

The shape of a p-y curve might differ for the state of loading. More specifically, (Dash et al., 2017) describe the typical shape of a non-liquefied soil's p-y curve as a convex curve with initial stiff slope which gradually reduces with soil-structure relative displacement, as demonstrated in figure 2.35. (Hededal & Klinkvort, 2010) Explain how these curves were originally created as the non-linear relation between lateral movement (y) and soil response (p) in terms of non-linear monotonic loading by Matock and his co-workers in the 1950^{s}. This was done by back calculation of a series of conducted tests. Later on, in the 1970^{s}, further cyclic tests were carried out by Matock on buried piles. These tests revealed a general trend for the ultimate capacity of the piles to drop compared to the monotonic case.

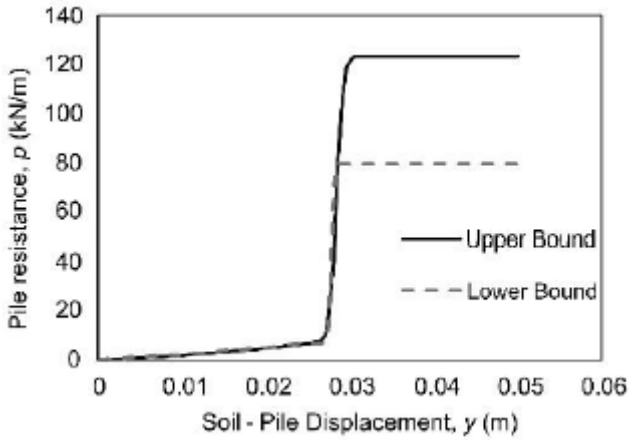

Figure 2.35: P-y curve for liquefied soil (Dash et al., 2017)

These curves have been very commonly used in practice so far. However, as (Dash et al., 2017) very well explains, new studies have proved that the p-y curve for liquefied soil has a different shape than the aforementioned ones. That is an upward concave with near-zero initial stiffness up to a certain displacement, which is created due to the loss of contact between soil particles in liquefied soil. Beyond this point, the stiffness increases as a result of the soil particles' rearranging as shown in figure 2.35.

2.10 Derivation of k and c

One of the most important aspects of this study was the determination of the spring and dashpot coefficients. Furthermore, these two coefficients are vital for the investigation of such a model, as they are playing a major role in achieving a realistic representation of the system's response. More specifically, the spring coefficient (k) was specified by usage of the most relevant and up to date studies while the dashpot coefficient (c) had to be adopted from previous studies, as described in the following paragraphs.

2.10.1 Derivation of the Spring Coefficient (k)

The determination of the spring's coefficient, which will also be referred to as modulus of subgrade reaction, was found to be a great challenge within the framework of this project. Furthermore, in order for the elastic spring coefficient to be determined in a realistic manner, the construction of a p-y curve for liquefied soil was needed.

Furthermore, it was mentioned how in the case of liquefied soil the shape of the p-y curve is an upward concave. This starts with a near to zero initial stiffness, up until it reaches a certain displacement. This near-zero tendency of the material can be explained by the loss of contact between soil particles in liquefied soil. Beyond this point, a stiffness increase is observed as soil particles begin to re-arrange and create the re-development of effective stress. The aforementioned shape is shown in figure 2.35 as was developed by (Dash et al., 2017). The method of (Dash et al., 2017) was used in this study as it was found to be one of the most up to date and accurate techniques.

(Dash et al., 2017) divide the process of creation for the p-y curves in four major steps. These include:

1. Evaluation the soil's parameters by usage of the SPT bore log
2. Considerations of the structure's geometry
3. Construction of a simplified liquefied soil stress-strain curve
4. Generation of the p-y curve with respect to the stress-strain one mentioned in step 3.

More specifically, the variation of SPT value (N) is the first thing which needs to be considered. In this case, this was done by representation of an SPT test presented by (Dash et al., 2017) and as can be seen in figure 2.36. It is worth mentioning how for the liquefiable layer, an average relative density of 40% was kept with values of 30-40% in the top layer, such as the ones in (Horsten, 2016).

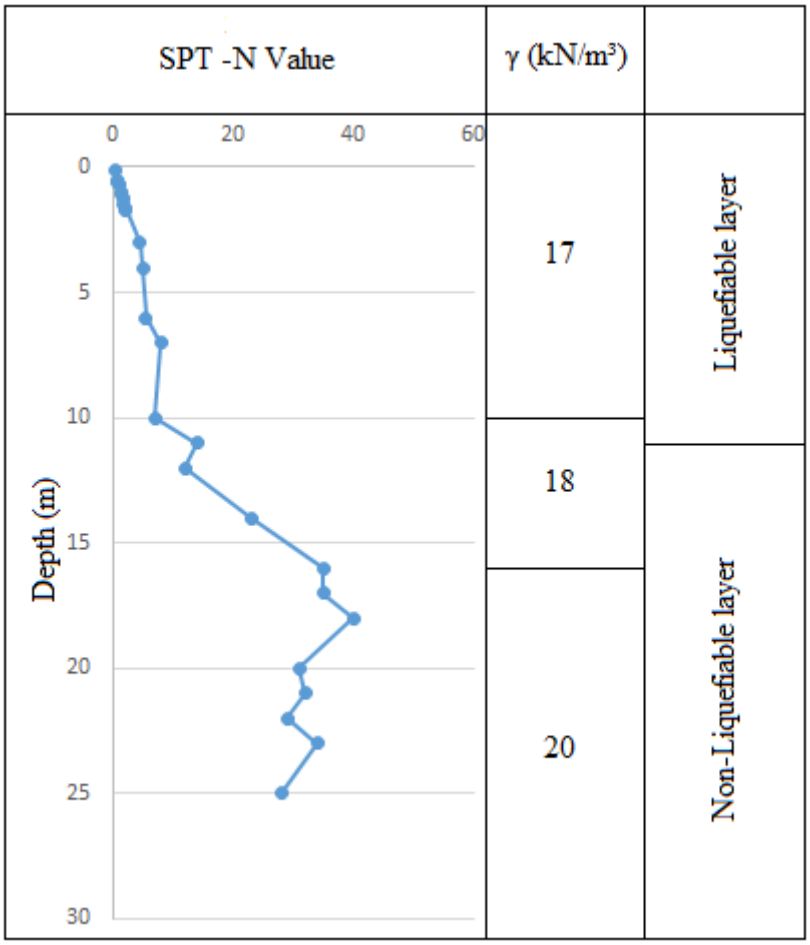

Figure 2.36: SPT blow-count used

Several soil parameters have to be derived from the blow count value (N). These are corrected SPT value (N_1), the relative density (D_r) the critical state stress ratio (M_c) and the residual strength of liquefied soil (M_c). These parameters can be estimated by laboratory testing as well as standard correlations used in literature. Taking into consideration the absence of laboratory testing in this case, the theoretical correlations, which were gathered from various literature pieces by (Dash et al., 2017) were considered.

It is worth mentioning at this point how great importance was given at the shallower depth of the SPT presented above as the burial depth of the pipeline considered was at the range of 0.5m-2m.

More specifically, the first value derived was the corrected for overburden pressure SPT value (N_1). For sandy soils, this is possible with application of the formula:

$$N_1 = (N/SQRT(p'_{ini}/98) \quad (2.27)$$

With p_{ini} being the initial effective overburden pressure. The next parameter mentioned was the soil's relative density D_r. This parameter was considered as a function of the aforementioned N_1 as:

$$D_r = SQRT(N_1/C_D) \quad (2.28)$$

Where $C_D = (9/(e_{max} - e_{min}))^{1.7}$ and at the absence of specified void ratios can be taken as 20 for sands with fines, 70 for gravelly sand and in this case, as 41 for clean sands. Moving on to the critical state stress ratio (M_c):

$$M_c = [(6\sin\phi_{cs})/(3-\sin\phi_{cs})] \quad (2.29)$$

In this case, ϕ_{cs} is the soil's critical state angle and when this is not available from laboratory results, the correlation $\phi_{cs} = 28^o + 15D_r$ can be used.

What can be defined as residual shear strength (s_u) of liquefied soil is the mobilized shear strength at large deformations after liquefaction has occurred. The upper and lower bound values can be used for the worst case scenario of lateral soil-structure interaction to be described. These values are presented in figure 2.37 and it is worth mentioning that the upper bound ones were used within the limits of this study.

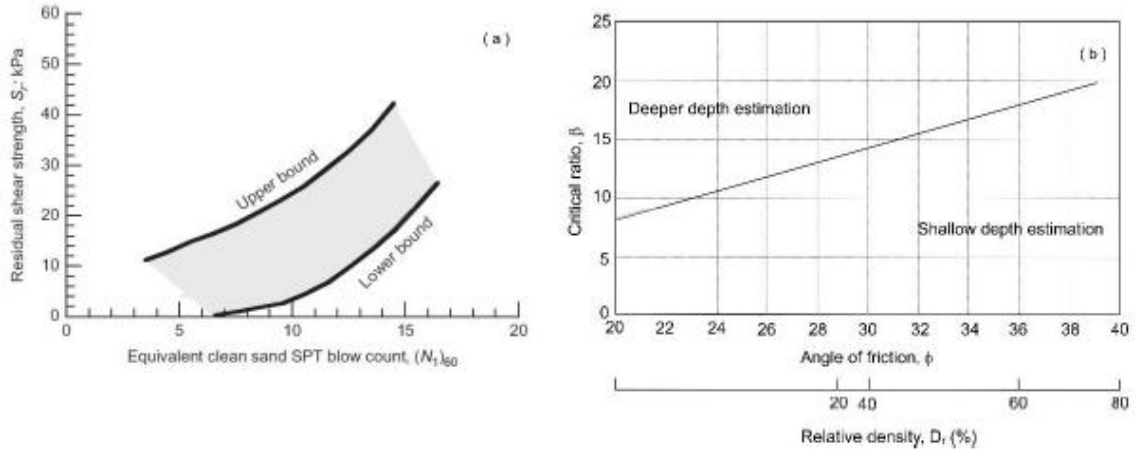

Figure 2.37: To the left (a) upper and lower residual shear strength of soil and to the right (b) critical depth ratio for various relative density/angle of friction (Dash et al., 2017)

Figure 2.37 also demonstrates a parameter which has not been mentioned so far. This is the critical ratio (β) which has been adapted from the 2010 API methods of practice. Furthermore, this parameter takes into consideration the structure's depth and diameter ratio in order for a boundary value, which distinguishes between shallow and deep depth to be created. More specifically, for a specified point at a depth (h) and for a structure's diameter (D), if the ratio h/D is greater than (β), then deep depth applies and vice versa.

Proceeding to the construction of the liquefied soil's simplified stress-strain curve, four main parameters were used. These were the take-off strain (y_{to}), initial shear modulus (G_1), critical state shear modulus (G_2) and the ultimate shear strength τ_{max}. The relationships used for the investigation of these parameters as well as a shape example for such a simplified stress strain relationship are presented in figure 2.38.

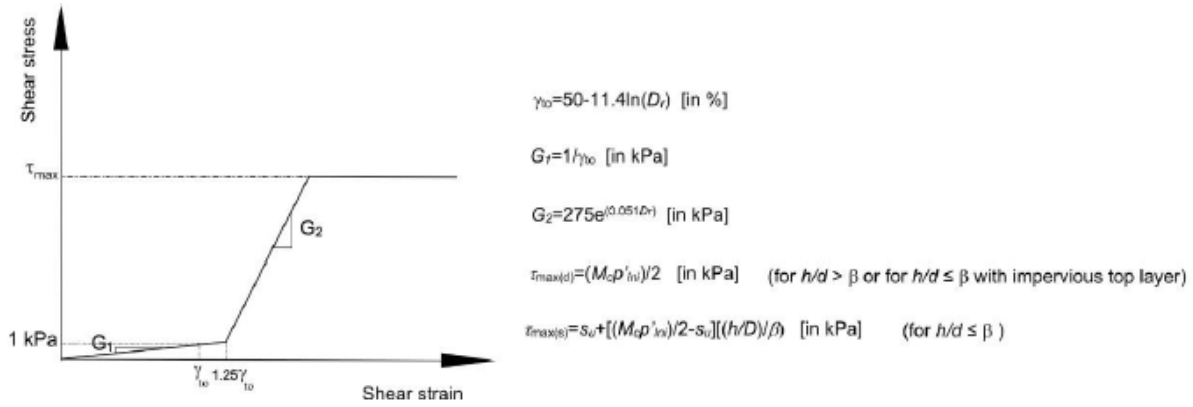

Figure 2.38: Post liquefaction stress strain relationships for liquefied soil (Dash et al., 2017)

It is worth mentioning at this point how $\tau_{max(d)}$ is correspondent of the minimum and non-negative pore water pressure in post liquefaction shearing and $\tau_{max(s)}$ is the soil's residual strength at shallow depths. In addition to this, (Dash et al., 2017) explains that the relationships of (G_2) and (y_{to}) were formulated by extensive element testing by a great lot of researchers. It is also explained how in the absence of experimental testing, these empirical relationships are safe to be used for the determination of stress-strain parameters. Finally, it is worth noting that the aforementioned relationships are based on soil relative densities ranging 20-80% and may not be extrapolated beyond or above these ranges.

Once the simplified stress-strain relationship has been established, scaling is used for the creation of the corresponding p-y curve. Furthermore, these scaling factors are M_s and N_s and figure 2.39 shows a schematic representation of this process.

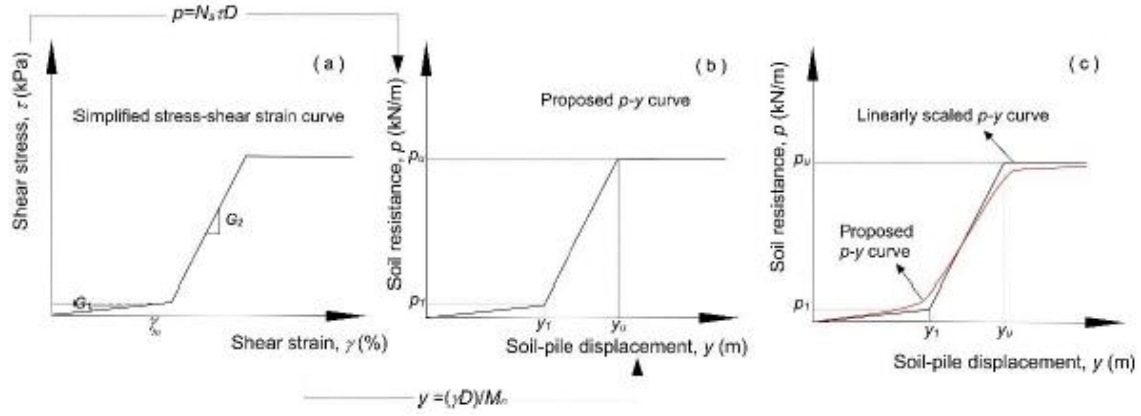

Figure 2.39: The process of obtaining liquefied soil's p-y curves from stress-strain relationships. (a) Simplified stress-strain curve for liquefied soil, (b) linearly scaled p-y curve model for stress-strain model, and (c) smoothed p-y curve model.(Dash et al., 2017)

2.10.2 Derivation of the Dashpot Parameter (c)

It was described, earlier on, in this chapter how it is most common for the coefficients of viscous dampers to be specified by means of physical modelling. It was then explained how all the complex energy dissipation mechanisms acting upon the system are nearly impossible to be satisfactorily expressed in a theoretical manner. It was also explained how a single value can be derived, which describes all those dissipation mechanisms combined. This was called equivalent damping.

In this case, (Horsten, 2016) investigated the phenomenon of pipe uplift in liquefied soil by means of physical modelling. Furthermore, several parameters were determined within this study, among which was a dashpot coefficient which was capable of adequately representing uplift behaviour. Three ways were used for this problem to be approached. These were a combination of physical modelling, a quasi-static analysis and Abaqus modelling.

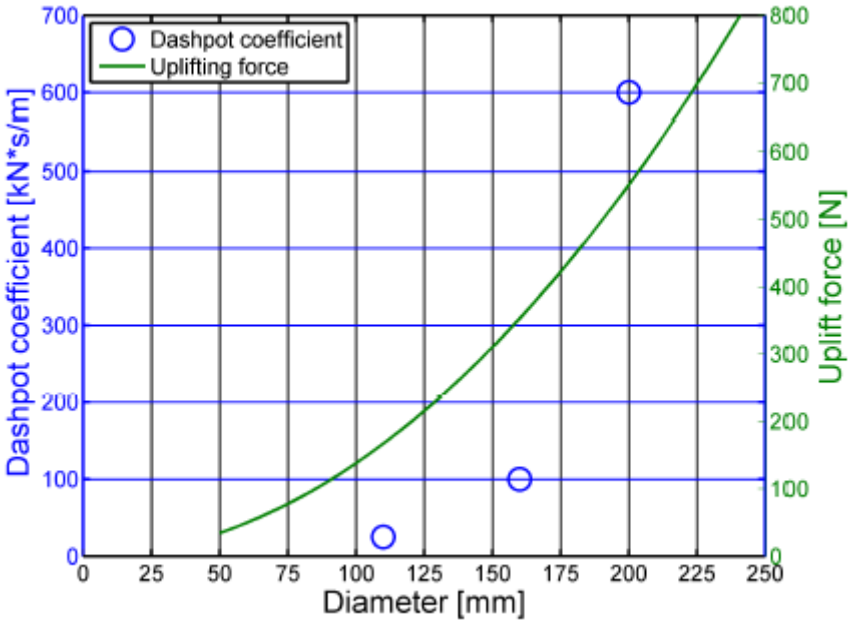

Figure 2.40: Pipe diameter-viscous damper coefficient relationship (Horsten, 2016)

Figure 2.40 describes how this study concluded in realistic dashpot coefficients related to pipe diameter and uplift force. Furthermore, a linear fit was applied with direct relation between the diameter of the pipe used and the coefficient. More specifically, it was concluded that:

Table 2.1: Dashpot Coefficients

Pipe Diameter (mm)	**Dashpot Coefficient** (kN*s/m)
110	25
160	100
200	600

Finally, these values were used for the computer modelling investigation, which was conducted within this study.

2.11 Maximum Uplift and Prevention

(O'Rourke & Liu, 2012) very well explain in their book how the content of a pipeline may affect its uplift potential. Furthermore, pipelines carrying liquids are not as likely as gas filled ones to experience uplift due to post-liquefaction effects because of their larger weight. However, the ones containing lighter materials, such as gas, are more susceptible to this phenomenon and thus, several commonly carried elements will be tested in this report.

A theoretical manner of analysis is suggested in the same report which states that the uplifting force per unit length can be calculated as:

$$P_{uplift} = (\pi D^2/4) *(\gamma_{soil} - \gamma_{contents}) - \pi D\gamma_{pipe} \quad (2.30)$$

Where (P_{uplift}) is the uplifting force, D the pipe's diameter and γ_{soil}, $\gamma_{contents}$ and γ_{pipe} the unit weights of the soil, pipe's contents and pipe's material respectively.

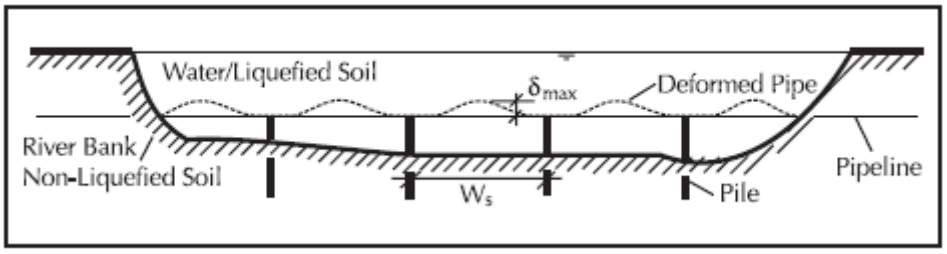

Figure 2.41: Pipe in liquefied zone (O'Rourke & Liu, 2012)

In addition to this, (O'Rourke & Liu, 2012) also suggest an equation capable of theoretically determining the expected maximum uplift displacement (δ_{max}) and/or the spacing of restrains, such as piles, where large uplift is essential to be prevented. This equation is:

$$A\delta_{max}^3 + 16*I*\delta_{max} - (16P_{uplift}W_s^4)/(E\pi^5) \quad (2.31)$$

Where, as shown in figure 2.41 A is the pipe's cross sectional area, W_s the pile's spacing, I the second moment of inertia and E the Young's Modulus.

Finally, the peak pipe strain can also be calculated from:

$$\varepsilon_{max} = \pm(\pi^2\delta_{max}D)/W_s^2 + (\pi^2\delta_{max}^2)/4W_s^2 \quad (2.32)$$

3 Conceptual Model

As has already been mentioned, the scope of this study is the investigation of buried pipelines' soil-structure interaction in liquefied soil by means of modern, computer simulation techniques. Furthermore, the approach adopted was a spring and dashpot modelling technique, which was used for the development of a single degree of freedom model. The term "degrees of freedom" is very well described by (Chopra, 1995) as the number of independent displacements required in order to express the displaced positions of all the masses relative to their original position.

3.1 Single Degree of Freedom

The first model created was a system that included a mass, and a Kelvin-Voigt element attached to its bottom side as shown in figure 3.1. It is worth mentioning at this point how the mass of this system was representative of the pipeline, filled with several different elements as will be discussed in the results' section. It can be seen from the formation of this system that the pipeline has only one degree of freedom, which is its displacement on the vertical axis during excitation.

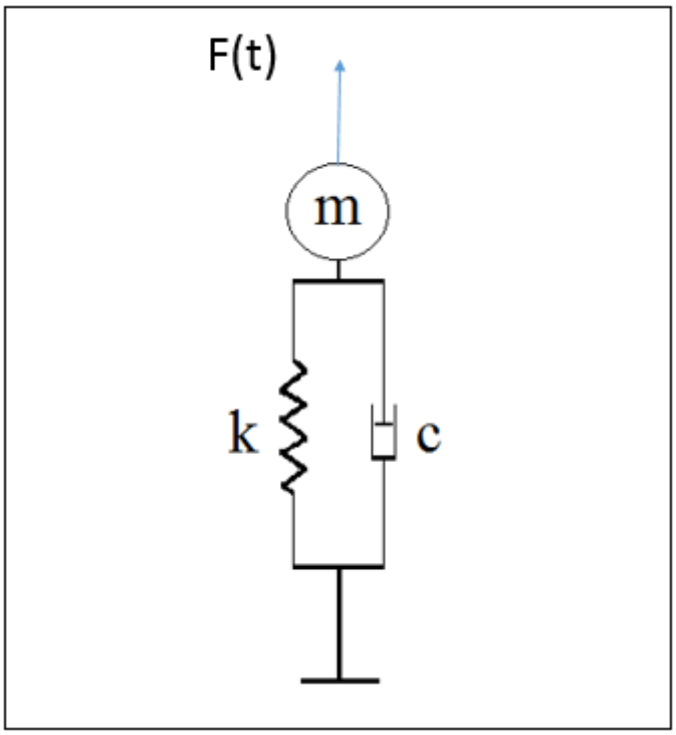

Figure 3.1: Single Degree of Freedom model used

Several things were required in order for this model to be expanded into an algorithm capable of representing a given parameter problem accurately. Furthermore, the most essential part was the formation of a constitutive equation for a pipeline allowed to move freely. This became possible by combination of the rheological models explained so far along with their characterising equations. More specifically, for the system described in figure 3.1, that equation was found to be:

$$F(t) = m(u)'' + c(u)' + ku \qquad (3.1)$$

Where (m) is mass, (u) is displacement and (c) and (k) the dashpot and spring coefficients respectively.

Dividing this by m, gives:

$$(u)'' = F(t)/m - c(u)'/m - ku$$

Which forms a differential equation that is solvable by the ODE45 solver in matlab. As for the uplift force, it was considered to be a wave in the form of F(t) = F0*sin(ωt) and in an appropriate number of cycles for each case considered upon which maximum uplift has occurred.

However, much more research was needed in order for k and c parameters, capable of representing soil-structure interaction during the complex phenomenon of post-liquefaction.

3.2 Multi Degree of Freedom

As for the next model, it was a multi degree of freedom one. More specifically, this system consisted of two degrees of freedom, horizontal and vertical displacement. As can be seen in figure 3.2, this model consisted of two Kelvin-Voigt elements at the bottom and right hand side of the pipeline mass.

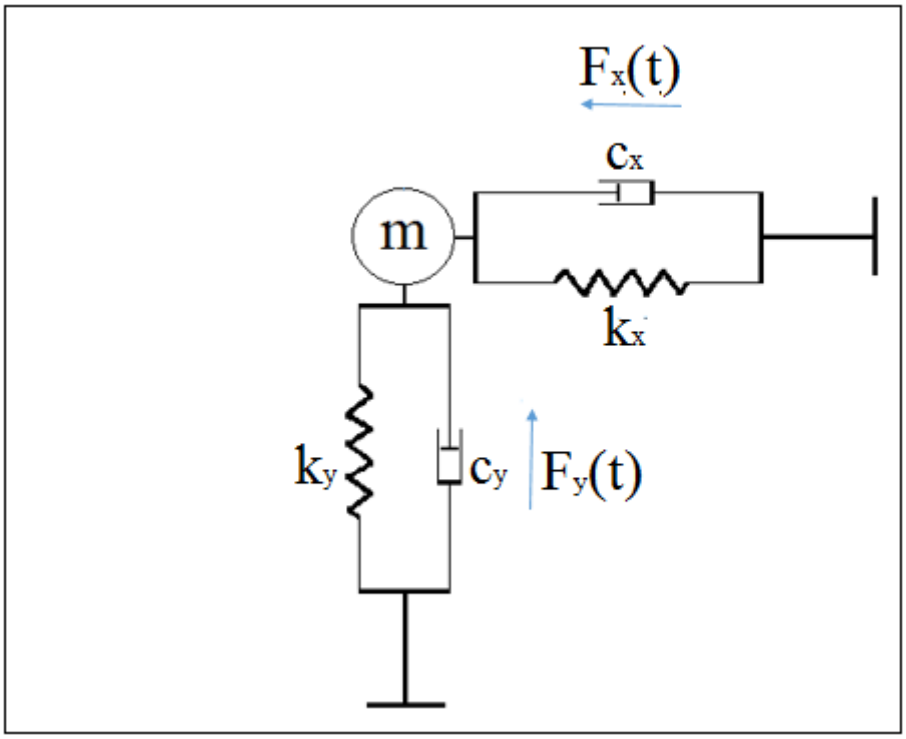

Figure 3.2: Multi Degree of Freedom Model

Once again, a constitutive equation had to be formed for the two degree of freedom model. This was proved to be a more challenging task in the case of the multi degree of freedom case due to the fact that the model parameters were now referred upon two different axes. Furthermore, a suitable solution was required, which would be able to correlate the x and y axes local coordinates with the respective global ones, which describe the combined force and displacement acting upon the investigated mass.

Likewise with the first model, a force relevant relationship was found suitable. More specifically, the two acting forces act on the same model point, the pipeline mass, and lay on the x and y axes respectively. Hence, a right angle between the two force vectors is present and vector addition becomes possible in accordance with the Pythagorean Theorem as:

$$R = \sqrt{Fx^2 + Fy^2} \tag{3.2}$$

Where (F_x) and (F_y) are the forces acting on the horizontal and vertical planes respectively and (R), which is also going to be refed to as F, is their resulting force as can be seen in part (a) of figure 3.3.

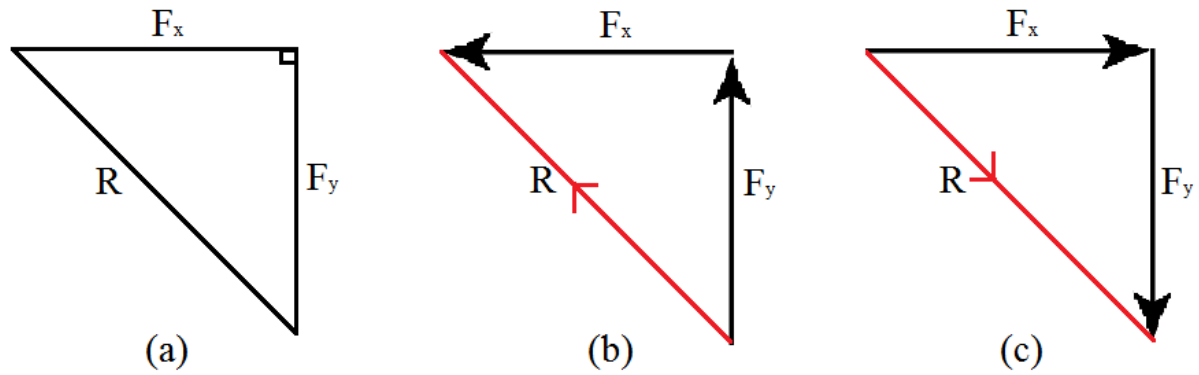

Figure 3.3: Local to global force relationship

Breaking all of these factors down, the following are valid:

$$F(t) = m(u)'' + c(u)' + ku$$

$$F_x(t) = m(u)'' + c_x(u)' + k_xu$$

$$F_y(t) = m(u)'' + c_y(u)' + k_yu$$

It is worth mentioning at this point how the direction of F_x and F_y was expected to change from positive to negative and vice versa as can be seen in parts (b) and (c) of figure 3.3. Naturally, this would also cause their resulting force's direction to change accordingly. However, on contrary to direction, the magnitude of all acting vectors would not be affected.

The combination of what has been mentioned so far leads to the formation of:

$$m(u)'' + c(u)' + ku = \sqrt{Fx(t)^2 + Fy(t)^2} \tag{3.3}$$

Which can be reformed to a solvable nonlinear second order differential equation as:

$$(u)'' = (\sqrt{Fx(t)^2 + Fy(t)^2} - c(u)' - ku)/m \tag{3.4}$$

In order for the force directions to be taken into consideration each time, the magnitude of the squared forces was considered with either positive or negative orientation and complex number solutions were obtained from the ODE45 solvable reformation:

$$(u)'' = (\sqrt{Fx(t) * |Fx(t)| + Fy(t) * |Fy(t)|} - c(u)' - ku)/m \tag{3.5}$$

3.3 Derivation of the Spring Coefficient (k) and Dashpot Coefficient (c)

As for the derivation of the spring coefficient (k), the method followed was the one proposed by (Dash et al., 2017) and as explained in chapter 2.10.1. (Dash et al., 2017) published a practical method of p-y curve construction for liquefied soils. It is worth mentioning how the proposed method is directly dependent to the given soil profile and has as a starting point the usage of SPT derived ground parameters. Hence, this allowed the usage of multiple SPT data inputs in order for the effect that ground parameters, such as stiffness, have on the results to be determined.

The evaluation of soil parameters from bore-log data has already been explained in section 2.10.1 of this report. Furthermore, in this section the way in which the required p-y curves were constructed as well as the way in which the horizontal and lateral spring coefficients were derived is explained. More specifically, the following set of equations is used in order for the ultimate lateral resistance and displacement to be evaluated:

1. The scaling factor N_s is found to be $N_s = 11.94$ for a rough interface and $N_s = 9.2$ for a smooth interface. The latter was found to be valid in terms of this study as it is taking into consideration pipelines made out of steel.
2. M_s, the strain scaling factor is used for the introduction of liquefaction to the p-y curves and is equal to $M_s = 1.87$ for fully liquefied soil.
3. The initial lateral resistance, which corresponds to take off strain is $p_1 = N_s\ 1.25\gamma_{to}G_1D$
4. The initial lateral displacement, which corresponds to take off strain is $y_1 = 1.25\gamma_{to}D/M_s$
5. The ultimate lateral resistance is $p_u = N_s\ \tau_{max}\ D$
6. The ultimate lateral displacement $y_u = [1.25\gamma_{to} + (\tau_{max} - G_1 1.25\gamma_{to})/G_2] * D/M_s$
7. Finally, (Dash et al., 2017) concluded that in order for a p-y curve model to be created, that is capable of a pragmatic post-liquefaction soil behaviour representation and can be used in numerical analysis, one more step has to be carried out. This is how the p-y curve derived in the previous steps has to be smoothened at its transition points by means of weighting factors, which were:

$$p = \omega\frac{p_1}{y_1}y + A(1-\omega)\left[\frac{p_u + p_1}{2} + \frac{p_u - p_1}{2}\tanh\frac{2\pi}{3(y_u - y_1)}\left(y - \frac{y_u + y_1}{2}\right)\right] \tag{3.6}$$

And:

$$\omega = \frac{1}{2}\left[1 - \tanh\left(\frac{6\pi}{y_u}\left(y - \frac{4y_1 + y_u}{6}\right)\right)\right] \tag{3.7}$$

Where a y= 0 corresponds to A = 0 and for any y different than zero, A = 1.

Following this process, the p-y curve presented in figure 3.4 is an example of the ones created with respect to this study.

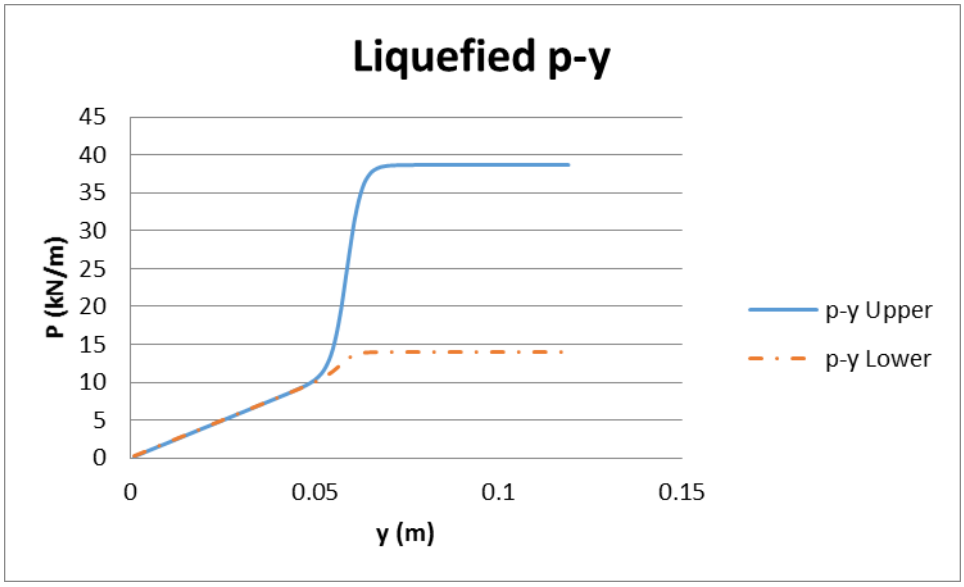

Figure 3.4: Example of liquefied soil's p-y curve produced in this study

After the corresponding p-y curve was created, the modulus of subgrade reaction also had to be determined. Furthermore, according to (Naggar & Bentley, 2000) and NEN3650-1 the horizontal modulus of subgrade reaction (k) can be determined as the tangent value produced by the p-y curves and corresponding to p_u/y. This coefficient is graphically represented in figure 3.5 and represents the transition from elastic to viscous behaviour of the post-liquefied material.

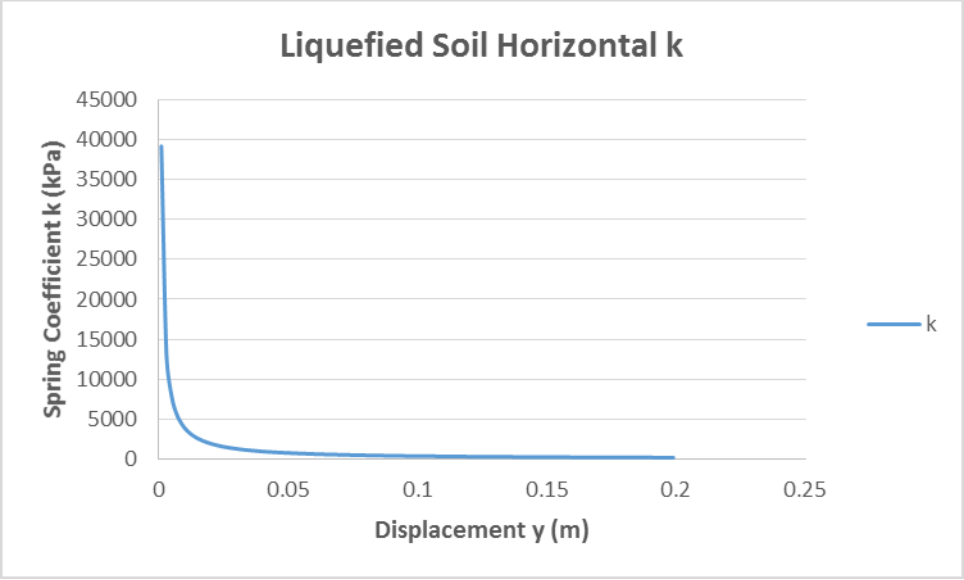

Figure 3.5: Example of calculated horizontal modulus of subgrade reaction (k) for liquefied soil

It is worth mentioning how this plays a major role in the numerical simulation of the liquefied material's behaviour and the corresponding transition between the pipe's uplift and settlement followed.

Finally, the modulus of subgrade reaction presented thus far was valid for the lateral case and had to be re-formed in order for it to be used in vertical situations as well. This was made possible by the comment of (Deltares, 2016) which states that $k_h = 0.7k_{v,bottom}$, where $k_{v,bottom}$ is the vertical modulus of subgrade reaction at the bottom point of the pipeline considered.

It is also worth mentioning at this point how the p-y curves as well as the modulus of subgrade reaction were independently derived for each investigation by means of a fully computer automated manner.

As for the dashpot coefficients, it was explained in section 2.10.2 how the values derived by (Horsten, 2016) were used as:

Table 3.1: Dashpot coefficients used

Pipe Diameter (mm)	**Dashpot Coefficient** (kN*s/m)
110	25
160	100
200	600

These coefficients resulted by usage, in a series of physical modelling experiment, and are dependent to the following ground and geometry conditions. These conditions were also taken into account for the investigations presented in this paper.

Table 3.2: Input and output parameters of laboratory experiments

Experiment	**Length** (mm)	**Diameter** (mm)	**Thickness** (mm)	**Cover** (mm)	**Relative Density** (%)	**Uplift Force** (kN/m)	**Uplift Displacement** (mm)
1	3000	110	3.05	300	20-40	154	225
2	3000	160	4.78	400	20-40	355	130
3	3000	200	6.35	500	20-40	558	70

Finally, it is worth mentioning at this point how the total uplift of the pipe was measured for a unit allowed to move freely.

3.4 Derivation of Parameters

The derivation of several input parameters has been explained so far. More specifically, the problem geometry has been described, as well as the dashpot coefficients used. In addition to these, the process by which the spring coefficient was derived each time has been explained. However, there are yet several parameters which were considered and in the following paragraphs, the derivation of these is going to be explained.

First of all, the weights used for the different pipelines, they were considered with respect to the available market catalogue by the producer company "Tioga" as:

Table 3.3: Pipeline input weights

Diameter (mm)	**Weight** (kg/m)
110	8.37
160	19.3
200	33.3

The aforementioned pipelines were considered for both the single and multi-degree of freedom models to be filled with several different materials which are most commonly transported by pipeline infrastructure. The weight of those materials could be calculated and added to the weight of the pipelines themselves by the corresponding material relative density and the already available occupied space by them. The relative densities used in each case were:

Table 3.4: Materials' relative densities

Material	Air	Gas	Oil	Water	Sludge
Density (kg/m^3)	1.2	0	900	1000	1600

It would be worth mentioning at this point how a full liquefaction state is considered already at the beginning of the analyses and hence, the liquefaction time is not taken into consideration.

Next, it was mentioned in clause 2.6.2 how several factors are critical to the extent that uplift due to liquefaction is likely to occur such as pipe diameter, burial depth and soil stiffness. These factors, along with various others, are going to be investigated in the following sections. However, it would be beneficial for some of the parameters used in these varied parameter investigations to be explained at this point of the report. First of all, the initial pipe diameters, weights and burial depths have already been determined. However, here are some of the varied ground parameters used and derived by the aforementioned methods with the help of SPTs created to represent the given ground conditions:

Table 3.5: Derived Input parameters of initial investigation conditions

Diameter (mm)	**Depth** (m)	**SPT Blow-count N**	**Critical Ratio β**	**Upper Residual Strength S_u** (kPa)
110	0.41	0.7	14	10
160	0.56	0.9	14	12
200	0.7	1.1	14	15

Next, several analyses were conducted in order for the effect of burial depth to be investigated. Furthermore, in each case, the pipeline was resting at a depth of 1.7m, which means that the cover was in all cases approximately 1.5m.

Table 3.6: Derived input parameters of pipeline bottom at 1.7m.

Diameter (mm)	**Depth** (m)	**SPT Blow-count N**	**Critical Ratio β**	**Upper Residual Strength S_u** (kPa)
110	1.7	4	17	30
160	1.7	4	17	30
200	1.7	4	17	30

Following, in terms of ground conditions, an input set of parameters was derived in such a way, that is would be capable of representing a stiffer ground domain than before, for a cover depth again of approximately 1.5m.

Table 3.7: Derived input parameters of pipeline for stiffer ground conditions with bottom at 1.7m.

Diameter (mm)	**Depth** (m)	**SPT Blow-count N**	**Critical Ratio β**	**Upper Residual Strength S_u** (kPa)
110	1.7	5	18	42
160	1.7	5	18	42
200	1.7	5	18	42

Finally, it was considered beneficial at this point for an overview of the parameters used by (Horsten, 2016) to be included for them to be compared to the ones listed above and used within the framework of this study and hence, a parameter validation to be made.

Table 3.8: Overview of pipe uplift experiment parameters as used in (Horsten, 2016)

number	length [m]	diameter [mm]	thickness [mm]	E-modulus [Mpa]	Coverage [mm]	Relative density [%]	Uplift force [N/m]
1	3000	110	110/17	1100	300	20-40	154
2	3000	160	160/33	1100	400	20-40	355
3	3000	200	200/33	1100	500	20-40	558

4 Results and Discussion

4.1 Method Validation

First of all, the topic of this research is a trending topic of geotechnical engineering for which, limited research material is available and even less results have been published so far. Furthermore, it was found appropriate that the validation of the method used in this study is done by results produced experimentally on this subject by (Horsten, 2016). Furthermore, in this section, the relevant results are presented. Finally, it has to be noted that the total uplift at the 3m point were considered as far as the results derived from this study are concerned.

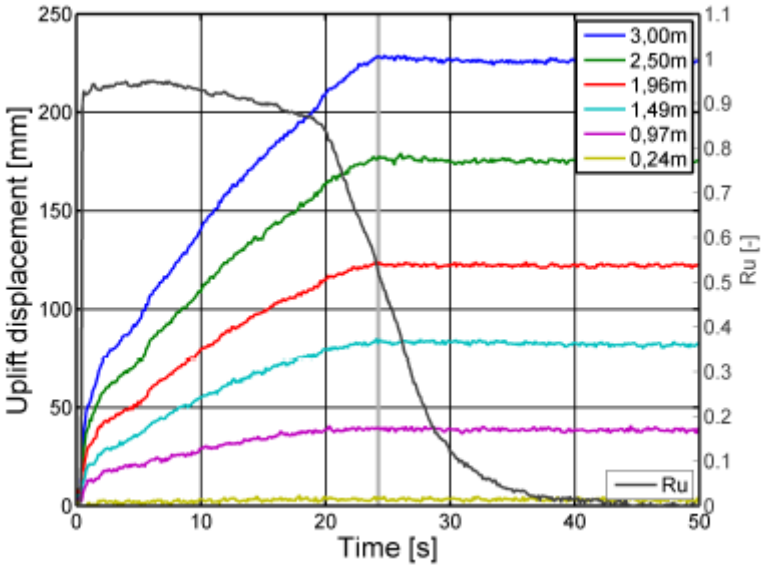

Figure 4.1: Uplift displacement for the 110mm pipeline as presented in (Horsten, 2016)

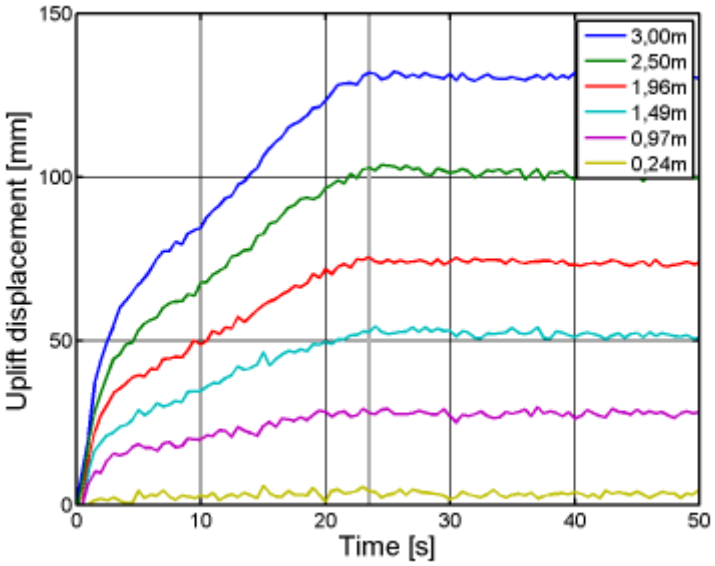

Figure 4.2: Uplift displacement for the 160mm pipeline as presented in (Horsten, 2016)

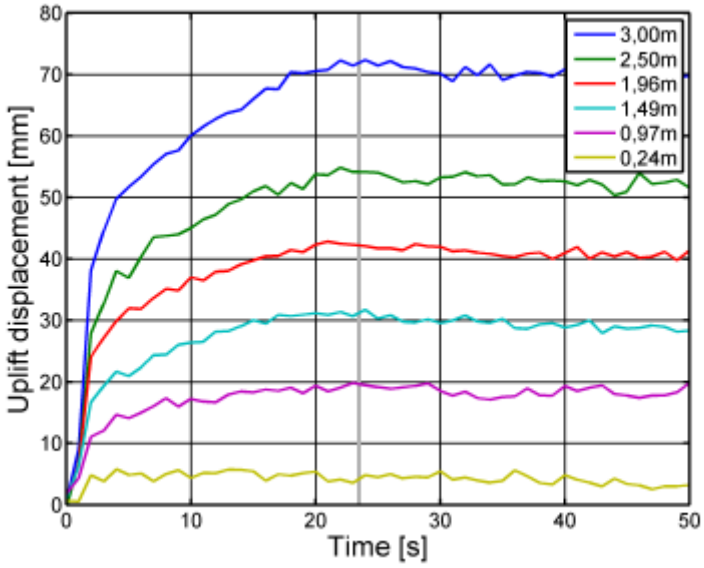

Figure 4.3: Uplift displacement for the 200mm pipeline as presented in (Horsten, 2016)

In addition to the results presented by (Horsten, 2016), validation of what is going to be presented in the following paragraphs can be done by once again recalling the centrifuge experiments conducted by (B. Huang et al., 2014) which were mentioned in the literature review of this report. Furthermore, in this study, aluminium pipes, reportedly meant to transport oil and gas, were tested with a relative density of 2.7g/cm³, a length of 390mm and inner and outer diameters of 36 and 40mm respectively.

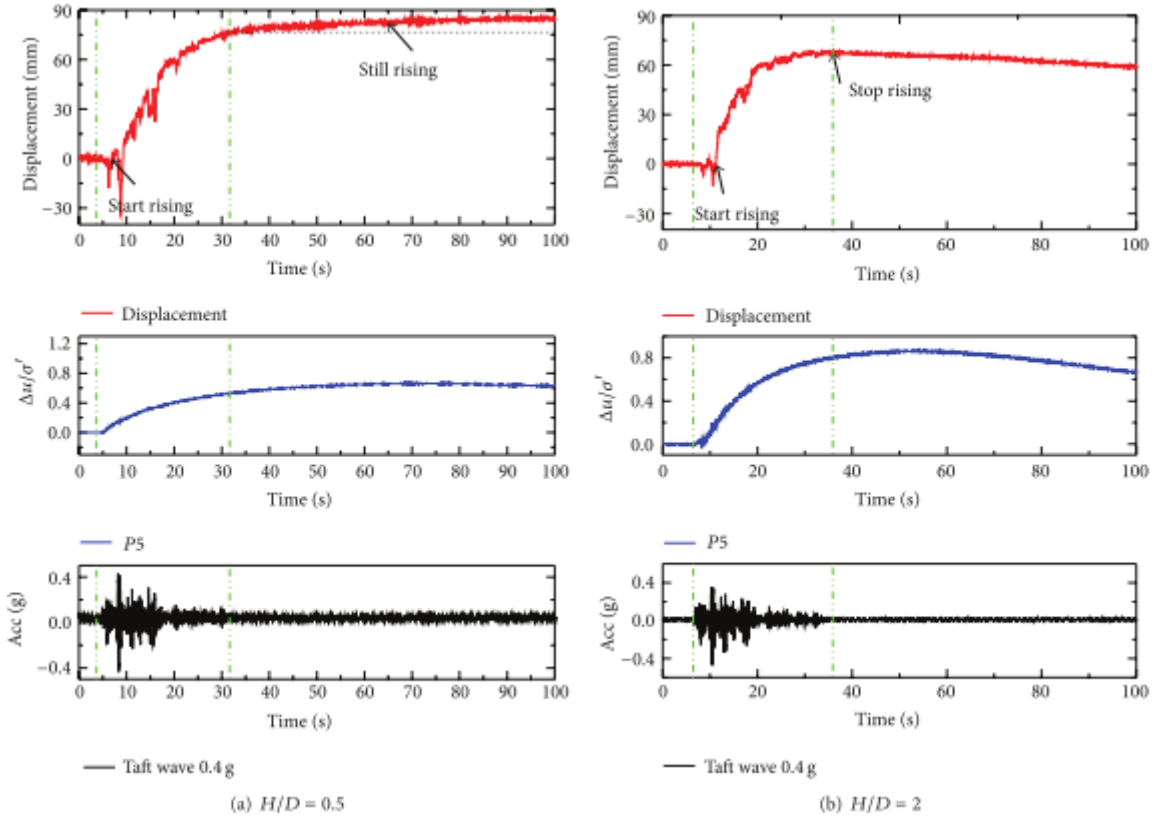

Figure 4.4: Centrifuge pipe uplift results presented by (B. Huang et al., 2014)

4.2 Single Degree of Freedom

The main interest of this chapter is the results produced by the first, single degree of freedom, model. Furthermore, analyses were run for the aforementioned input geometries and parameters in order for the influence of weight, diameter, burial depth and soil stiffness upon pipe uplift to be investigated.

4.2.1 Initial Parameter Single Degree of Freedom and Validation

The first investigation, which was carried out, was the one that had as input parameters a selection of data identical to the one used in the physical modelling experiments of (Horsten, 2016), as were presented in the tables of part 3.4.

As can be seen in figures bellow, the maximum observed uplift displacement in each case was:

Table 4.1: Single degree of freedom uplift of gas filled pipeline

Diameter (mm)	110	160	200
Maximum Uplift (mm)	138	130	76

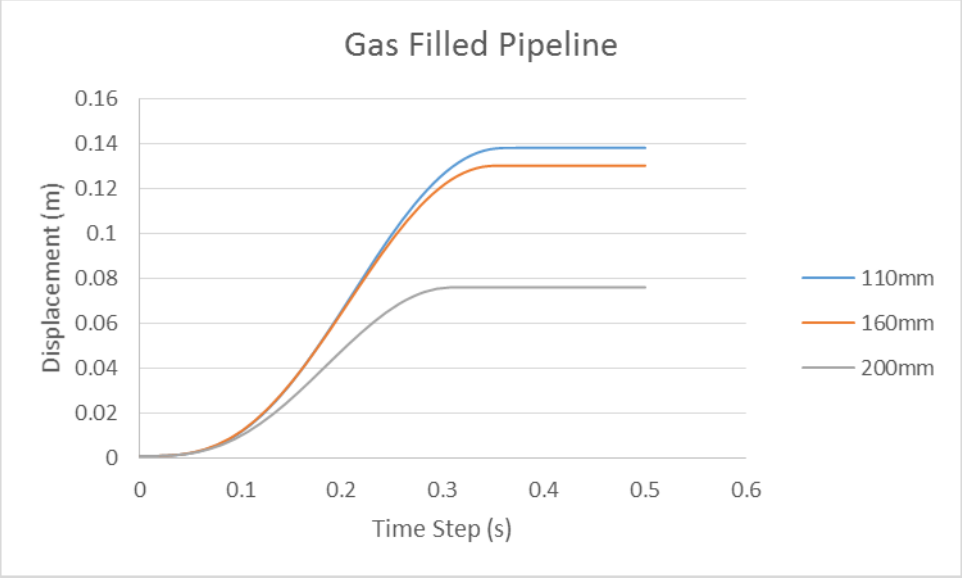

Figure 4.5: Uplift of gas filled pipelines

Table 4.2: Single degree of freedom uplift of air filled pipelines

Diameter (mm)	110	160	200
Maximum Uplift (mm)	138	130	76

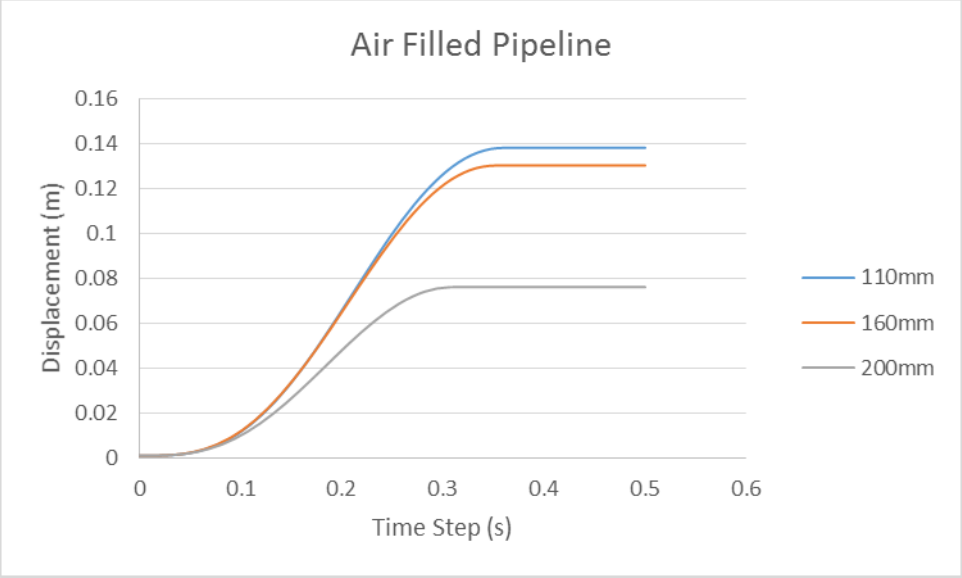

Figure 4.6: Uplift of air filled pipelines

Although the uplift values are comparable to the ones presented by (Horsten, 2016) for the cases of the 160mm and 200mm pipelines, the 110mm diameter ones do not follow the trend. This was observed in all analyses held and it was concluded that the dashpot coefficient in the 110mm diameter case was not accurate. Furthermore, these pipelines were left outside the scope of this study and investigation continued for the remaining two.

.As for oil filled pipelines, maximum uplift was:

Table 4.3: Single degree of freedom uplift of oil filled pipelines

Diameter (mm)	160	200
Maximum Uplift (mm)	80	56

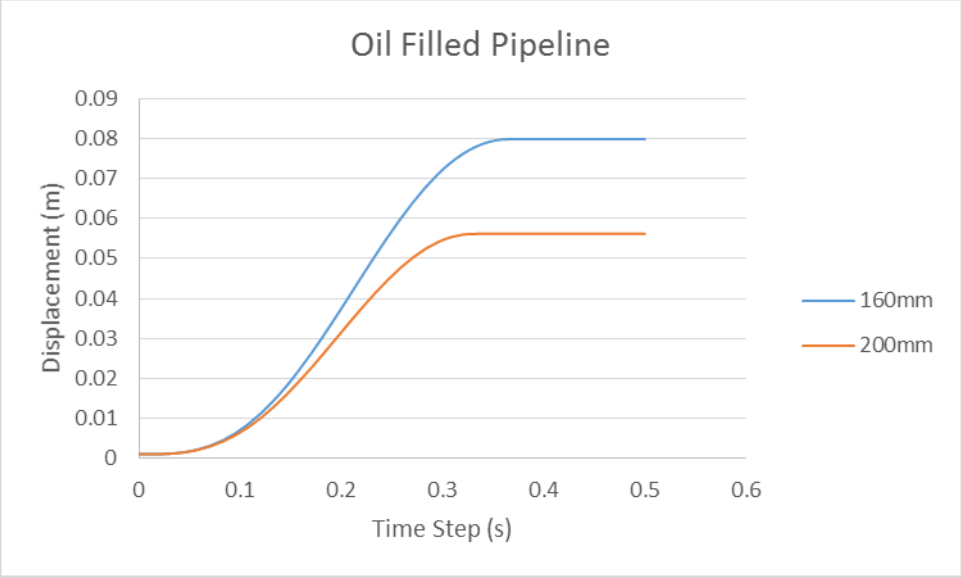

Figure 4.7: Uplift of oil filled pipeline

Next, pipelines carrying water were tested and their maximum uplift was found to be:

Table 4.4: Single degree of freedom uplift of water filled pipelines

Diameter (mm)	160	200
Maximum Uplift (mm)	76	54

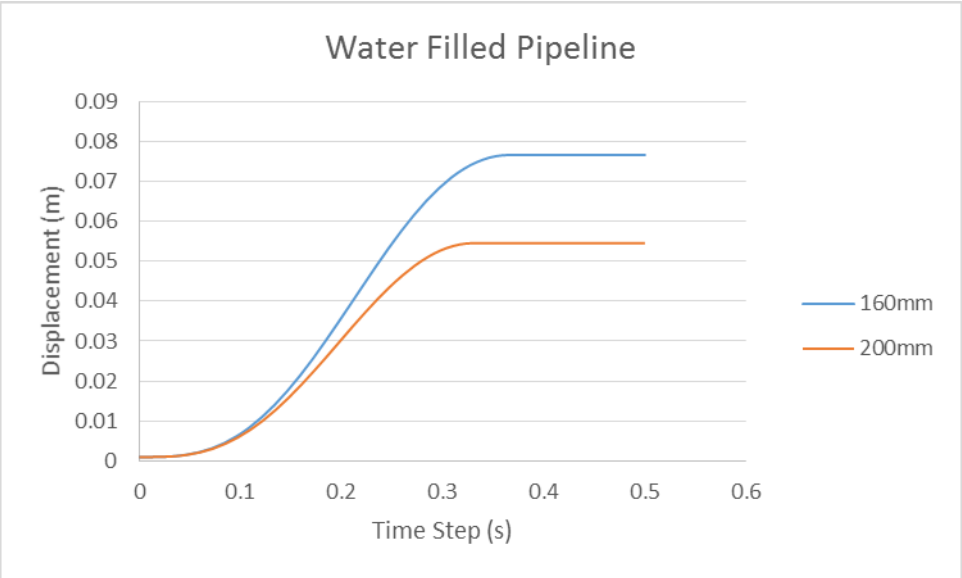

Figure 4.8: Uplift of water filled pipeline

Finally, maximum uplift of sludge filled pipelines was found to be:

Table 4.5: Single degree of freedom uplift of sludge filled pipelines

Diameter (mm)	160	200
Maximum Uplift (mm)	62	47

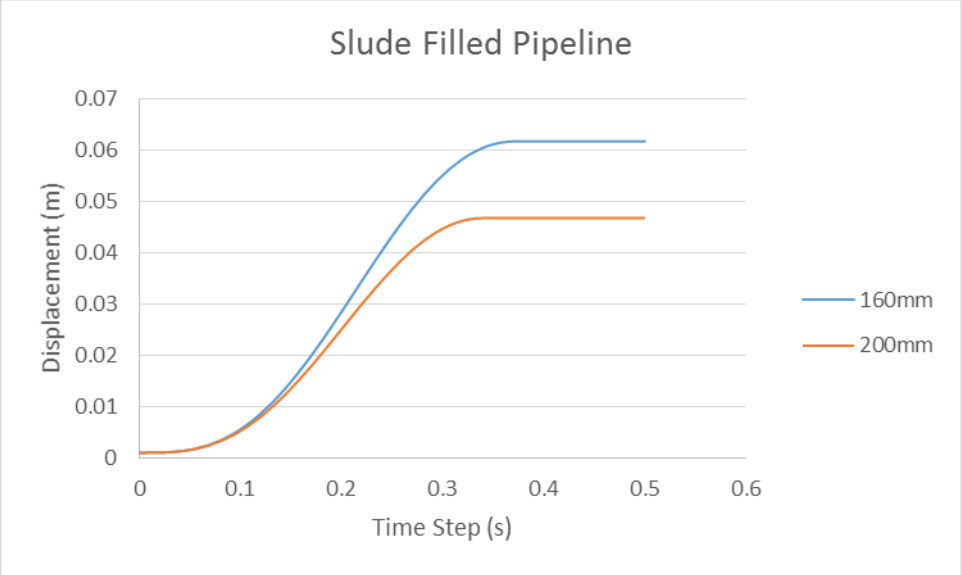

Figure 4.9: Uplift of sludge filled pipeline

What is concluded from the aforementioned results is the validation of several statements that have been made so far. These are:

- The results for the air/gas filled pipeline are almost identical between them and show a good fit as compared to the ones presented by (Horsten, 2016)
- The diameter of the pipeline is confirmed to be a critical affecting factor to uplift due to liquefaction and more specifically, larger diameters lead to lower uplift results.
- Last, but not least, it is observed that the weight of the pipeline due to the containing material greatly affects the extent to which uplift occurs. The relationship of this is, as expected, how larger weight leads to less uplift.

What has not yet been clarified is the extent to which burial depth and soil stiffness affect uplift. However, these will be investigated in greater depth later on in this report.

4.2.2 Influence of Burial Depth

As it has already been mentioned several times thus far in this report, one of the main influence factors to the pipeline's produced uplift is the burial depth. Furthermore, in this part, the pipeline cover considered was approximately 1.5m in all cases and as for the model considered, that was the single degree of freedom one.

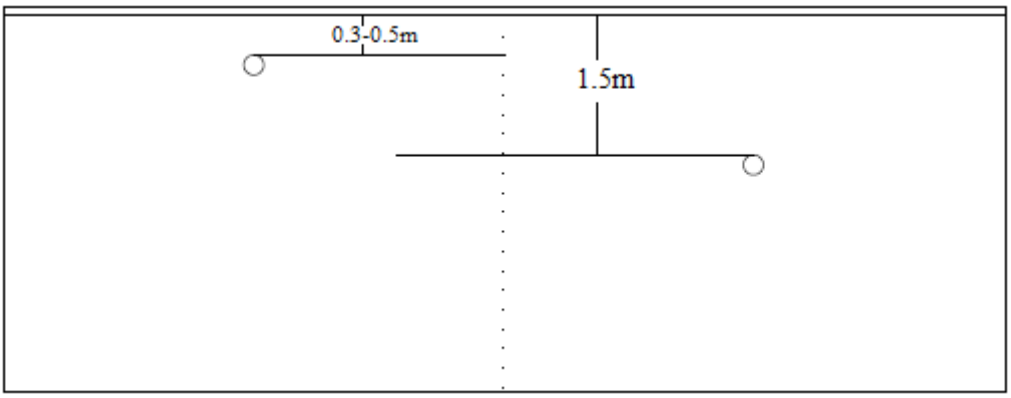

Figure 4.10: Change of burial depth

The produced results were:

Table 4.6: 1.5m cover uplift of gas filled pipeline

Diameter (mm)	160	200
Maximum Uplift (mm)	117	71

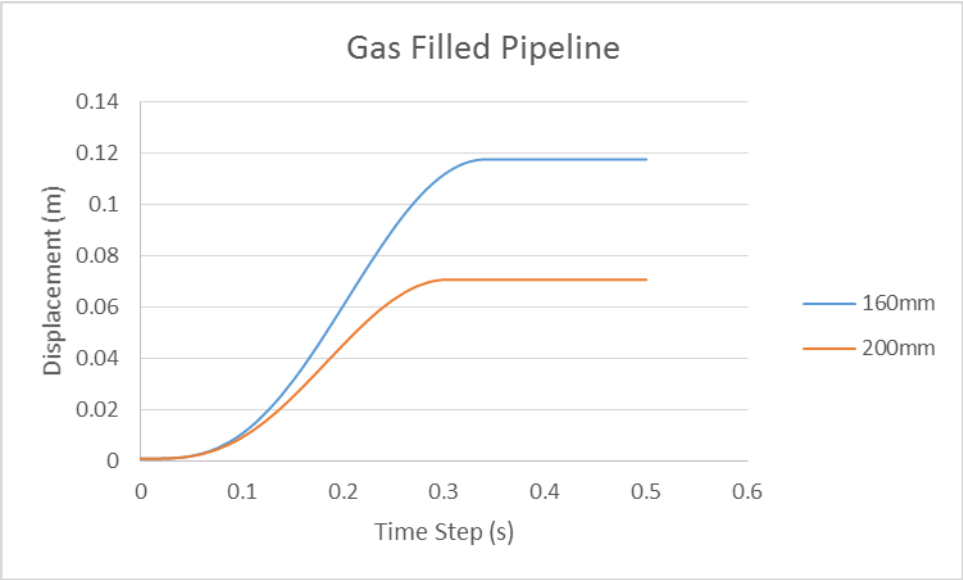

Figure 4.11: 1.5m cover uplift of gas filled pipeline

Table 4.7: 1.5m cover uplift of air filled pipeline

Diameter (mm)	160	200
Maximum Uplift (mm)	117	71

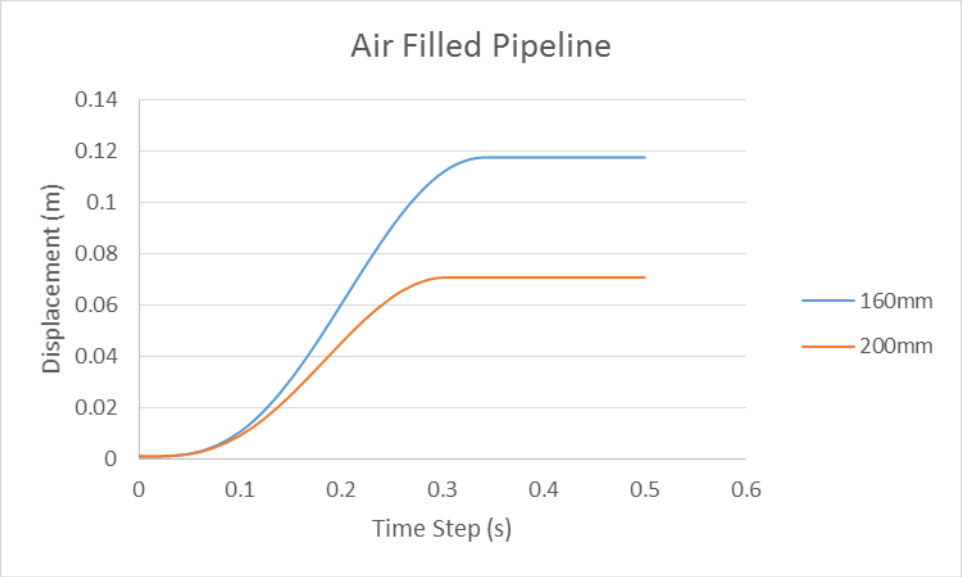

Figure 4.12: 1.5m cover uplift of air filled pipeline

Table 4.8: 1.5m cover uplift of oil filled pipeline

Diameter (mm)	160	200
Maximum Uplift (mm)	72	52

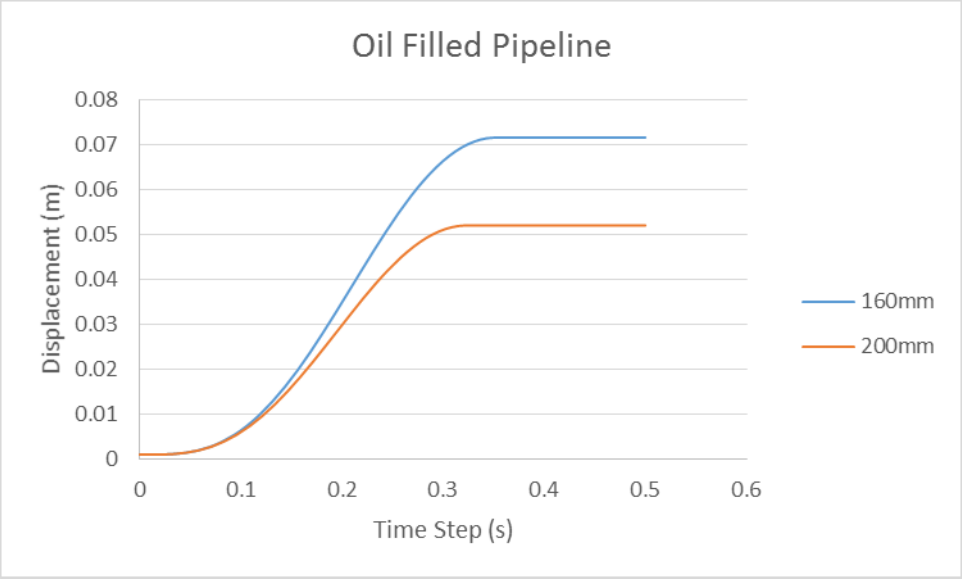

Figure 4.13: 1.5m cover uplift of gas filled pipeline

Table 4.9: 1.5m cover uplift of water filled pipeline

Diameter (mm)	160	200
Maximum Uplift (mm)	68	50

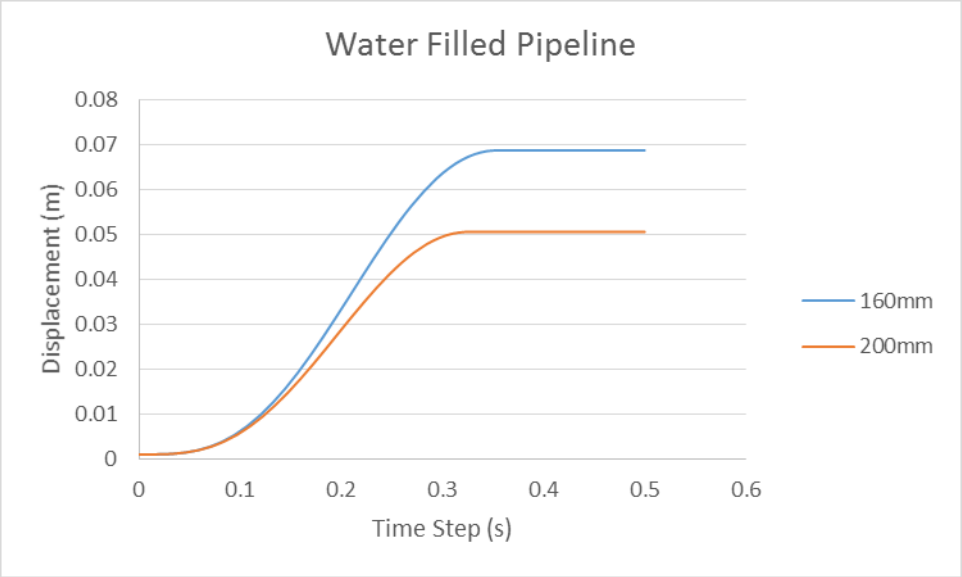

Figure 4.14: 1.5m cover uplift of water filled pipeline

Table 4.10: 1.5m cover uplift of sludge filled pipeline

Diameter (mm)	160	200
Maximum Uplift (mm)	55	43

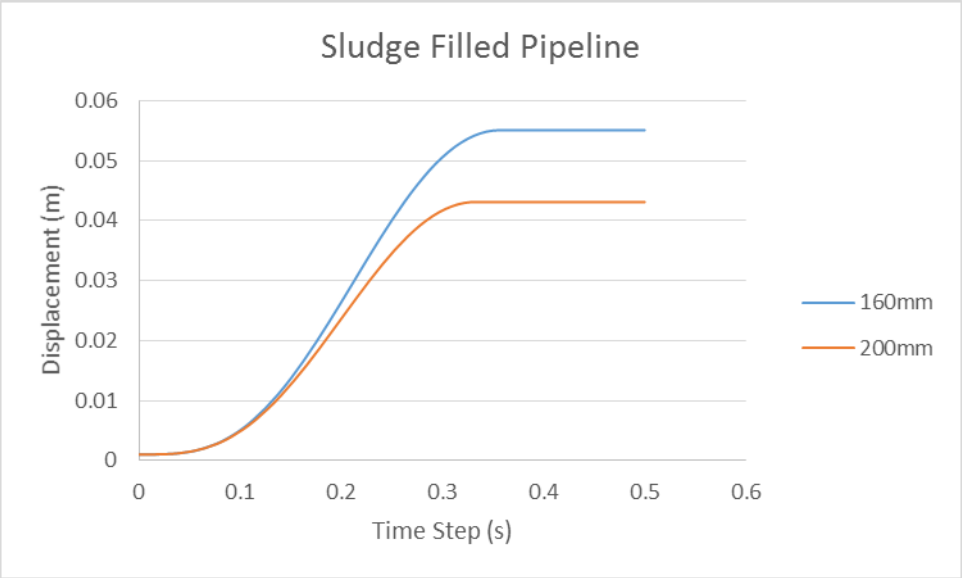

Figure 4.15: 1.5m cover uplift of sludge filled pipeline

Where what can be concluded from the results presented in this section is:

- As was expected, the larger cover/burial depth of 1.5m results to less resulting uplift as compared to the shallower depths presented before.
- The diameter and weight relationships with produced uplift are yet again present.
- Larger pipeline burial depths can be proved useful as a prevention technique against pipelines' failure due to uplift, as they are found to reduce the magnitude of uplift occurring.

4.2.3 Influence of Soil Stiffness

It was discussed in chapter 2 of this report how the last of the listed main factors, which influence a pipe's uplift was the soil's stiffness. For this analysis, a cover of approximately 1.5m was again considered but now with a stiffer soil's ground properties. The way with which this was made possible was a change to the input SPT N parameter with a larger one. Furthermore, the selection of the parameter was done with manual fit such that a relative density of 60% was now considered and corresponded by an N equal to 5.

The values which resulted were:

Table 4.11: Stiffer soil uplift of gas filled pipeline

Diameter (mm)	160	200
Maximum Uplift (mm)	107	66

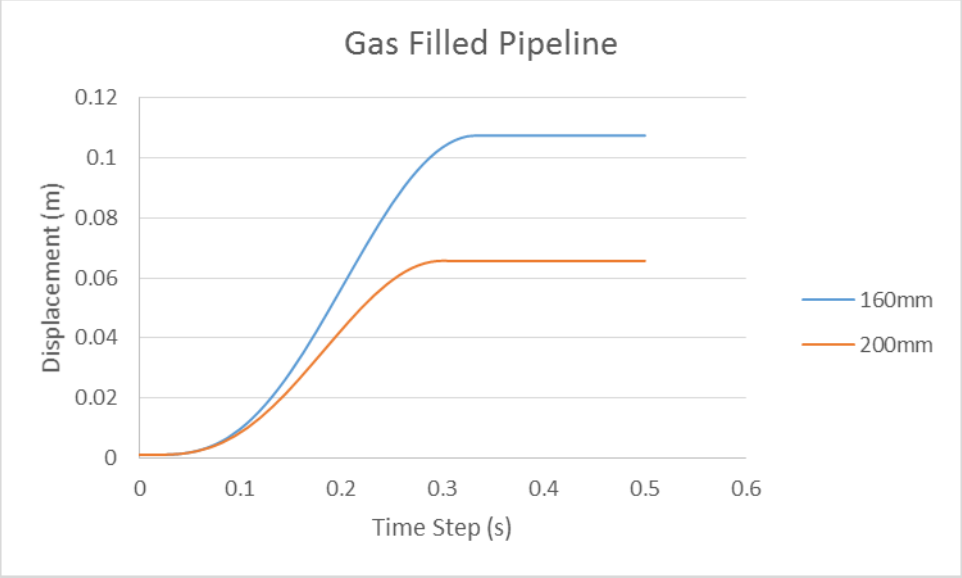

Figure 4.16: Stiffer soil uplift of gas filled pipeline

Table 4.12: Stiffer soil uplift of air filled pipeline

Diameter (mm)	160	200
Maximum Uplift (mm)	107	66

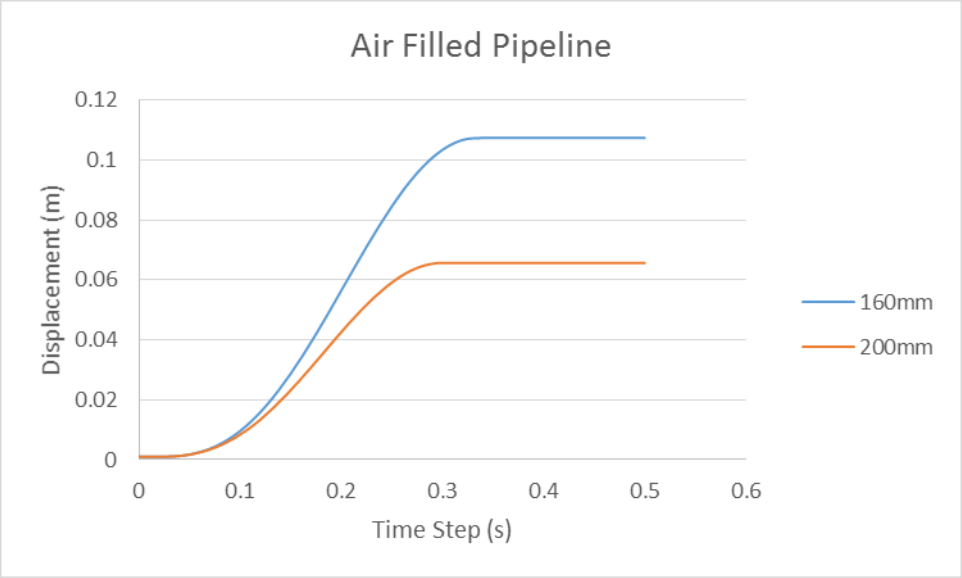

Figure 4.17: Stiffer soil uplift of air filled pipeline

Table 4.13: Stiffer soil uplift of oil filled pipeline

Diameter (mm)	160	200
Maximum Uplift (mm)	65	48

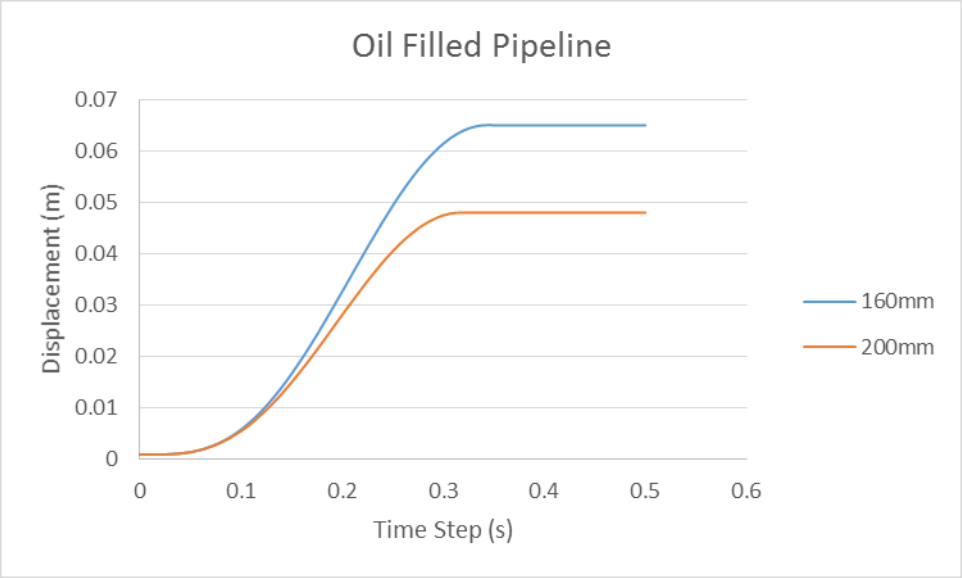

Figure 4.18: Stiffer soil uplift of oil filled pipeline

Table 4.14: Stiffer soil uplift of water filled pipeline

Diameter (mm)	160	200
Maximum Uplift (mm)	62	47

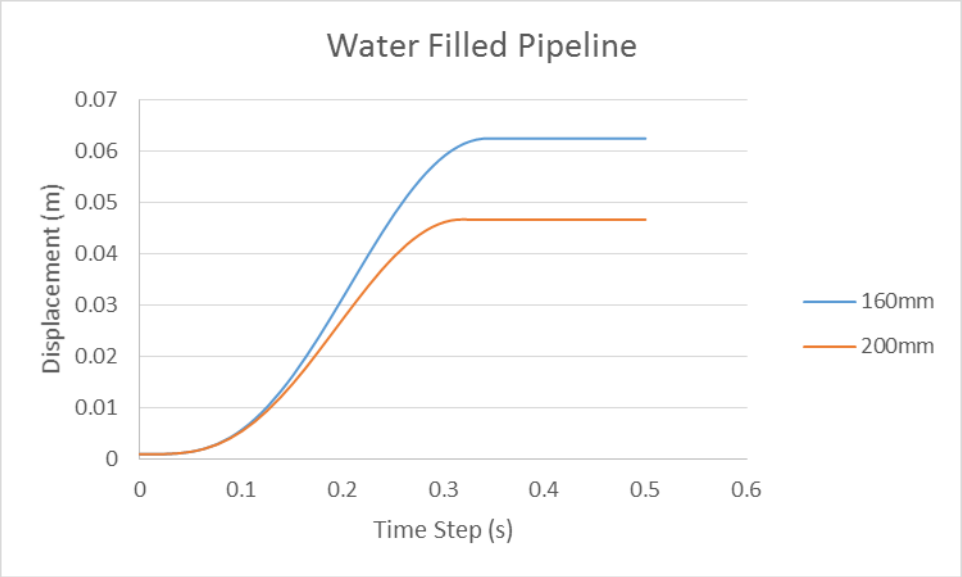

Figure 4.19: Stiffer soil uplift of water filled pipeline

Table 4.15: Stiffer soil uplift of sludge filled pipeline

Diameter (mm)	160	200
Maximum Uplift (mm)	50	40

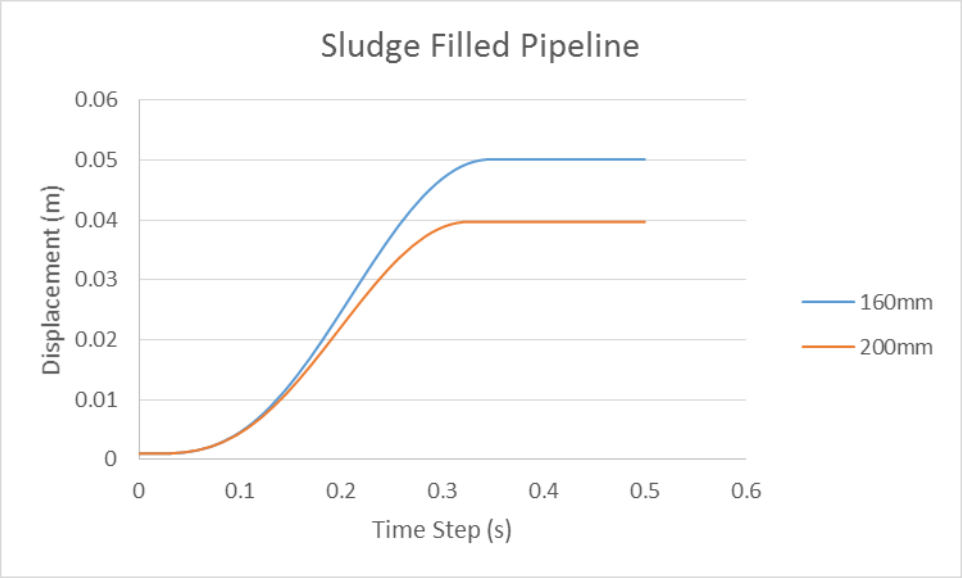

Figure 4.20: Stiffer soil uplift of sludge filled pipeline

Several conclusions could again be derived from these results, which summed up are:

- How stiffer soil conditions result in lower uplift values, just as expected.
- The trends of pipeline diameter and weight versus produced uplift remain constant.
- Stiffer ground conditions can serve as a prevention technique against pipeline's uplift due to liquefaction.

4.3 Multi Degree of Freedom

4.3.1 Initial Parameter Multi Degree of Freedom

The second section of this investigation involved a multi degree of freedom model. More specifically, as was explained in chapter 3, two degrees of freedom were considered, horizontal and vertical. A few things, which are worth to be mentioned here are how the vertical uplift force remained the same as described in the previous model while the horizontal fraction was considered as one tenth of the first. This ratio concluded that the direction of the resulting vector of force is located at 5.65° on the vertical axis and hence, the previously derived values for the single degree of freedom model were used.

In this case, the resulting values of uplift were as follows:

Table 4.16: Multi degree of freedom uplift of gas filled pipelines

Diameter (mm)	160	200
Maximum Uplift (mm)	202	101

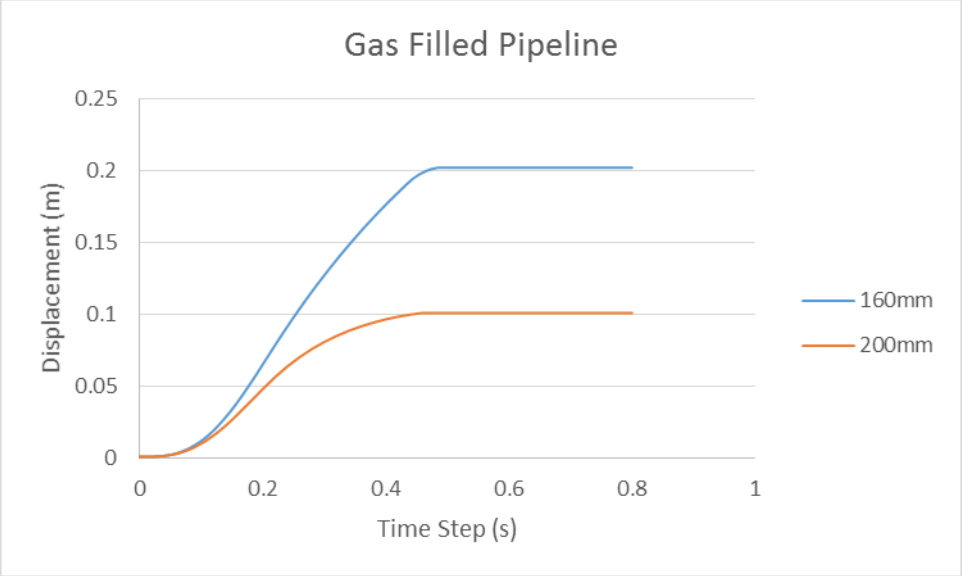

Figure 4.21: Multi Degree of freedom uplift of gas filled pipeline

It is worth mentioning at this point that, as was described in chapter 3 of this report, the solution of this model now lies in the complex number field, while the single degree of freedom one lied in the real one. Thus, in order for a direct comparison to be made between the two, the imaginary part of the two degree of freedom solution is ignored. The result of the aforementioned factor was exaggerated uplift values, as can be seen in figure 4.21.

Table 4.17: Multi degree of freedom uplift of air filled pipelines

Diameter (mm)	160	200
Maximum Uplift (mm)	202	101

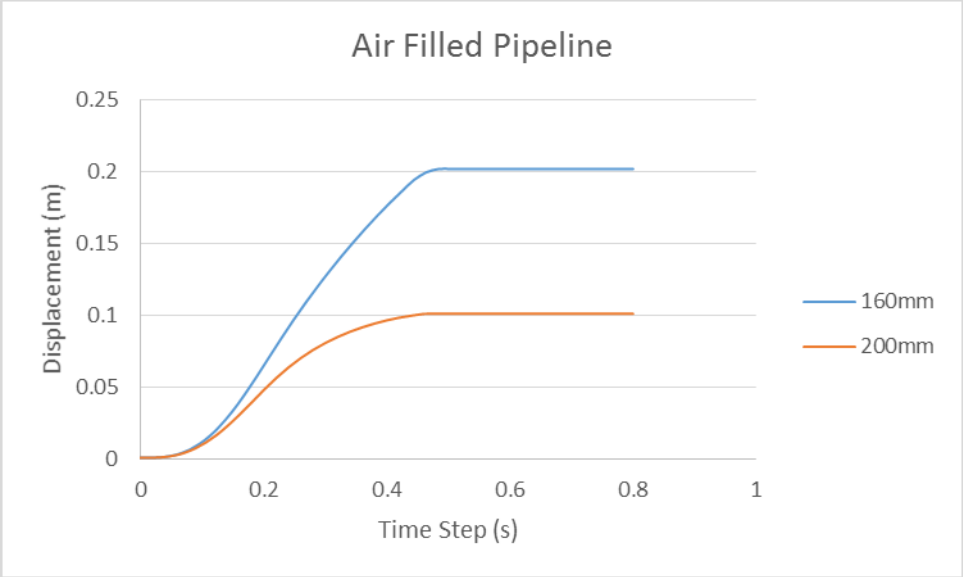

Figure 4.22Multi Degree of freedom uplift of air filled pipeline

Table 4.18: Multi degree of freedom uplift of oil filled pipelines

Diameter (mm)	160	200
Maximum Uplift (mm)	127	82

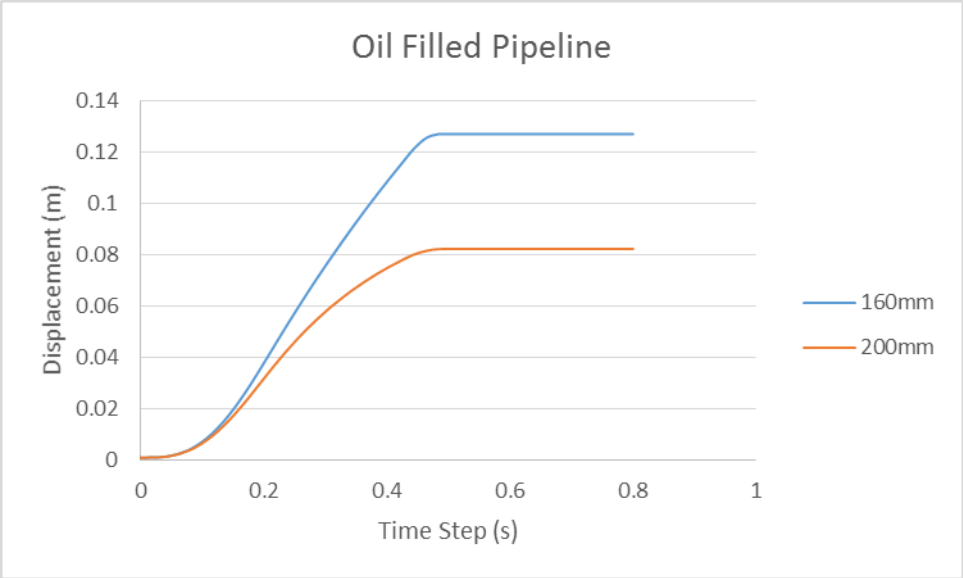

Figure 4.23: Multi Degree of Freedom Uplift of Oil Filled Pipeline

Table 4.19: Multi degree of freedom uplift of water filled pipelines

Diameter (mm)	160	200
Maximum Uplift (mm)	118	81

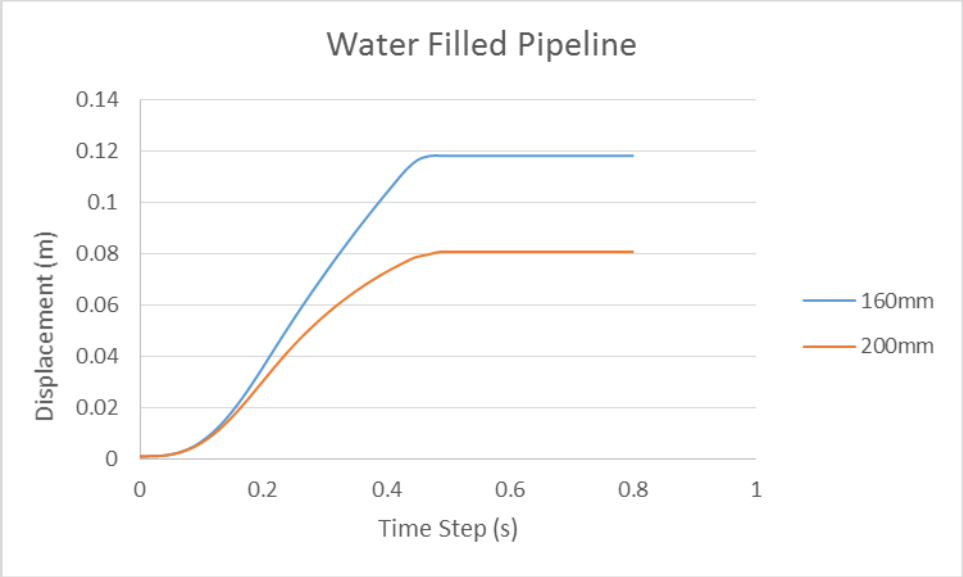

Figure 4.24: Multi Degree of Freedom Uplift of Water Filled Pipeline

Table 4.20: Multi degree of freedom uplift of sludge filled pipelines

Diameter (mm)	160	200
Maximum Uplift (mm)	98	71

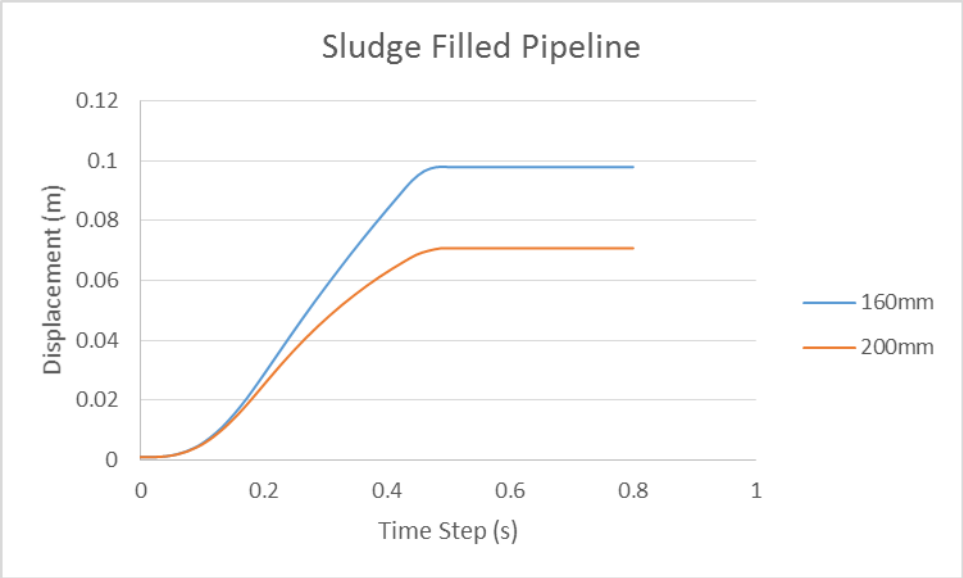

Figure 4.25: Multi Degree of Freedom Uplift of Sludge Filled Pipeline

Several things were concluded from the aforementioned results. These are:

- The confirmation of the relationships between produced uplift and the diameter of the pipeline, as well as its total weight.
- The time step at which maximum uplift is reached is larger than the one of the single degree of freedom solution.
- Production of exaggerated values due to the nature of the solution.

4.3.2 Influence of Burial Depth

Once again, the influence of burial depth was investigated as for the single degree of freedom model. Furthermore, the pipeline is placed to rest at a bottom point of 1.7m depth, while the cover at all times is approximately 1.5m.

Table 4.21: Multi degree of freedom uplift of 1.5m cover gas filled pipelines

Diameter (mm)	160	200
Maximum Uplift (mm)	189	93

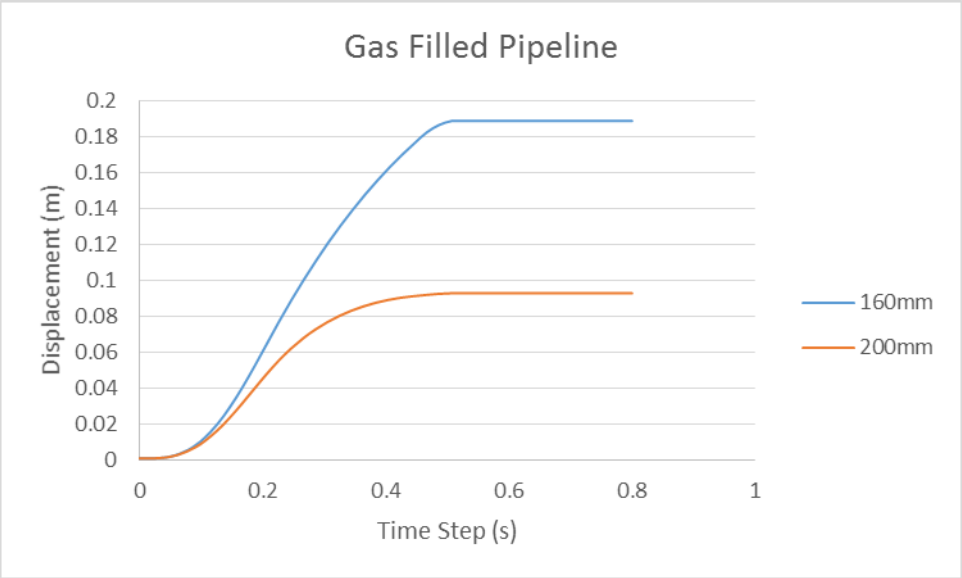

Figure 4.26: Multi degree of freedom uplift of 1.5m cover gas filled pipelines

Table 4.22: Multi degree of freedom uplift of 1.5m cover air filled pipelines

Diameter (mm)	160	200
Maximum Uplift (mm)	189	93

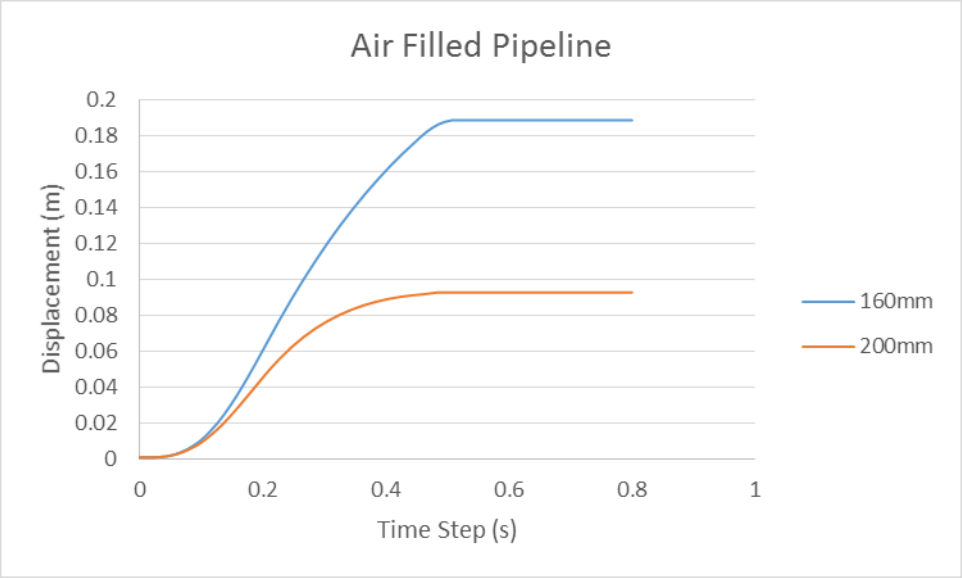

Figure 4.27: Multi degree of freedom uplift of 1.5m cover air filled pipelines

Table 4.23: Multi degree of freedom uplift of 1.5m cover oil filled pipelines

Diameter (mm)	160	200
Maximum Uplift (mm)	119	76

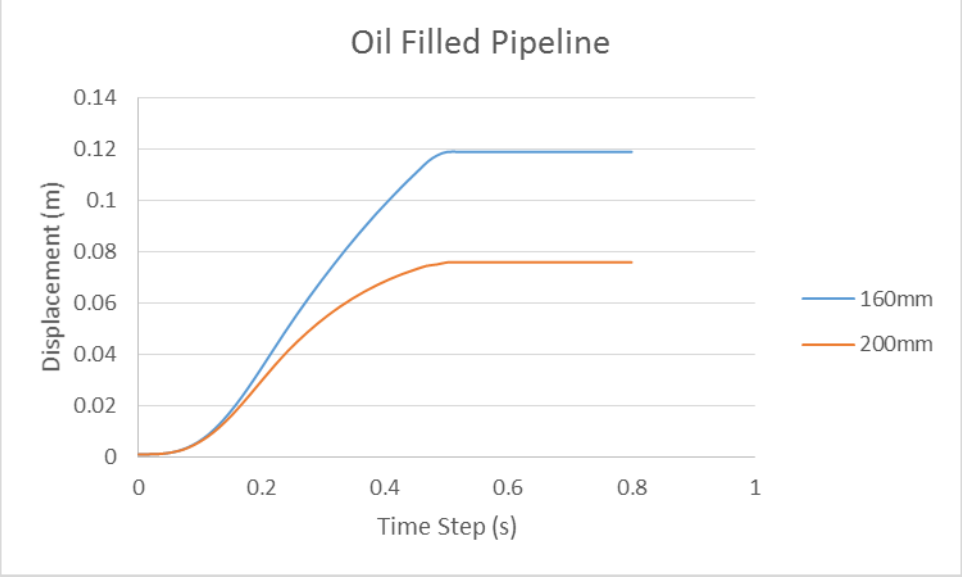

Figure 4.28: Multi degree of freedom uplift of 1.5m cover oil filled pipelines

Table 4.24: Multi degree of freedom uplift of 1.5m cover water filled pipelines

Diameter (mm)	160	200
Maximum Uplift (mm)	112	74

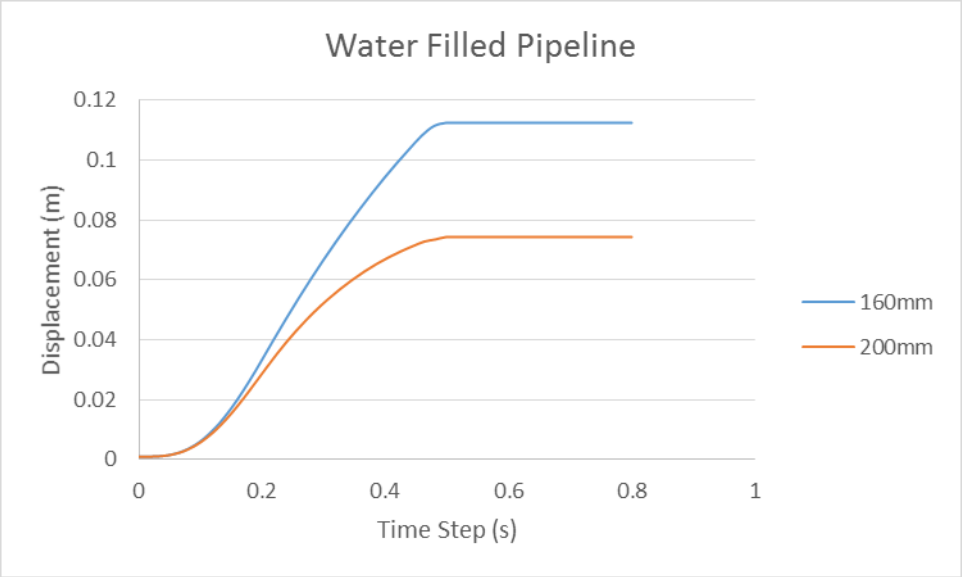

Figure 4.29: Multi degree of freedom uplift of 1.5m cover water filled pipelines

Table 4.25: Multi degree of freedom uplift of 1.5m cover sludge filled pipelines

Diameter (mm)	160	200
Maximum Uplift (mm)	90	66

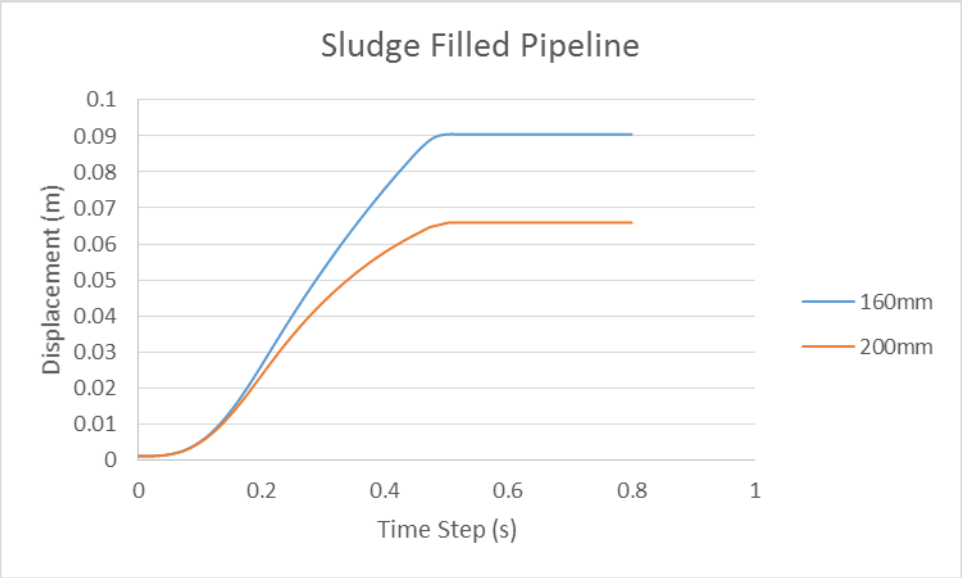

Figure 4.30: Multi degree of freedom uplift of 1.5m cover sludge filled pipelines

Once again, several conclusions can be derived from the results presented in this section.

- First of all, the general trend is once again in agreement with the one derived from the respective single degree of freedom analysis where larger burial depth was found to lead to smaller values of pipe uplift.
- The effect of weight and diameter is yet again present in the aforementioned results.
- The point at which maximum uplift was observed was larger than the one of the single degree of freedom model.
- Exaggerated results are presented due to the complex field number nature of the solution.

4.3.3 Influence of Soil Stiffness

Next, the influence of the soil's stiffness was investigated for the case of the multi-degree of freedom model and compared to the corresponding values of the single degree of freedom model. As was the case in the investigation of the latter, the pipelines are placed to rest at a bottom point of 1.7m depth, with an approximate cover depth of 1.5m. However, in this case the soil's input parameters are the ones explained before for stiff conditions. Furthermore, the findings were:

Table 4.26: Stiffer soil multi degree of freedom uplift of gas filled pipelines

Diameter (mm)	160	200
Maximum Uplift (mm)	167	83

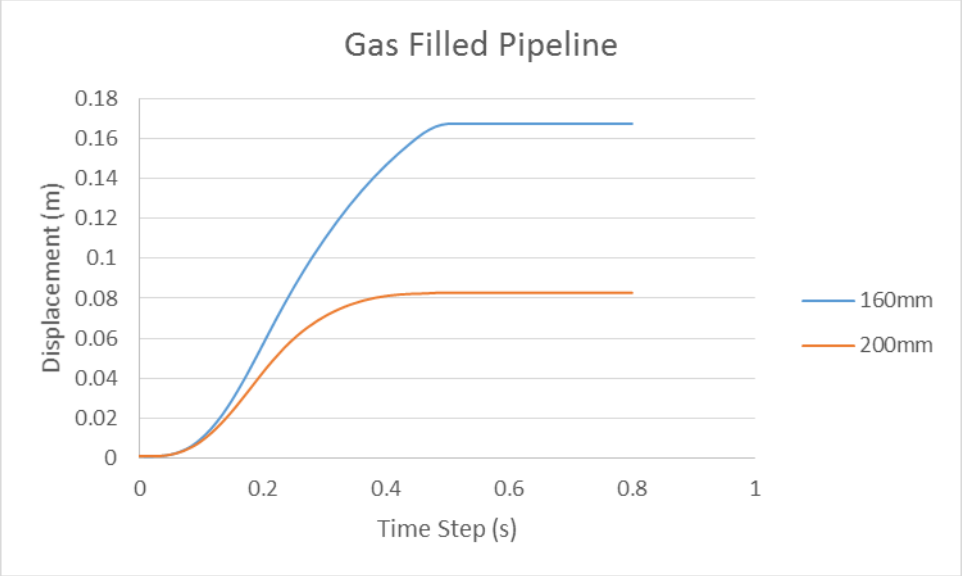

Figure 4.31: Stiffer soil multi degree of freedom uplift of gas filled pipelines

Table 4.27: Stiffer soil multi degree of freedom uplift of air filled pipelines

Diameter (mm)	160	200
Maximum Uplift (mm)	167	83

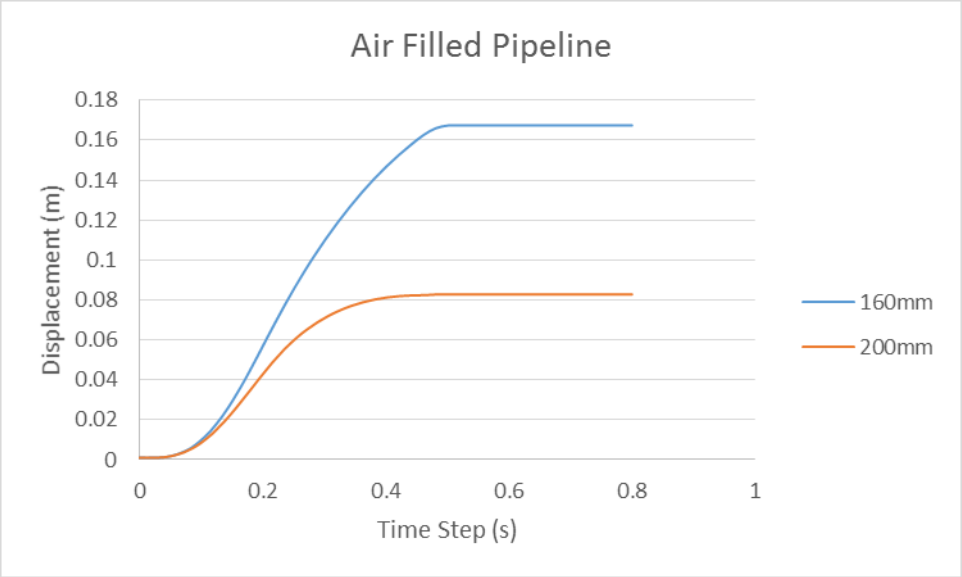

Figure 4.32: Stiffer soil multi degree of freedom uplift of air filled pipelines

Table 4.28: Stiffer soil multi degree of freedom uplift of oil filled pipelines

Diameter (mm)	160	200
Maximum Uplift (mm)	106	68

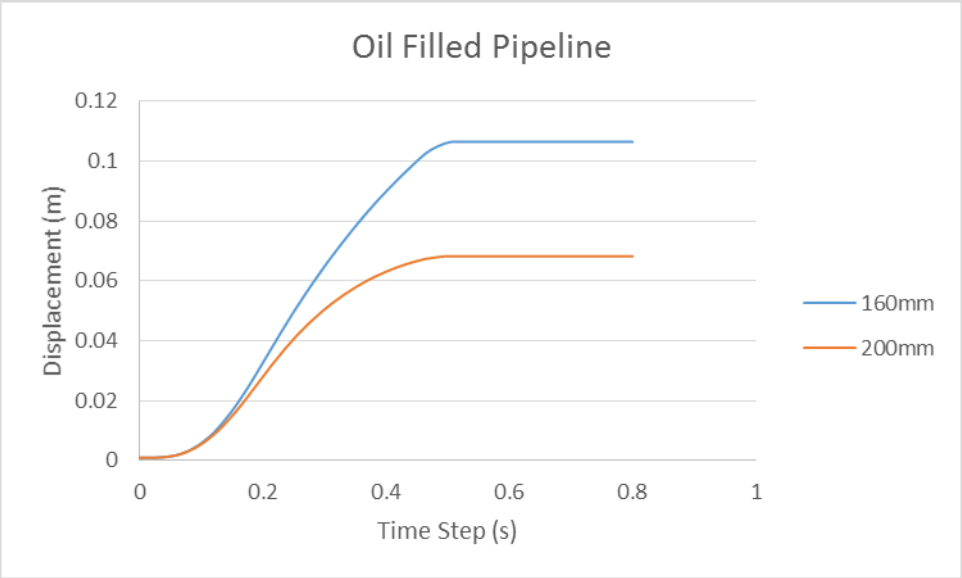

Figure 4.33: Stiffer soil multi degree of freedom uplift of oil filled pipelines

Table 4.29: Stiffer soil multi degree of freedom uplift of water filled pipelines

Diameter (mm)	160	200
Maximum Uplift (mm)	102	66

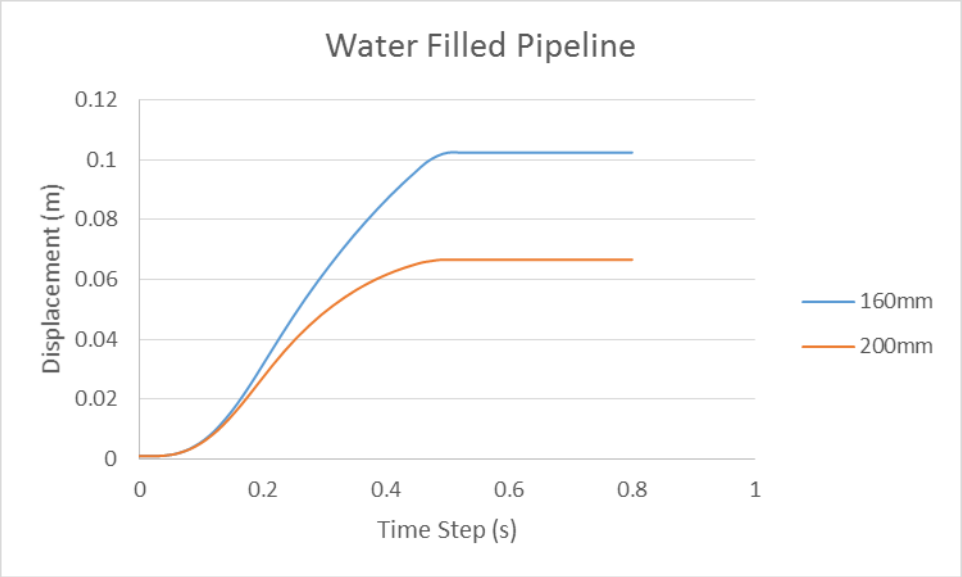

Figure 4.34: Stiffer soil multi degree of freedom uplift of water filled pipelines

Table 4.30: Stiffer soil multi degree of freedom uplift of sludge filled pipelines

Diameter (mm)	160	200
Maximum Uplift (mm)	85	59

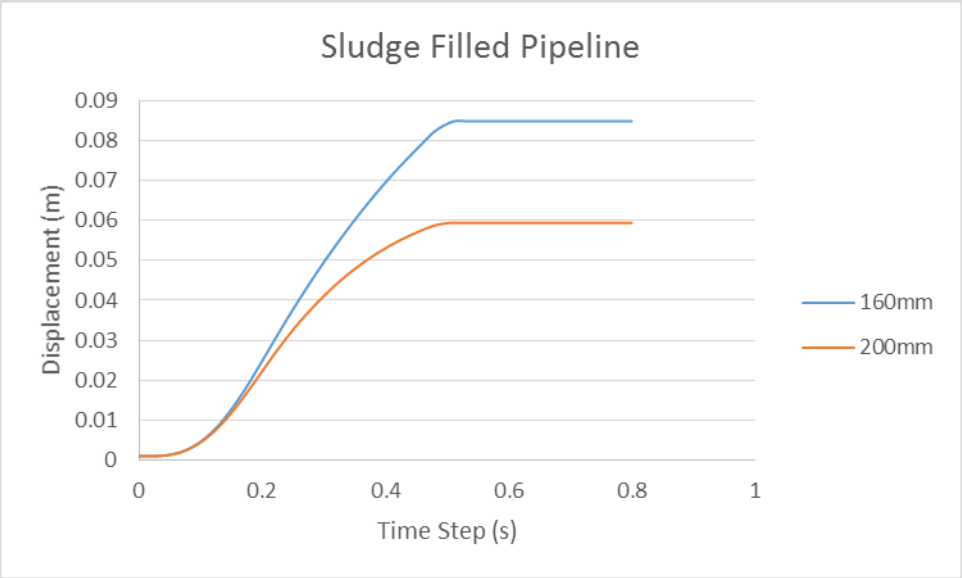

Figure 4.35: Stiffer soil multi degree of freedom uplift of water filled pipelines

The conclusions which can be derived from the results presented in this section are as follows:

- Once again, just like in the single degree of freedom model, stiffer soil conditions lead to lower uplift values and the trend remains in agreement with the previous relevant results presented so far.
- The effect of pipeline weight and diameter is yet again the same as the previous studies.
- Maximum uplift is observed at a time step larger than the single degree of freedom model but comparable to the previous one of the multi-degree of freedom investigations.
- Exaggerated results are once again present.

4.3.4 Influence of Dashpot Coefficient

The dashpot coefficient expresses a resistance to an applied force. It can then be derived how with the addition of an extra force, corresponding dashpot coefficients and their effect on the produced results also have to be investigated. This was made possible by linear fit between the initial parameter results of both models. More specifically, the values which were found to be appropriate for the 160 and 200mm diameter pipelines were 300 and 900 kN*s/m respectively. The results were as follows in this chapter.

Table 4.31: Multi degree of freedom uplift of gas filled pipelines with larger dashpot coefficients

Diameter (mm)	160	200
Maximum Uplift (mm)	123	74

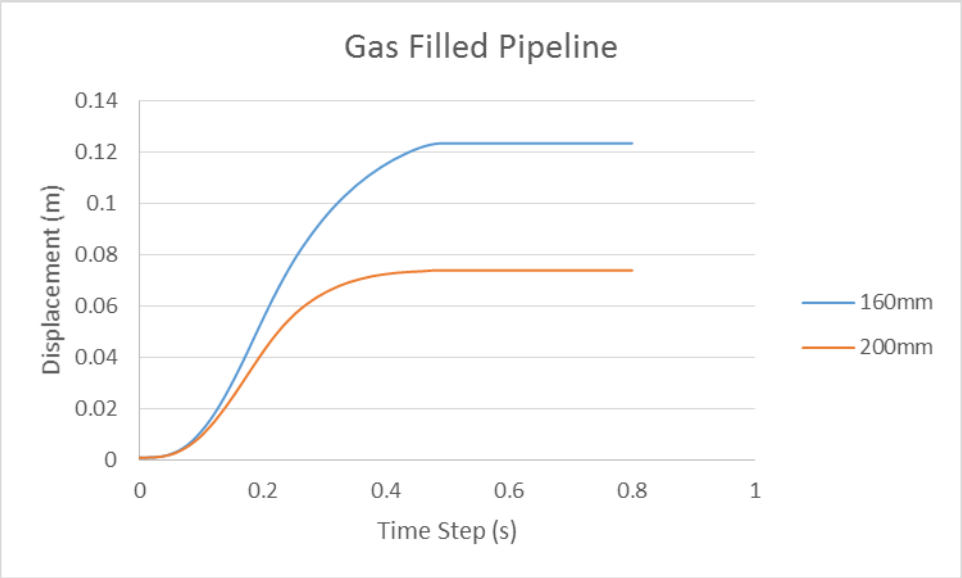

Figure 4.36: Multi degree of freedom uplift of gas filled pipelines with larger dashpot coefficients

Table 4.32: Multi degree of freedom uplift of air filled pipelines with larger dashpot coefficients

Diameter (mm)	160	200
Maximum Uplift (mm)	123	74

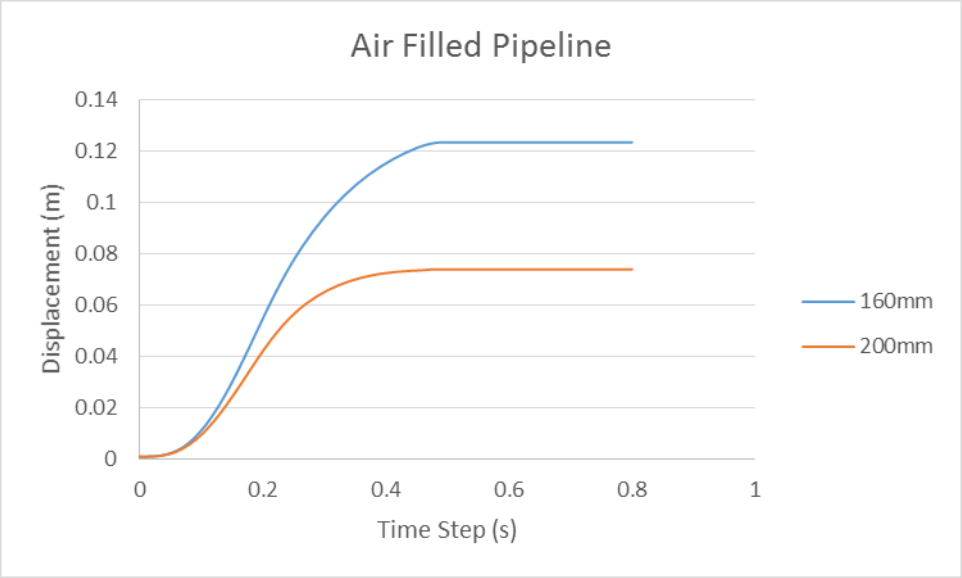

Figure 4.37: Multi degree of freedom uplift of air filled pipelines with larger dashpot coefficients

Table 4.33: Multi degree of freedom uplift of oil filled pipelines with larger dashpot coefficients

Diameter (mm)	160	200
Maximum Uplift (mm)	95	65

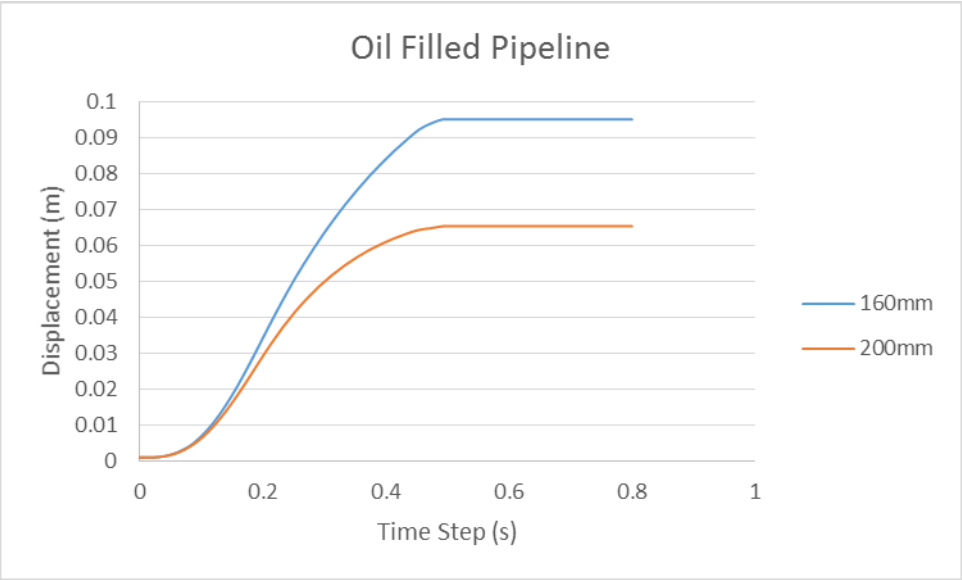

Figure 4.38: Multi degree of freedom uplift of oil filled pipelines with larger dashpot coefficients

Table 4.34: Multi degree of freedom uplift of water filled pipelines with larger dashpot coefficients

Diameter (mm)	160	200
Maximum Uplift (mm)	93	64

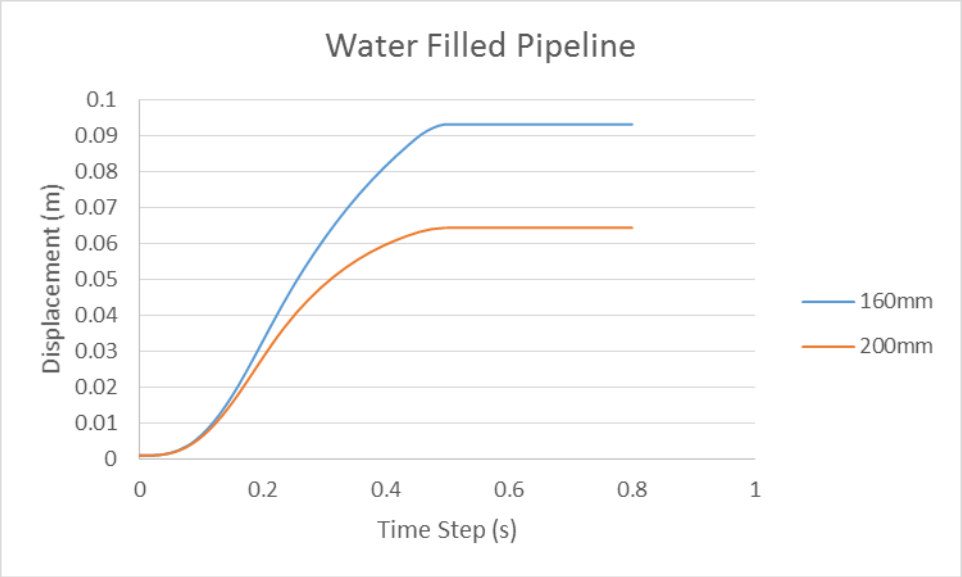

Figure 4.39: Multi degree of freedom uplift of water filled pipelines with larger dashpot coefficients

Table 4.35: Multi degree of freedom uplift of sludge filled pipelines with larger dashpot coefficients

Diameter (mm)	160	200
Maximum Uplift (mm)	81	57

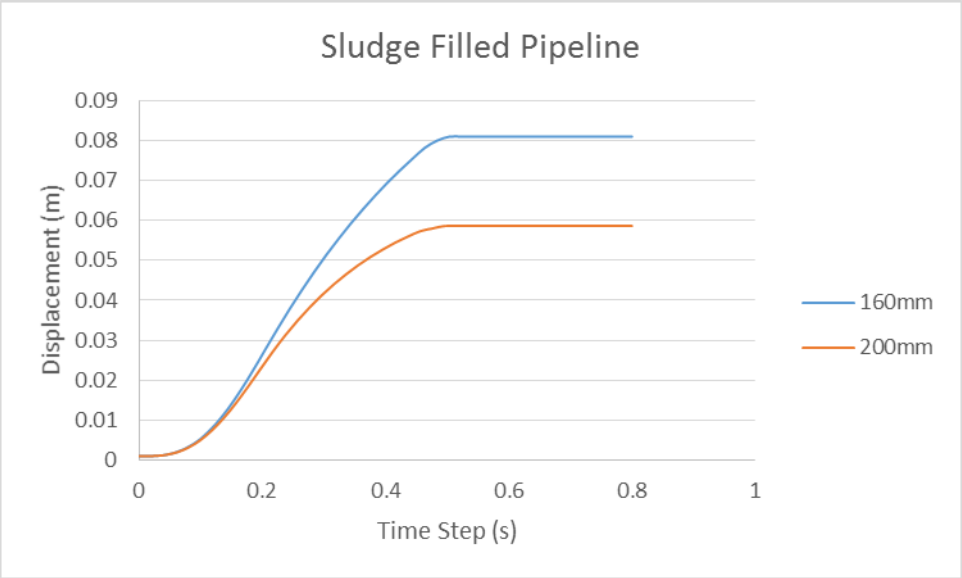

Figure 4.40: Multi degree of freedom uplift of sludge filled pipelines with larger dashpot coefficients

The conclusions of this section are:

- Larger dashpot coefficients tend to produce more realistic results, when compared with all the previous corresponding findings derived in this report as well as the ones presented from previous investigations.
- The point at which maximum uplift is observed is yet again in accordance to the one of the multi-degree of freedom model and not the single degree of freedom one.
- The general trends of diameter and weight effects once again remain constant.

5 Conclusions & Recommendations

5.1 Conclusions

Summing up, the following can be deduced from this report:

- Beam-Spring models with Kelvin-Voigt spring and dashpot are an appropriate means of predicting post liquefaction pipelines' displacement.
- The post-liquefaction p-y curve method produced by (Dash et al., 2017) is confirmed to yield satisfactory results.
- Larger pipe diameter tends to produce smaller uplift results.
- Pipelines with greater self or total weight are expected to show lower uplift values.
- The burial depth of the investigated pipelines was also an affecting factor. More specifically, pipelines placed under larger covers were found to be less uplifted than the ones buried shallower in both single and multi-degree of freedom models.
- The soil stiffness was also found to play a great part in the degree at which post-liquefaction uplift is present. Furthermore, less uplift was found to occur for pipelines buried in stiffer ground conditions for both models.
- The pipe models in this report can be used for the production of soil-structure interaction analysis between post-liquefied ground and pipelines when the appropriate input parameters are available.

5.2 Recommendations

Some recommendations are stated in this part, concerning real life applications of this report's findings as well as propositions for future research.

- Use of heavier pipelines, with larger diameter and thickness is recommended when the given ground profile suggests that liquefaction is a possible hazard. It would be worth mentioning how the difference in price between 160 and 200mm pipelines varies from 5.5 to 20 euro per running meter, depending on the selected steel grade, with the 200mm ones being more expensive.
- Soil densification, by means of compaction is found to be a great prevention mechanism against pipe failure due to uplift phenomena which result from liquefaction and post-liquefaction. In terms of cost, that would have to be calculated project-specific as the required type of machinery as well as the required renting time would vary depending on the project's magnitude and conditions. Furthermore, a cost analysis between compaction and larger diameter pipelines is recommended for the most efficient solution to be determined.
- It is also recommended that when pipelines are to be placed in grounds prone to liquefaction the burial depth should be considered. More specifically, a larger burial depth can be used as a preventive mechanism against failure due to uplift in cases of critical displacement.
- It is suggested that more preventive techniques are investigated in the future, such as the use of piles under pipelines and their effect against uplift.
- Experimental procedures could be used for further investigation of damping coefficients in liquefied and post-liquefied soil-structure interaction conditions. More specifically, a relationship between single and multi-degree of freedom condition dashpots could be established as well as a standard table of practise for both single and multi-degree of freedom models.

Bibliography

ASCE-ALA. (2005). Seismic Guidelines for Water Pipelines March 2005, (March).

Bartlett, S., & Youd, T. L. (1995). Liquefaction-induced lateral spread displacement. *Journal of Geotechnical Engineering*, *121*(4), 316–329.

Berghe, J. Vanden, Cathie, D., & Ballard, J. (2001). Analyse des mécanismes de soulèvement de pipelines par eléments finis, (1986), 1801–1804. https://doi.org/10.3233/978-1-61499-656-9-1801

Boulanger, R. W., & Idriss, I. M. (2014). CPT and SPT based liquefaction triggering procedures. *Center for Geotechnical Modeling*, (April), 134.

Braja M. Das. (2011). *Geotehnical engineering handbook*.

Cheuk, C. Y., White, D. J., & Bolton, M. D. (2008). Uplift Mechanisms of Pipes Buried in Sand. *Journal of Geotechnical and Geoenvironmental Engineering*, *134*(2), 154–163. https://doi.org/10.1061/(ASCE)1090-0241(2008)134:2(154)

Chhabra, R. P. (2010). Non-Newtonian fluids: An introduction. *Rheology of Complex Fluids*, 3–34. https://doi.org/10.1007/978-1-4419-6494-6_1

Chian, S. C., Tokimatsu, K., Asce, M., Phani, S., & Madabhushi, G. (2014). Soil Liquefaction – Induced Uplift of Underground Structures : Physical and Numerical Modeling. *Journal of Geotechnical and Geoenvironmental Engineering*, *140*(10), 1–18. https://doi.org/10.1061/(ASCE)GT.1943-5606.0001159.

Chopra, A. K. (1995). Dynamics of Structures, 794.

Dash, S., Rouholamin, M., Lombardi, D., & Bhattacharya, S. (2017). A practical method for construction of p-y curves for lique fi able soils. *Soil Dynamics and Earthquake Engineering*, *97*(March), 478–481. https://doi.org/10.1016/j.soildyn.2017.03.002

Deltares. (2016). D-GEO PIPELINE.

Faeli, Z., & Fakher, A. (2010). Allowable Differential Settlement of Oil Pipelines. *International Journal of Engineering*, *4*(4), 308–320.

Hededal, O., & Klinkvort, R. T. (2010). A new elasto-plastic spring element for cyclic loading of piles using the p-y-curve concept. *Numerical Methods in Geotechnical Engineering*, 883–888.

Horsten, T. (2016). Pipe uplift in liquefied sands.

Huang, B., Liu, J., Lin, P., & Ling, D. (2014). Uplifting behavior of shallow buried pipe in liquefiable soil by dynamic centrifuge test. *Scientific World Journal*, *2014*. https://doi.org/10.1155/2014/838546

Huang, Y., & Yu, M. (2013). Review of soil liquefaction characteristics during major earthquakes of the twenty-first century. *Natural Hazards*, *65*(3), 2375–2384. https://doi.org/10.1007/s11069-012-0433-9

Hwang, J. I., Kim, C. Y., Chung, C. K., & Kim, M. M. (2006). Viscous fluid characteristics of liquefied soils and behavior of piles subjected to flow of liquefied soils. *Soil Dynamics and Earthquake Engineering*, *26*(2–4 SPEC. ISS.), 313–323. https://doi.org/10.1016/j.soildyn.2005.02.020

Idriss, I. M., & Boulanger, R. W. (2010). SPT-Based liquefaction triggering procedures, (UCD/CGM-

10/02), 1–127. https://doi.org/UCD/CGM-10/02

Jóźwiak, B., Orczykowska, M., & Dziubiński, M. (2015). Fractional generalizations of Maxwell and Kelvin-Voigt models for biopolymer characterization. *PLoS ONE*, *10*(11), 1–19. https://doi.org/10.1371/journal.pone.0143090

Kacar, A., Tan, H. T., & Kaya, M. O. (2011). Free vibration analysis of beams on variable winkler elastic foundation by using the differential transform method. *Mathematical and Computational Applications*, *16*(3), 773–783.

Kelly, P. (2015). Solid Mechanics Part 1, 283–343.

Knappett, J. a, & Craig, R. F. (2012). *Craig ' s Soil Mechanics*.

Kouretzis, G. P., Krabbenhøft, K., Sheng, D., & Sloan, S. W. (2014). Soil-buried pipeline interaction for vertical downwards relative offset. *Canadian Geotechnical Journal*, *51*(10), 1087–1094. https://doi.org/10.1139/cgj-2014-0029

López-Guerra, E. A., & Solares, S. D. (2014). Modeling viscoelasticity through spring-dashpot models in intermittent-contact atomic force microscopy. *Beilstein Journal of Nanotechnology*, *5*(1), 2149–2163. https://doi.org/10.3762/bjnano.5.224

Naggar, M. H. El, & Bentley, K. J. (2000). Dynamic analysis for laterally loaded piles and dynamic *p-y* curves. *Canadian Geotechnical Journal*, *37*(6), 1166–1183. https://doi.org/10.1139/cgj-37-6-1166

O'Rourke, M. J., & Liu, J. X. (2012). *Seismic Design of Buried and Offshore Pipelines*.

Sahoo, R. N., Reddy, D. V., & Sukhija, B. S. (2007). Evidence of liquefaction near Baramulla (Jammu and Kashmir, India) due to the 2005 Kashmir earthquake. *Current Science*, *92*(3), 293–295.

Sumer, B. M., Fredsøe, J., Christensen, S., & Lind, M. T. (1999). Sinking r floatation of pipelines and other objects in liquefied soil under waves, 53–90.

Yang, Z., & Elgamal, A. (2001). Sand Boils and Liquefaction--Induced Lateral Deformation. *15th International Conference on Soil Mechanics and Geotechnical Engineering*, *1989*, 345–350.

Appendix A

Tioga

Philadelphia Regional Center
2650 Whitehall Lane
Philadelphia, PA 19137
O 215-821-0700
F 215-533-1645
E sales@tiogapipe.com

Houston Regional Center
616 FM 1960 W, Suite 700
Houston, TX 77090
O 713-433-2111
F 281-397-0132
E sales@tiogapipe.com

Chattanooga Regional Center
1201 Riverfront Parkway, Suite 106
Chattanooga, TN 37402
O 423-899-3398
F 423-899-9695
E sales@tiogapipe.com

PIPE DIMENSIONS AND WEIGHTS

Available in commercial and nuclear

U.S./METRIC

NOMINAL PIPE SIZE	OD	SCHEDULE DESIGNATIONS			WALL THICKNESS		WEIGHT		ID	
INCH MM	INCH MM	ASME			INCH	MM	LBS/FOOT	KG/METER	INCH	MM
1/8 6	0.405 10.3	10		10S	0.049	1.24	0.19	0.28	0.307	7.80
		STD	40	40S	0.068	1.73	0.24	0.37	0.269	6.84
		XS	80	80S	0.095	2.41	0.31	0.47	0.215	5.84
1/4 8	0.540 13.7	10		10S	0.065	1.65	0.33	0.49	0.410	10.40
		STD	40	40S	0.088	2.24	0.43	0.63	0.364	9.22
		XS	80	80S	0.119	3.02	0.54	0.80	0.302	7.66
3/8 10	0.675 17.1	10		10S	0.065	1.65	0.42	0.63	0.545	13.80
		STD	40	40S	0.091	2.31	0.57	0.84	0.493	12.48
		XS	80	80S	0.126	3.20	0.74	1.10	0.423	10.70
1/2 15	0.840 21.3	5		5S	0.065	1.65	0.54	0.80	0.710	18.00
		10		10S	0.083	2.11	0.67	1.00	0.674	17.08
		STD	40	40S	0.109	2.77	0.85	1.27	0.622	15.76
		XS	80	80S	0.147	3.73	1.09	1.62	0.546	13.84
		160			0.188	4.78	1.31	1.95	0.464	11.74
		XX			0.294	7.47	1.72	2.55	0.252	6.36
3/4 20	1.050 26.7	5		5S	0.065	1.65	0.69	1.03	0.920	23.40
		10		10S	0.083	2.11	0.86	1.28	0.884	22.48
		STD	40	40S	0.113	2.87	1.13	1.69	0.824	20.96
		XS	80	80S	0.154	3.91	1.48	2.20	0.742	18.88
		160			0.219	5.56	1.95	2.90	0.613	15.58
		XX			0.308	7.82	2.44	3.64	0.434	11.06
1 25	1.315 33.4	5		5S	0.065	1.65	0.87	1.29	1.185	30.10
		10		10S	0.109	2.77	1.41	2.09	1.097	27.86
		STD	40	40S	0.133	3.38	1.68	2.50	1.049	26.64
		XS	80	80S	0.179	4.55	2.17	3.24	0.957	24.30
		160			0.250	6.35	2.85	4.24	0.815	20.70
		XX			0.358	9.09	3.66	5.45	0.599	15.22
1-1/4 32	1.660 42.2	5		5S	0.065	1.65	1.11	1.65	1.530	38.90
		10		10S	0.109	2.77	1.81	2.69	1.442	36.66
		STD	40	40S	0.140	3.56	2.27	3.39	1.380	35.08
		XS	80	80S	0.191	4.85	3.00	4.47	1.278	32.50
		160			0.250	6.35	3.77	5.61	1.160	29.50
		XX			0.382	9.70	5.22	7.77	0.896	22.80
1-1/2 40	1.900 48.3	5		5S	0.065	1.65	1.28	1.90	1.770	45.00
		10		10S	0.109	2.77	2.09	3.11	1.682	42.76
		STD	40	40S	0.145	3.68	2.72	4.05	1.610	40.94
		XS	80	80S	0.200	5.08	3.63	5.41	1.500	38.14
		160			0.281	7.14	4.86	7.25	1.338	34.02
		XX			0.400	10.15	6.41	9.55	1.100	28.00
2 50	2.375 60.3	5		5S	0.065	1.65	1.61	2.39	2.245	57.00
		10		10S	0.109	2.77	2.64	3.93	2.157	54.76
		STD	40	40S	0.154	3.91	3.66	5.44	2.067	52.48
		XS	80	80S	0.218	5.54	5.03	7.48	1.939	49.22
		160			0.344	8.74	7.47	11.11	1.687	42.82
		XX			0.436	11.07	9.04	13.44	1.503	38.16
2-1/2 65	2.875 73.0	5		5S	0.083	2.11	2.48	3.69	2.709	68.78
		10		10S	0.120	3.05	3.53	5.26	2.625	66.90
		STD	40	40S	0.203	5.16	5.80	8.63	2.469	62.68
		XS	80	80S	0.276	7.01	7.67	11.41	2.323	58.98
		160			0.375	9.53	10.02	14.92	2.125	53.94
		XX			0.552	14.02	13.71	20.39	1.771	44.96
3 80	3.500 88.9	5		5S	0.083	2.11	3.03	4.52	3.334	84.68
		10		10S	0.120	3.05	4.34	6.46	3.260	82.80
		STD	40	40S	0.216	5.49	7.58	11.29	3.068	77.92
		XS	80	80S	0.300	7.62	10.26	15.27	2.900	73.66
		160			0.438	11.13	14.34	21.35	2.624	66.64
		XX			0.600	15.24	18.60	27.68	2.300	58.42
3-1/2 90	4.000 101.6	5		5S	0.083	2.11	3.48	5.18	3.834	97.38
		10		10S	0.120	3.05	4.98	7.41	3.760	95.50
		STD	40	40S	0.226	5.74	9.12	13.57	3.548	90.12
		XS	80	80S	0.318	8.08	12.51	18.64	3.364	85.44
		XX			0.636	16.15	22.85	34.03	2.728	69.30
4 100	4.500 114.3	5		5S	0.083	2.11	3.92	5.84	4.334	110.08
		10		10S	0.120	3.05	5.62	8.37	4.260	108.20
					0.156	3.96	7.24	10.78	4.188	106.38
					0.188	4.78	8.67	12.91	4.124	104.74
		STD	40	40S	0.237	6.02	10.80	16.08	4.026	102.26
		XS	80	80S	0.337	8.56	15.00	22.32	3.826	97.18
		120			0.438	11.13	19.02	28.32	3.624	92.04
		160			0.531	13.49	22.53	33.54	3.438	87.32
		XX			0.674	17.12	27.57	41.03	3.152	80.06
4-1/2 115	5.000 127.0	STD	40	40S	0.247	6.27	12.53	18.67	4.506	114.46
		XS	80	80S	0.355	9.02	17.63	26.24	4.290	108.96
		XX			0.710	18.03	32.56	48.45	3.580	90.94

NOMINAL PIPE SIZE	OD	SCHEDULE DESIGNATIONS			WALL THICKNESS		WEIGHT		ID	
INCH MM	INCH MM	ASME			INCH	MM	LBS/FOOT	KG/METER	INCH	MM
5 125	5.563 141.3	5		5S	0.109	2.77	4.36	9.46	5.345	135.76
		10		10S	0.134	3.40	7.78	11.56	5.295	134.50
		STD	40	40S	0.258	6.55	14.62	21.77	5.047	128.20
		XS	80	80S	0.375	9.52	20.80	30.97	4.813	122.24
		120			0.500	12.70	27.06	40.28	4.563	115.90
		160			0.625	15.88	32.99	49.12	4.313	109.54
		XX			0.750	19.05	38.59	57.43	4.063	103.20
6 150	6.625 168.3	5		5S	0.109	2.77	7.59	11.31	6.407	162.76
		10		10S	0.134	3.40	9.30	13.85	6.357	161.50
					0.188	4.78	12.96	19.28	6.249	158.78
		STD	40	40S	0.280	7.11	18.99	28.26	6.065	154.08
		XS	80	80S	0.432	10.97	28.60	42.56	5.761	146.36
		120			0.562	14.27	36.43	54.21	5.501	139.76
		160			0.719	18.26	45.39	67.57	5.187	131.78
		XX			0.864	21.95	53.21	79.22	4.897	124.40
7 175	7.625 193.7	STD	40	40S	0.301	7.65	23.57	35.10	7.023	178.40
		XS	80	80S	0.500	12.70	38.08	56.69	6.625	168.30
		XX			0.875	22.22	63.14	94.00	5.875	149.24
8 200	8.625 219.1			5S	0.109	2.77	9.92	14.78	8.407	213.56
		10		10S	0.148	3.76	13.41	19.97	8.329	211.58
		20			0.250	6.35	22.38	33.33	8.125	206.40
		STD	40	40S	0.277	7.04	24.72	36.80	8.071	205.02
		60			0.322	8.18	28.58	42.55	7.981	202.74
		XS	80	80S	0.406	10.31	35.67	53.09	7.813	198.48
		100			0.500	12.70	43.43	64.64	7.625	193.70
		120			0.594	15.09	51.00	75.92	7.437	188.92
		140			0.719	18.26	60.77	90.44	7.187	182.58
		XX			0.812	20.62	67.82	100.93	7.001	177.86
		160			0.875	22.22	72.49	107.93	6.875	174.64
					0.906	23.01	74.76	111.27	6.813	173.00
9 225	9.625 244.5	STD	40	40S	0.342	8.69	33.94	50.54	8.941	227.12
		XS	80	80S	0.500	12.70	48.77	72.60	8.625	219.10
		XX			0.875	22.22	81.85	121.85	7.875	200.04
10 250	10.750 273.0			5S	0.134	3.40	15.21	22.61	10.482	266.20
				10S	0.165	4.19	18.67	27.78	10.420	264.62
					0.188	4.78	21.23	31.62	10.374	263.44
		20			0.250	6.35	28.06	41.76	10.250	260.30
		30			0.307	7.80	34.27	51.01	10.136	257.40
		STD	40	40S	0.365	9.27	40.52	60.29	10.020	254.66
		XS	60	80S	0.500	12.70	54.79	81.52	9.750	247.60
		80			0.594	15.09	64.89	95.98	9.562	242.82
		100			0.719	18.26	77.10	114.71	9.312	236.48
		120			0.844	21.44	89.30	133.01	9.062	230.12
		140	XX		1.000	25.40	104.23	155.10	8.750	222.20
		160			1.125	28.58	115.75	172.27	8.500	215.84
11 275	11.750 298.5	STD	40	40S	0.375	9.52	45.60	67.91	11.000	279.44
		XS	80	80S	0.500	12.70	60.13	89.51	10.750	273.10
		XX			0.875	22.22	101.72	151.46	10.000	254.04
12 300	12.750 323.8			5S	0.156	3.96	21.00	31.24	12.438	315.88
				10S	0.180	4.57	24.19	35.98	12.390	314.66
					0.188	4.78	25.25	37.61	12.374	314.28
		20			0.250	6.35	33.41	49.71	12.250	311.10
		30			0.330	8.38	43.81	65.19	12.090	307.04
		STD		40S	0.375	9.52	49.61	73.86	12.000	304.78
		40			0.406	10.31	53.57	79.71	11.938	303.18
		XS		80S	0.500	12.70	65.80	97.84	11.750	298.40
		60			0.562	14.27	73.22	108.93	11.626	295.26
		80			0.688	17.48	88.71	132.05	11.374	288.84
		100			0.844	21.44	107.42	159.87	11.062	280.92
		120	XX		1.000	25.40	125.61	186.92	10.750	273.00
		140			1.125	28.58	139.81	208.08	10.500	266.66
		160			1.312	33.32	160.42	238.69	10.126	257.16
14 350	14.000 355.6			10S	0.188	4.78	27.76	41.36	13.624	346.08
		10			0.250	6.35	36.75	54.69	13.500	342.90
		20			0.312	7.92	45.65	67.91	13.376	339.76
		STD	30	40S	0.375	9.52	54.62	81.33	13.250	336.54
		40			0.438	11.13	63.50	94.55	13.124	333.34
		XS		80S	0.500	12.70	72.16	107.40	13.000	330.20
		60			0.594	15.09	85.13	126.72	12.812	325.42
		80			0.750	19.05	106.23	158.11	12.500	317.50
		100			0.938	23.83	130.98	194.98	12.124	307.94
		120			1.094	27.79	150.92	224.66	11.812	300.02
		140			1.250	31.75	170.37	253.58	11.500	292.10
		160			1.406	35.71	189.29	281.72	11.188	284.18

Figure A.1: Commercially produced pipeline properties 1 (https://www.tiogapipe.com/)

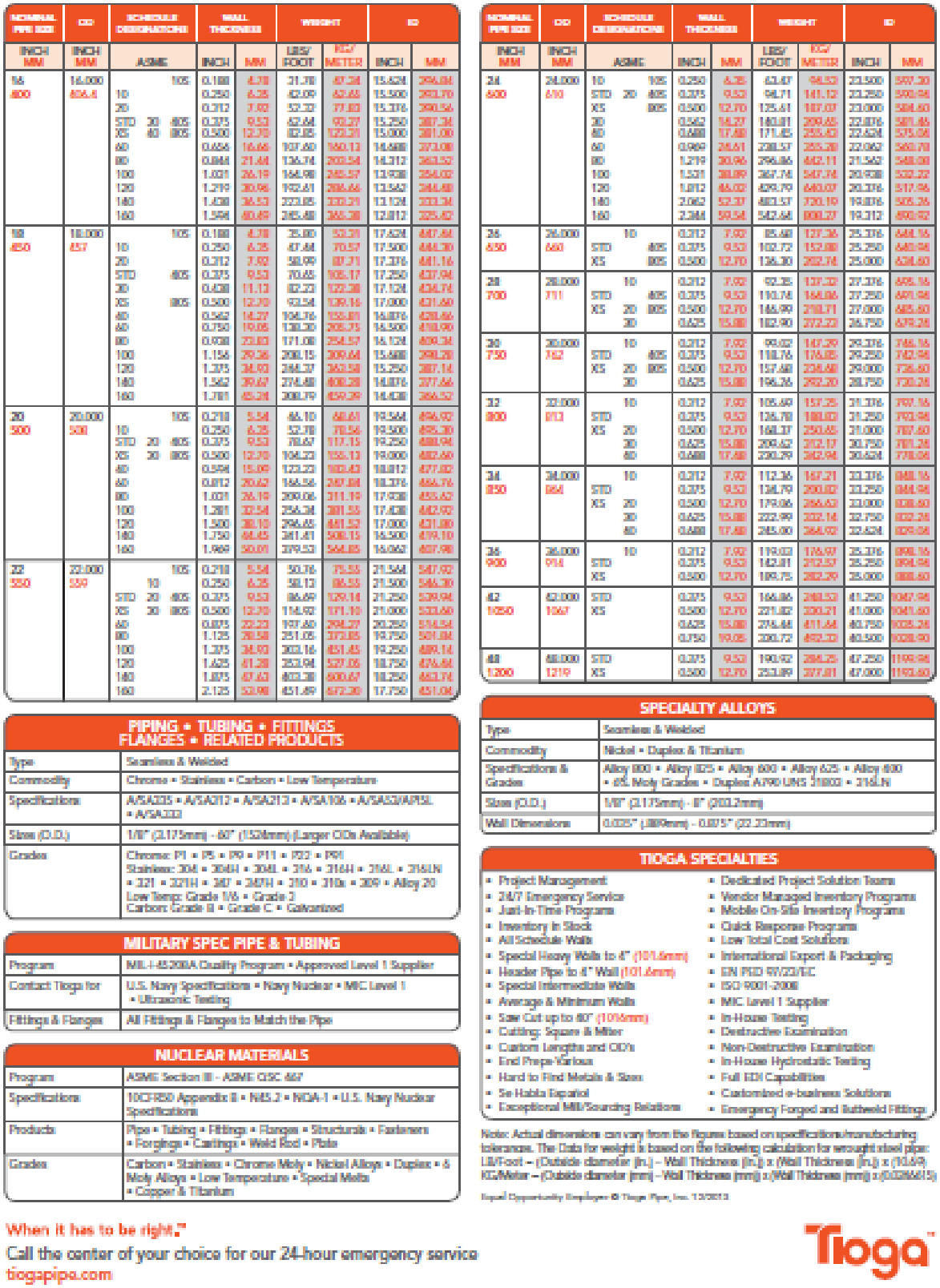

NOMINAL PIPE SIZE	OD	SCHEDULE DESIGNATIONS	WALL THICKNESS		WEIGHT		ID	
INCH MM	INCH MM	ASME	INCH	MM	LBS/ FOOT	KG/ METER	INCH	MM
16 400	16.000 406.4	10 105	0.188	4.78	31.78	47.34	15.624	396.84
		10	0.250	6.35	42.09	62.65	15.500	393.70
		20	0.312	7.92	52.37	77.83	15.376	390.56
		STD 20 405	0.375	9.53	62.64	93.27	15.250	387.34
		XS 40 805	0.500	12.70	82.85	122.71	15.000	381.00
		60	0.656	16.66	107.60	160.13	14.688	373.08
		80	0.844	21.44	136.74	203.54	14.312	363.52
		100	1.031	26.19	166.98	248.57	13.938	354.02
		120	1.219	30.96	192.61	286.66	13.562	344.48
		140	1.438	36.53	223.85	333.21	13.124	333.34
		160	1.594	40.49	245.48	365.38	12.812	325.42
18 450	18.000 457	105	0.188	4.78	35.80	53.31	17.624	447.64
		10	0.250	6.35	47.44	70.67	17.500	444.50
		20	0.312	7.92	58.99	87.81	17.376	441.16
		STD 605	0.375	9.53	70.65	105.17	17.250	437.94
		30	0.438	11.13	82.23	122.38	17.124	434.74
		XS 805	0.500	12.70	93.54	139.16	17.000	431.60
		40	0.562	14.27	104.76	155.81	16.876	428.66
		60	0.750	19.05	138.20	205.75	16.500	418.90
		80	0.938	23.83	171.08	254.57	16.124	409.34
		100	1.156	29.36	208.15	309.64	15.688	398.28
		120	1.375	34.93	244.37	363.58	15.250	387.14
		140	1.562	39.67	274.48	408.28	14.876	377.66
		160	1.781	45.24	308.79	459.39	14.438	366.52
20 500	20.000 508	105	0.218	5.54	44.10	65.61	19.564	496.92
		10	0.250	6.35	52.78	78.56	19.500	495.30
		STD 20 405	0.375	9.53	78.67	117.15	19.250	488.94
		XS 30 805	0.500	12.70	104.23	155.13	19.000	482.60
		40	0.594	15.09	123.23	183.43	18.812	477.82
		60	0.812	20.62	166.56	247.84	18.376	466.76
		80	1.031	26.19	209.06	311.19	17.938	455.62
		100	1.281	32.54	256.24	381.35	17.438	442.92
		120	1.500	38.10	296.65	441.52	17.000	431.80
		140	1.750	44.45	341.41	508.15	16.500	419.10
		160	1.969	50.01	379.53	564.85	16.062	407.98
22 550	22.000 559	105	0.218	5.54	50.76	75.55	21.564	547.92
		10	0.250	6.35	58.13	86.55	21.500	546.30
		STD 20 405	0.375	9.53	86.69	129.14	21.250	539.94
		XS 30 805	0.500	12.70	114.92	171.10	21.000	533.60
		40	0.875	22.23	197.80	294.37	20.250	514.34
		80	1.125	28.58	251.05	373.85	19.750	501.84
		100	1.375	34.93	303.16	451.45	19.250	489.14
		120	1.625	41.28	353.94	527.05	18.750	476.44
		140	1.875	47.63	403.38	600.67	18.250	463.74
		160	2.125	53.98	451.49	672.30	17.750	451.04

NOMINAL PIPE SIZE	OD	SCHEDULE DESIGNATIONS	WALL THICKNESS		WEIGHT		ID	
INCH MM	INCH MM	ASME	INCH	MM	LBS/ FOOT	KG/ METER	INCH	MM
24 600	24.000 610	10 105	0.250	6.35	63.47	94.53	23.500	597.30
		STD 20 405	0.375	9.53	94.71	141.12	23.250	590.94
		XS 805	0.500	12.70	125.61	187.07	23.000	584.60
		30	0.562	14.27	140.81	209.65	22.876	581.46
		40	0.688	17.48	171.65	255.62	22.624	575.04
		60	0.969	24.61	238.57	355.28	22.062	560.78
		80	1.219	30.96	296.86	442.11	21.562	548.08
		100	1.531	38.89	367.74	547.74	20.938	532.22
		120	1.812	46.02	429.79	640.07	20.376	517.56
		140	2.062	52.37	483.57	720.19	19.876	504.26
		160	2.344	59.54	542.66	808.27	19.312	490.62
26 650	26.000 660	10	0.312	7.92	85.68	127.36	25.376	644.16
		STD 405	0.375	9.53	102.72	152.88	25.250	640.94
		XS 805	0.500	12.70	136.30	202.74	25.000	634.60
28 700	28.000 711	10	0.312	7.92	92.35	137.32	27.376	695.16
		STD 405	0.375	9.53	110.74	164.86	27.250	691.94
		XS 20 805	0.500	12.70	146.99	218.71	27.000	685.60
		30	0.625	15.88	182.90	272.23	26.750	679.24
30 750	30.000 762	10	0.312	7.92	99.02	147.29	29.376	746.16
		STD 405	0.375	9.53	118.76	176.85	29.250	742.94
		XS 20 805	0.500	12.70	157.68	234.68	29.000	736.60
		30	0.625	15.88	196.26	292.20	28.750	730.24
32 800	32.000 813	10	0.312	7.92	105.69	157.25	31.376	797.16
		STD	0.375	9.53	126.78	188.83	31.250	793.94
		XS 20	0.500	12.70	168.37	250.65	31.000	787.60
		30	0.625	15.88	209.62	312.17	30.750	781.26
		40	0.688	17.48	230.29	342.94	30.624	778.04
34 850	34.000 864	10	0.312	7.92	112.36	167.21	33.376	848.16
		STD	0.375	9.53	134.79	200.82	33.250	844.94
		XS 20	0.500	12.70	179.06	266.62	33.000	838.60
		30	0.625	15.88	222.99	332.14	32.750	832.24
		40	0.688	17.48	245.00	364.92	32.624	828.04
36 900	36.000 914	10	0.312	7.92	119.03	176.97	35.376	898.16
		STD	0.375	9.53	142.81	212.57	35.250	894.94
		XS	0.500	12.70	189.75	282.39	35.000	888.60
42 1050	42.000 1067	STD	0.375	9.53	166.86	248.53	41.250	1047.94
		XS	0.500	12.70	221.82	330.21	41.000	1041.60
			0.625	15.88	276.44	411.64	40.750	1035.24
			0.750	19.05	330.72	492.30	40.500	1028.90
48 1200	48.000 1219	STD	0.375	9.53	190.92	284.25	47.250	1199.94
		XS	0.500	12.70	253.89	377.81	47.000	1193.60

PIPING • TUBING • FITTINGS FLANGES • RELATED PRODUCTS

Type	Seamless & Welded
Commodity	Chrome • Stainless • Carbon • Low Temperature
Specifications	A/SA335 • A/SA312 • A/SA213 • A/SA106 • A/SA53/API5L • A/SA333
Sizes (O.D.)	1/8" (3.175mm) - 60" (1524mm) (Larger ODs Available)
Grades	Chrome: P1 • P5 • P9 • P11 • P22 • P91 Stainless: 304 • 304H • 304L • 316 • 316H • 316L • 316LN • 321 • 321H • 347 • 347H • 310 • 310s • 309 • Alloy 20 Low Temp: Grade 1/6 • Grade 3 Carbon: Grade B • Grade C • Galvanized

MILITARY SPEC PIPE & TUBING

Program	MIL-I-45208A Quality Program • Approved Level 1 Supplier
Contact Tioga for	U.S. Navy Specifications • Navy Nuclear • NRC Level 1 • Ultrasonic Testing
Fittings & Flanges	All Fittings & Flanges to Match the Pipe

NUCLEAR MATERIALS

Program	ASME Section III - ASME QSC 467
Specifications	10CFR50 Appendix B • N45.2 • NQA-1 • U.S. Navy Nuclear Specifications
Products	Pipe • Tubing • Fittings • Flanges • Structurals • Fasteners • Forgings • Castings • Weld Rod • Plate
Grades	Carbon • Stainless • Chrome Moly • Nickel Alloys • Duplex • 6 Moly Alloys • Low Temperature • Special Melts • Copper & Titanium

SPECIALTY ALLOYS

Type	Seamless & Welded
Commodity	Nickel • Duplex & Titanium
Specifications & Grades	Alloy 800 • Alloy 825 • Alloy 600 • Alloy 625 • Alloy 400 • 6% Moly Grades • Duplex A790 UNS 31803 • 316LN
Sizes (O.D.)	1/8" (3.175mm) - 8" (203.2mm)
Wall Dimensions	0.035" (.889mm) - 0.875" (22.23mm)

TIOGA SPECIALTIES

- Project Management
- 24/7 Emergency Service
- Just-In-Time Programs
- Inventory In Stock
- All Schedule Walls
- Special Heavy Walls to 4" (101.6mm)
- Header Pipe to 4" Wall (101.6mm)
- Special Intermediate Walls
- Average & Minimum Walls
- Saw Cut up to 80" (1016mm)
- Cutting: Square & Miter
- Custom Lengths and OD's
- End Preps-Various
- Hard to Find Metals & Sizes
- Se Habla Español
- Exceptional Mill/Sourcing Relations
- Dedicated Project Solution Teams
- Vendor Managed Inventory Programs
- Mobile On-Site Inventory Programs
- Quick Response Programs
- Low Total Cost Solutions
- International Export & Packaging
- EN PED 97/23/EC
- ISO 9001-2008
- NRC Level 1 Supplier
- In-House Testing
- Destructive Examination
- Non-Destructive Examination
- In-House Hydrostatic Testing
- Full EDI Capabilities
- Customized e-business Solutions
- Emergency Forged and Buttweld Fittings

Note: Actual dimensions can vary from the figures based on specifications/manufacturing tolerances. The Data for weight is based on the following calculation for wrought steel pipe: LB/Foot = (Outside diameter (in.) – Wall Thickness (in.)) x (Wall Thickness (in.)) x (10.69) KG/Meter = (Outside diameter (mm) – Wall Thickness (mm)) x (Wall Thickness (mm)) x (0.0246615)

When it has to be right.™

Call the center of your choice for our 24-hour emergency service

tiogapipe.com

Tioga™

Figure A.2: Commercially produced pipeline properties 2 (https://www.tiogapipe.com/)

Appendix B

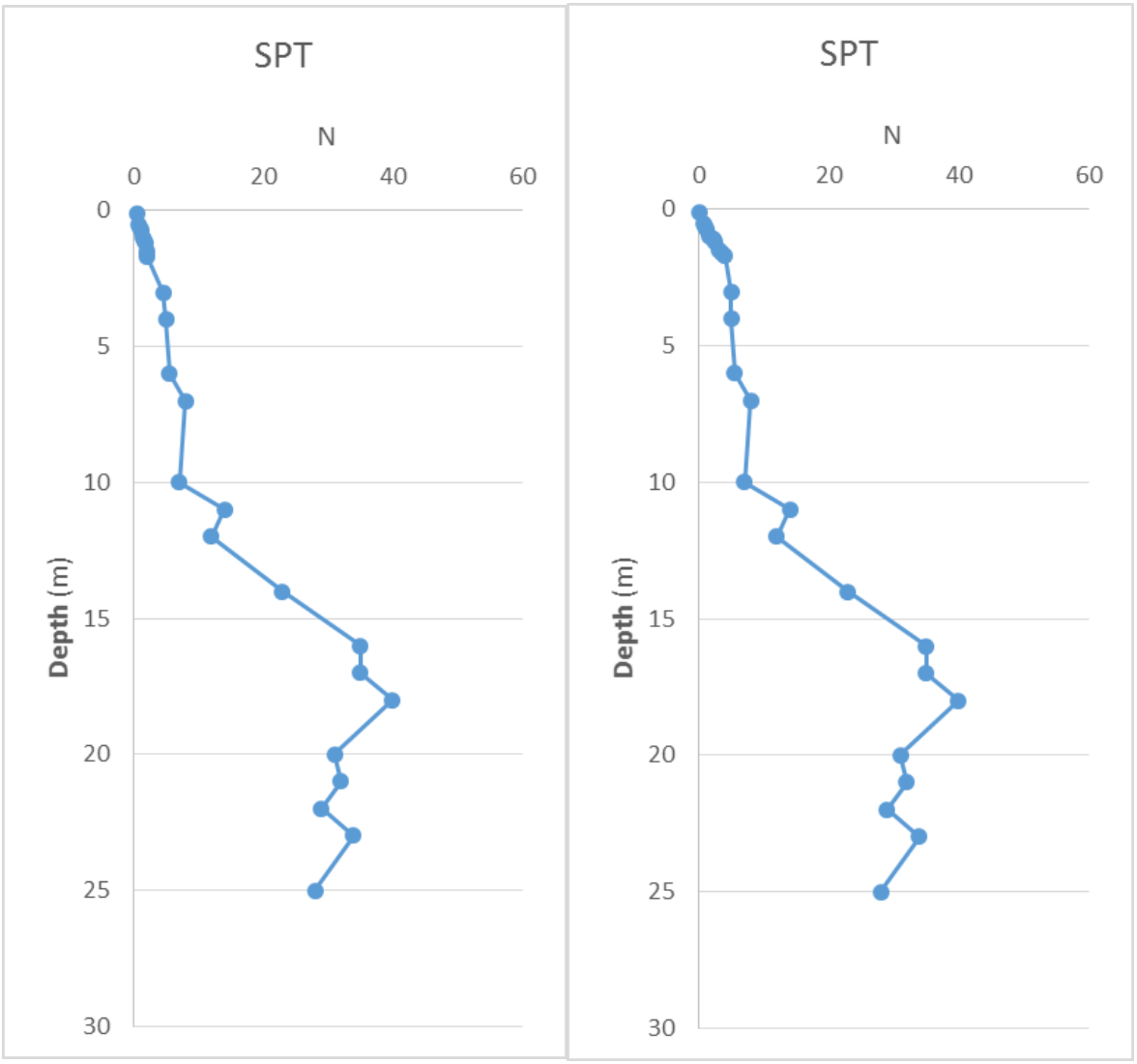

Figure B.1: Normal SPT used to the left, SPT for stiffer ground profile to the right